Combining Lattice Boltzmann Simulation and Synchrotron Imaging to Study Bubble Dynamics in Electrodes of Vanadium Redox Flow Batteries

Kangjun Duan

Energie & Umwelt / Energy & Environment
Band / Volume 722
ISBN 978-3-95806-955-8

Mitglied der Helmholtz-Gemeinschaft

JÜLICH
Forschungszentrum

Schriften des Forschungszentrums Jülich
Reihe Energie & Umwelt / Energy & Environment Band / Volume 722

Forschungszentrum Jülich GmbH
Institute of Energy Technologies (IET)
Theorie und computergestützte Modellierung von Materialien
in der Energietechnik (IET-3)

Combining Lattice Boltzmann Simulation and Synchrotron Imaging to Study Bubble Dynamics in Electrodes of Vanadium Redox Flow Batteries

Kangjun Duan

Schriften des Forschungszentrums Jülich
Reihe Energie & Umwelt / Energy & Environment Band / Volume 722

ISSN 1866-1793 ISBN 978-3-95806-955-8

Bibliografische Information der Deutschen Nationalbibliothek.
Die Deutsche Nationalbibliothek verzeichnet diese Publikation in der
Deutschen Nationalbibliografie; detaillierte Bibliografische Daten
sind im Internet über http://dnb.d-nb.de abrufbar.

Herausgeber und Vertrieb:	Forschungszentrum Jülich GmbH Zentralbibliothek, Verlag 52425 Jülich Tel.: +49 2461 61-5368 Fax: +49 2461 61-6103 zb-publikation@fz-juelich.de www.fz-juelich.de/zb
Umschlaggestaltung:	Grafische Medien, Forschungszentrum Jülich GmbH
Druck:	Grafische Medien, Forschungszentrum Jülich GmbH
Copyright:	Forschungszentrum Jülich 2026

Schriften des Forschungszentrums Jülich
Reihe Energie & Umwelt / Energy & Environment, Band / Volume 722

D 82 (Diss. RWTH Aachen University, 2026)

ISSN 1866-1793
ISBN 978-3-95806-954-1 (Print)
ISBN 978-3-95806-955-8 (E-Book)

Vollständig frei verfügbar über das Publikationsportal des Forschungszentrums Jülich (JuSER)
unter www.fz-juelich.de/zb/openaccess.

This is an Open Access publication distributed under the terms of the Creative Commons Attribution License 4.0, which permits unrestricted use, distribution, and reproduction in any medium, provided the original work is properly cited.

Abstract

The large-scale integration of renewably generated electrical energy into power grids poses a formidable challenge due to its intermittent and spatially distributed nature. While traditional power systems rely on coal or gas-fired plants for load balancing and frequency regulation, the increasing penetration of renewable sources necessitates advanced energy storage solutions to bridge the gap between fluctuating supply and real-time demand. Vanadium redox flow batteries (VRFBs) have emerged as a promising durable energy storage technology, playing a crucial role in stabilizing renewable energy input, enabling seasonal energy storage, and enhancing overall grid flexibility. However, despite their advantages, VRFBs face critical performance limitations due to side reactions that occur at the electrodes. Among them, the hydrogen evolution reaction (HER) has been identified as a major source of efficiency losses, leading to an imbalance in state of charge, and bubble formation, which disrupts ion transport and reduces the effective reaction area within the electrode. Understanding the mechanistic details of gas evolution and its interaction with the porous electrode structure is therefore essential for further optimizing battery performance.

To investigate gas evolution behavior in VRFB electrodes, synchrotron X-ray tomography was employed to obtain high-resolution three-dimensional images of gas bubbles formed during HER. These measurements enable a direct spatial characterization of individual bubbles and their morphology, but due to imaging contrast limitations, the electrode fibers could not be directly visualized in the presence of the electrolyte. To systematically analyze the observed bubble structures, we have developed a deep learning-based image processing framework, which enables automated segmentation, 3D reconstruction, and quantitative morphological analysis of bubbles. This approach facilitates high-throughput statistical evaluation of bubble size, shape, and spatial distribution under different electrochemical conditions. The results

have revealed that increasingly negative electrode potentials intensify HER, producing larger and more irregular bubbles that accumulate in regions like the electrode borders, leading to pathway blockage and a reduced reaction area.

However, the simultaneous visualization of bubbles and the underlying porous electrode microstructure could not be achieved in these experiments. To bridge this gap, additional synchrotron X-ray scans of dry electrodes were conducted, allowing for a more detailed characterization of the fiber structure. These structural insights were then incorporated into Lattice Boltzmann method (LBM) simulations, enabling a systematic investigation of how electrolyte flow, electrode compression, and HER rate influence bubble transport and retention within the porous network. The numerical simulations revealed that optimal electrolyte velocity enhances bubble removal, whereas excessive compression leads to gas entrapment, severely impairing mass transport. By correlating these results with experimental observations, this study provides a mechanistic understanding of how gas evolution influences mass transport and electrochemical performance in VRFBs.

This work establishes a multi-scale framework limited to electrode- and pore-scale phenomena for investigating gas evolution in electrochemical energy storage systems, combining high-resolution imaging, machine learning-based data analysis, and mesoscale numerical modeling. The methodologies developed in this dissertation advance the understanding of HER-driven bubble dynamics and lay the foundation for future research on multiphase phenomena in energy storage and conversion systems. By systematically addressing the interplay between electrochemical reactions, gas evolution, and electrode microstructure, this study provides new insights for optimizing electrode design and operational strategies, ultimately paving the way for more efficient and durable VRFBs, which are essential for the large-scale deployment of a renewable energy infrastructure.

Zusammenfassung

Die großflächige Integration erneuerbar erzeugter elektrischer Energie in Stromnetze stellt aufgrund ihres intermittierenden und räumlich verteilten Charakters eine erhebliche Herausforderung dar. Während herkömmliche Stromsysteme auf Kohle- oder Gaskraftwerke zur Lastregelung und Frequenzstabilisierung angewiesen sind, erfordert der zunehmende Anteil erneuerbarer Energien fortschrittliche Energiespeicherlösungen, um die Lücke zwischen schwankendem Angebot und Echtzeit-Nachfrage zu überbrücken. Dennoch weisen VRFBs trotz ihrer Vorteile erhebliche Leistungsbegrenzungen auf, insbesondere durch Nebenreaktionen an den Elektroden. Eine der bedeutendsten Nebenreaktionen ist die Wasserstoffentwicklungsreaktion (HER), die zu Effizienzverlusten führt und ein Ungleichgewicht im Ladezustand (State of Charge) sowie Blasenbildung verursacht. Diese Gasblasen stören den Ionentransport und verringern die effektive Reaktionsfläche innerhalb der Elektrode. Ein mechanistisches Verständnis der Gasentwicklung und ihrer Wechselwirkung mit der porösen Elektrodenstruktur ist daher entscheidend für die weitere Optimierung der Batterieleistung.

Um das Gasentwicklungsverhalten in VRFB-Elektroden zu untersuchen, wurde Synchrotron Röntgentomographie eingesetzt, um hochauflösende dreidimensionale Bilder von während der HER entstehenden Gasblasen zu erhalten. Diese Messungen ermöglichen eine direkte räumliche Charakterisierung einzelner Blasen und ihrer Morphologie. Zur systematischen Analyse der beobachteten Blasenstrukturen wurde ein Deep-Learning-basiertes Bildverarbeitungsframework entwickelt, das eine automatisierte Segmentierung, dreidimensionale Rekonstruktion sowie eine quantitative morphologische Analyse der Blasen erlaubt. Dieser Ansatz ermöglicht eine hochdurchsatzfähige statistische Auswertung von Blasengröße, -form und räumlicher Verteilung unter verschiedenen elektrochemischen Bedingungen. Die Ergebnisse zeigen, dass zunehmend negative Elektrodenpotenziale die HER verstärken und zur Bildung größerer und

unregelmäßiger Blasen führen, die sich bevorzugt in Bereichen wie den Elektrodenrändern ansammeln. Dies resultiert in einer Blockierung von Transportpfaden und einer Reduktion der effektiven Reaktionsfläche.

Eine gleichzeitige Visualisierung der Gasblasen und der zugrunde liegenden porösen Elektrodenmikrostruktur konnte in diesen Experimenten nicht erreicht werden. Um diese Lücke zu schließen, wurden zusätzliche Synchrotron-Röntgenscans trockener Elektroden durchgeführt, die eine detailliertere Charakterisierung der Faserstruktur ermöglichen. Diese strukturellen Informationen wurden anschließend in Lattice-Boltzmann-Simulationen (LBM) integriert, um systematisch zu untersuchen, wie Elektrolytströmung, Elektrodenkompression und HER-Rate den Blasentransport und die Blasenretention innerhalb des porösen Netzwerks beeinflussen. Die numerischen Simulationen zeigen, dass eine optimale Elektrolytgeschwindigkeit die Blasenentfernung begünstigt, während eine übermäßige Kompression zur Gaseinschließung führt und den Stofftransport erheblich beeinträchtigt. Durch die Korrelation dieser Ergebnisse mit experimentellen Beobachtungen liefert diese Arbeit ein mechanistisches Verständnis darüber, wie Gasentwicklung den Stofftransport und die elektrochemische Leistung in VRFBs beeinflusst.

Diese Arbeit etabliert ein mehrskaliges Untersuchungsframework, das auf Elektroden- und Porenskalenphänomene begrenzt ist, zur Analyse der Gasentwicklung in elektrochemischen Energiespeichersystemen. Die in dieser Dissertation entwickelten Methoden erweitern das Verständnis von HER-getriebener Blasendynamik und bilden die Grundlage für zukünftige Forschungen zu Mehrphasenphänomenen in Energiespeicher- und Umwandlungssystemen. Durch die systematische Analyse des Zusammenspiels zwischen elektrochemischen Reaktionen, Gasentwicklung und Elektrodenmikrostruktur liefert diese Studie neue Erkenntnisse zur Optimierung des Elektrodenaufbaus und der Betriebsstrategien und trägt damit zur Entwicklung effizienterer und langlebigerer VRFBs bei, die für den großskaligen Ausbau einer erneuerbaren Energieinfrastruktur von zentraler Bedeutung sind. [1]

[1] Die Erstübersetzung wurde mit Hilfe von Google translate durchgeführt und anschließend manuell überarbeitet.

Acknowledgments

This dissertation would not have been possible without the support and encouragement of many people, to whom I would like to express my sincere gratitude.

First and foremost, I would like to thank my supervisors, Prof. Roswitha Zeis, Prof. Jens Harting, Prof. Michael Eikerling, and Dr. Thomas Kadyk, for their invaluable guidance, technical support, and consistent encouragement throughout my doctoral journey. Their expertise and insights helped me navigate through many challenges and taught me skills that I consider priceless.

I am also deeply grateful to my colleagues and friends at Forschungszentrum Jülich, and Helmholtz Institute Ulm. In particular, I would like to thank Kerstin Köble and Thanh Hoang Vu for their kind help and fruitful discussions. Their support made my research experience both productive and enjoyable.

Special thanks go to SGL Carbon for providing the SIGRACELL® carbon felts used in this study.

I also gratefully acknowledge the China Scholarship Council for funding my PhD studies under grant number 202106950013.

The experimental work would not have been possible without access to world-class imaging facilities. I thank the KIT light source for beamline access and the Institute for Beam Physics and Technology (IBPT) for operating the KARA storage ring. Furthermore, I thank the Deutsche Forschungsgemeinschaft (DFG) under Project No. 431791331—SFB 1452, the Federal Ministry of Education and Research (BMBF) under project H2Giga/AEM-Direkt (Grant No. 03HY103HF), and the Gauss Centre for Supercomputing (GCS) for providing computing time through the John von Neumann Institute for Computing (NIC) on the JUWELS supercomputer at Jülich Supercomputing Centre.

I am also thankful to the Fonds der Chemischen Industrie (FCI) for supporting our collaborators

K. K. and M. S. with a Kekulé Ph.D. fellowship.

Beyond academic support, I wish to sincerely thank my family for their unwavering love, trust, and support. Without their encouragement and sacrifices, I would not have had the opportunity to pursue this path in Germany and experience such a meaningful chapter in my life.

Lastly, I thank all the friends and colleagues who have walked alongside me during this journey. Your kindness and motivation carried me through moments of doubt and fatigue, and I will always be grateful.

Erklärungen zur Dissertation

Ich erkläre hiermit eidesstattlich, dass ich die Dissertation selbstständig verfasst, alle in Anspruch genommenen Hilfen in der Dissertation angegeben habe und die schriftliche und elektronische Fassung übereinstimmen.

Ort, Datum | Unterschrift

Die Grundsätze zur Sicherung guter wissenschaftlicher Praxis der RWTH Aachen habe ich eingehalten.

Ort, Datum | Unterschrift

Die Veröffentlichung verletzt keine bestehenden Betriebsgeheimnisse.

Ort, Datum | Unterschrift

Contents

List of figures

List of Tables

Nomenclature

Symbols

Symbol	Description	Unit
A	Parameter controlling interfacial tension	–
B_i	Weight to ensure mass conservation	–
C_l	Length scale conversion factor	m / l.u.
C_t	Time scale conversion factor	s / l.u.
C_m	Mass scale conversion factor	kg / l.u.
F	Body force	N
F_i	Discrete force in direction i	N
G	Color gradient	–
P	Pressure	Pa
Re	Reynolds number	–
Ca	Capillary number	–
e_i	Discrete velocity in direction i	l.u./t
f_i	Distribution function in direction i	–
k_r	Reaction rate	s^{-1}
t	Lattice time	l.u.
u	Velocity vector	$\mathrm{m\,s}^{-1}$
x	Lattice site position	l.u.
c_s	Speed of sound	$\mathrm{m\,s}^{-1}$
w_i	Weighting factor in direction i	–

Greek Letters

Symbol	Description	Unit
α	Fluid component	–
β	Parameter controlling interface thickness	–
θ_i	Angle between color gradient and lattice velocity	rad
τ	Relaxation time	l.u.
ϕ	Color function (order parameter)	–
μ	Dynamic viscosity	Pa s
ρ	Density	$\mathrm{kg\,m^{-3}}$
ρ_0	Reference density	$\mathrm{kg\,m^{-3}}$
σ	Interfacial tension	$\mathrm{N\,m^{-1}}$
$\bar{\nu}$	Mixed fluid kinematic viscosity	$\mathrm{m^2\,s^{-1}}$
ν_r	Red fluid kinematic viscosity	$\mathrm{m^2\,s^{-1}}$
ν_b	Blue fluid kinematic viscosity	$\mathrm{m^2\,s^{-1}}$

Subscripts and Superscripts

0	Initial value
b	Blue fluid (liquid phase)
r	Red fluid (gas phase)
i	Discrete velocity direction
eq	Equilibrium value
$pert$	Perturbation term
rec	Recoloring term
$boundary$	Lattice nodes at the boundary
LB	Lattice Boltzmann units
$Phys$	Physical units

Abbreviations

3D	Three-dimensional
BGK	Bhatnagar–Gross–Krook
CR	Compression ratio
CT	Computed tomography
CV	cyclic voltammetry
DEMS	Differential electrochemical mass spectrometry
DRT	istribution of relaxation times
EIS	electrochemical impedance spectroscopy
HER	Hydrogen evolution reaction
ITK	Insight Segmentation and Registration Toolkit
KARA	Karlsruhe Research Accelerator
LBM	Lattice Boltzmann Method
LDES	Long-duration energy storage
LGA	Lattice gas automata
l.u.	Lattice unit
TP	true positives
TN	true negatives
FP	false positives
FN	false negatives
OER	Oxygen evolution reaction
OCV	Open circuit voltage
PEM	Proton exchange membrane
PTL	Porous transport layer
RFB	Redox flow battery
RHE	Reversible hydrogen electrode
SHE	Standard hydrogen electrode potential
VRFBs	Vanadium redox flow batteries

1. Introduction

1.1. Energy and Environmental Background: The Need for Long-Duration Energy Storage

Global environmental challenges have reached a critical point in recent years, driving the urgent need for clean and sustainable energy alternatives. International efforts to curb carbon emissions have been marked by a series of policy milestones, from the United Nations Framework Convention on Climate Change (1992) to the Kyoto Protocol (1997) and notably the Paris Agreement (2015). The Paris Agreement sets clear targets for global carbon emission control, with a strong emphasis on reducing emissions in the energy and industrial sectors [1]. Research shows that the power generation sector is one of the primary sources of greenhouse gases, accounting for roughly one-third of global emissions [2].

A 2024 study analyzing the pollution risks of power generation companies revealed that coal remains the dominant source of global electricity (35.98%) with a pollution index significantly higher than that of nuclear and natural gas [3]. The study advocates for using composite environmental pollution indices to assess energy resource safety, thereby promoting low-carbon energy development . Furthermore, data indicate that improvements in power plant efficiency have already had a measurable impact: from 1990 to 2017, increasing the average efficiency of coal-fired power plants from 32% to 36% reduced CO_2 emissions by approximately 2.2 billion tonnes, while the expansion of hydro-power and nuclear energy decreased emissions by 1.67 and 1.07 billion tonnes, respectively [4].

The increasing penetration of renewable energy sources, particularly wind and solar power, has fundamentally reshaped the modern energy landscape [5, 6]. While these energy sources pro-

vide significant environmental benefits, their intermittent and unpredictable nature poses substantial challenges to grid stability and reliability. Unlike conventional fossil fuel-based power generation, which can be dispatched on demand, renewable energy generation depends on weather conditions, leading to fluctuations in power supply [7–12]. Currently, power grids rely heavily on coal and gas-fired power plants to maintain grid stability through load balancing and frequency regulation. However, with the global push toward carbon neutrality and the gradual phase-out of fossil fuels, the future power grid must evolve from a system dominated by coal and gas into an integrated network of source, grid, load, and storage [13]. This transformation is essential not only for reducing carbon emissions but also for ensuring reliable power delivery in a system increasingly reliant on variable renewable energy.

In this evolving energy landscape, long-duration energy storage (LDES) becomes indispensable. Defined by the U.S. Department of Energy as storage systems capable of retaining energy for more than 10 hours [14], LDES is critical for bridging periods of surplus renewable generation with times of high demand, ranging from hours to even seasons. In November 2022, COP26 in Glasgow established a Long-Duration Energy Storage Council to accelerate the development and deployment of these technologies [15].

Among the various LDES options, including pumped hydro storage, compressed air energy storage, and hydrogen storage, redox flow batteries offer unique advantages due to their ability to decouple power and energy capacity. In particular, vanadium redox flow batteries (VRFBs) have attracted significant attention for their high efficiency, long cycle life, and inherent safety [7, 16]. These features make VRFBs exceptionally well suited for grid-scale applications, where they can play a pivotal role in stabilizing energy output, enhancing grid flexibility, and facilitating the large-scale integration of renewable energy [17].

In summary, the confluence of stringent international emission targets, the predominance of fossil fuels in current energy systems, and the disruptive nature of renewable energy sources underscores the critical need for robust long-duration energy storage solutions. VRFBs, with their distinct technical and operational advantages, are poised to become a cornerstone technology in the future sustainable power grid, ensuring both environmental sustainability and system reliability.

1.2. Fundamentals of Vanadium Redox Flow Batteries

Flow batteries are a class of electrochemical energy storage systems in which electroactive species are dissolved in liquid electrolytes and stored externally in separate tanks. During charge and discharge, these electrolytes are circulated through an electrochemical cell, enabling the decoupling of energy capacity (determined by the tank volume) from power (dictated by the cell stack) [18]. The concept of a flow battery-like system can be traced back to the late 19th century. In 1879, John Doyle described a refillable Zn-Br_2 battery in a patent [19, 20], although it differs substantially from current redox flow battery (RFB) designs.

Significant early advances in flow battery research emerged in the 1970s and 1980s, particularly through NASA's studies on iron-chromium (Fe/Cr) systems [21]. These investigations laid much of the groundwork for modern RFB research, exploring the potential of liquid-based redox couples for energy storage. Sum, Rychcik, and Skyllas-Kazacos at the University of New South Wales successfully demonstrated the viability of an all-vanadium redox flow battery by exploiting vanadium's four stable oxidation states, which operate effectively within the electrochemical voltage window of a graphite–aqueous acid interface [22–25]. This innovation overcame the cross-contamination and dilution issues faced by mixed-metal systems such as iron–chromium RFBs. Following these advances, UNSW filed several patents related to VRFB technology, which were subsequently licensed to corporations in Japan, Thailand, and Canada, leading to varying degrees of commercial success [26–29].

Today, the VRFB is widely regarded as the most mature and commercially promising flow battery technology [30]. Its single-metal electrolyte design prevents cross-contamination of active species, a major concern in other RFB chemistries, and confers a high degree of electrochemical reversibility [31]. VRFBs also offer a long cycle life, relatively fast response times, and the ability to be deeply discharged without significant capacity loss [12]. Typical energy densities range from about 20 Wh L^{-1} to 55 Wh L^{-1} [30], which is lower than many solid-state batteries but sufficient for stationary applications requiring multi-hour to multi-day storage.

Recent years have seen a surge in large-scale VRFB deployments worldwide, signaling the technology's growing commercial viability. In China, for example, a 400 MWh VRFB project in Dalian began operation in 2022, with plans to expand to 800 MWh, one of the largest flow bat-

tery installations globally [32]. Japan's Sumitomo Electric has deployed more than 30 VRFB systems worldwide since the early 2000s, ranging from small-scale demonstrations to multi-megawatt-hour facilities [30]. In the United States, utility-scale demonstrations have emerged in solar-heavy states like California, focusing on multi-hour storage, peak shaving, and improved grid resiliency [33]. Across Europe, VRFB solutions marketed under the CellCube brand (Enerox GmbH) have been deployed for commercial and industrial applications, including grid-scale pilots in Germany and Austria [30]. Numerous other companies and research institutes continue to optimize electrode materials, membranes, and electrolyte formulations to further improve system.

1.2.1. The Vanadium Redox Flow Battery System

A VRFB system is comprised of several integrated components that work together to achieve efficient energy storage, as shown in Figure 1.1. At the heart of the system are two external electrolyte tanks that store vanadium-based solutions in different oxidation states. One tank contains the negative electrolyte, typically a mixture of V^{2+} and V^{3+} ions, while the other holds the positive electrolyte, usually composed of V^{4+} and V^{5+} species. These tanks define the overall energy capacity of the battery and allow the decoupling of energy and power components.

The stored electrolytes are continuously circulated through a cell stack by pumps and a network of flow channels. Within the cell stack, each individual cell is constructed with two half-cells separated by an ion-selective membrane [12]. This membrane plays a critical role in maintaining charge balance by permitting proton transfer while preventing the mixing of the two distinct vanadium electrolytes. Carbon-based electrodes, typically in the form of carbon felt or carbon paper, are installed in both half-cells to provide a high surface area for the electrochemical reactions.

The working principle of a VRFB hinges on the reversible redox reactions of vanadium ions within a specific electrochemical voltage window. During the charging process, an external power source drives electrons into the negative half-cell, reducing V^{3+} to V^{2+} according to the

reaction:

$$V^{3+} + e^- \longrightarrow V^{2+} \tag{1.1}$$

Simultaneously, in the positive half-cell, V^{4+} is oxidized to V^{5+} with water participating in the reaction:

$$VO^{2+} + H_2O \longrightarrow VO_2^+ + 2\,H^+ + e^- \tag{1.2}$$

During discharging, these reactions reverse: electrons flow back from the battery to the external circuit as V^{2+} is oxidized back to V^{3+} in the negative half-cell, while V^{5+} is reduced to V^{4+} in the positive half-cell. The overall net reaction can be summarized as:

$$V^{3+} + VO^{2+} + 2\,H^+ \longrightarrow V^{2+} + VO_2^+ + H_2O \tag{1.3}$$

By utilizing vanadium in multiple oxidation states, the VRFB design effectively avoids cross-contamination issues common in mixed-metal systems, thereby enhancing cycle life and system reliability. The energy is stored in the liquid electrolyte within the tanks, while the cell stack converts electrical energy to chemical energy, and vice versa via these well-coordinated redox reactions.

Ancillary components, such as pumps and control systems, ensure uniform electrolyte flow and maintain optimal reaction conditions. This integrated approach allows the VRFB to deliver stable power output and high energy efficiency over thousands of cycles, making it particularly suitable for large-scale, long-duration energy storage applications.

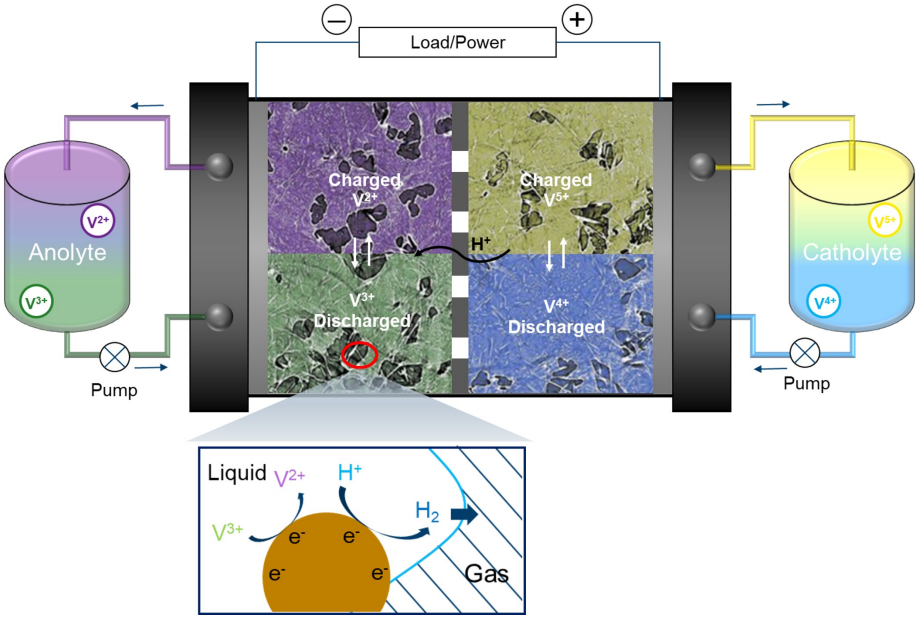

Figure 1.1.: An illustration of the working principle of a vanadium redox flow battery

1.2.2. Challenges in VRFB Development

Despite their promise as a long-duration energy storage technology characterized by high safety, long cycle life, and environmental compatibility, VRFBs still face several critical technical challenges impeding their widespread commercialization. Among these, the major issue remains the high initial investment costs, driven primarily by expensive electrolyte materials, particularly high-purity vanadium solutions, and advanced stack components such as ion-exchange membranes and bipolar plates [34]. Although recent progress has been made in cost reduction through electrolyte optimization and advances in manufacturing techniques, initial system costs remain significantly higher than those of competing technologies like lithium-ion batteries, restricting VRFBs' near-term market penetration.

A further notable limitation arises from the intrinsically low energy density of VRFB systems. Currently, the energy density of VRFBs is generally in the range of 20–40 Wh/kg, considerably lower than the 80–180 Wh/kg achievable by lithium-ion counterparts [35]. This low energy density translates into larger physical footprints for the same storage capacity, constraining their deployment in space-sensitive scenarios. Improvements such as increasing electrolyte con-

centration, developing high-performance electrode materials, and optimizing stack architecture represent ongoing research efforts aimed at mitigating this issue [36].

Operational efficiency and stability also pose substantial challenges. Typical VRFB systems exhibit relatively modest energy conversion efficiencies (70%–75%) [17, 37], which are significantly lower than those of lithium-ion systems (around 90%) [38]. This efficiency gap largely originates from resistive losses within cell stacks, uneven electrolyte distribution, and parasitic side reactions, especially hydrogen evolution, which occurs under certain operating conditions. Moreover, VRFBs are susceptible to self-discharge due to species crossover through the membrane, especially during prolonged idle periods [39]. While this does not typically result in permanent capacity loss, it reduces round-trip efficiency and necessitates periodic rebalancing of the electrolytes [40]. In parallel, aging mechanisms such as membrane degradation, pump wear, and electrolyte contamination accumulate over time and can lead to performance decay, reduced energy efficiency, and increased maintenance frequency [7, 11, 41]. Additionally, the narrow optimal temperature window (typically between 10–40 °C) necessitates supplementary thermal management solutions, adding complexity and raising operational costs [34].

Furthermore, the inherent system complexity and associated maintenance requirements present additional barriers. VRFBs rely on pumps and complex fluid distribution networks to circulate electrolytes, leading to parasitic power consumption and increased maintenance demands [7]. Frequent inspections, periodic replacements of components such as graphite electrodes and membranes, and monitoring electrolyte condition further raise operational expenditures and challenge long-term system reliability.

Addressing these technical hurdles through continuous technological advancements—in electrolyte formulation, electrode materials, cell-stack design optimization, and enhanced system integration—is essential to unlocking the full commercial potential of VRFB technology. Within this broader technical framework, understanding specific phenomena such as parasitic reactions and gas bubble formation inside electrode structures remains crucial. The subsequent section focuses specifically on the nature and implications of these parasitic side reactions, providing detailed insight into their mechanisms and consequences for VRFB performance.

1.3. Parasitic side reactions

Although VRFBs are designed to harness the reversible redox reactions of vanadium ions in a strongly acidic environment, several unwanted side reactions can occur under practical operating conditions [42]. These so-called “parasitic reactions” consume charge that would otherwise be used for the vanadium redox process and, over time, lead to electrode degradation and electrolyte imbalances [36]. Among these reactions, hydrogen evolution at the negative electrode is generally the most problematic, but other reactions, such as oxygen evolution at the positive electrode and carbon corrosion at high potentials, also contribute to performance losses.
When the negative half-cell potential becomes sufficiently negative during charging, protons in the acidic medium can be reduced to hydrogen gas:

$$2\,H^+ + 2\,e^- \longrightarrow H_2. \tag{1.4}$$

This hydrogen evolution reaction (HER) not only diverts electrons from the desired V(III)/V(II) couple, thus lowering the Coulombic efficiency, but also leads to the formation of gas bubbles within the porous electrode structure. These bubbles exhibit two primary detrimental effects. On one hand, their accumulation in pore spaces impedes electrolyte transport by physically blocking flow paths, leading to local mass transport limitations. On the other hand, their adhesion to carbon fiber surfaces effectively reduces the electrochemically active area, thereby limiting the number of accessible reaction sites. Both effects contribute to diminished current density and overall energy efficiency of the cell[43]. Although electrode modifications, such as metal-ion doping or surface treatments, have been explored to suppress HER [42], the precise motion of bubbles (nucleation, coalescence, detachment) within the electrode remains incompletely understood. Such knowledge is crucial for developing strategies that mitigate the parasitic impact of gas evolution.
Another side reaction, the oxygen evolution reaction (OER), can occur at the positive electrode if the cell potential becomes high enough to oxidize water:

$$2\,H_2O \longrightarrow O_2 \uparrow + 4H^+ + 4\,e^-. \tag{1.5}$$

Although less frequent under normal VRFB operation, this reaction becomes more likely during severe overcharging or elevated potentials. Like HER, OER leads to bubble formation and can diminish the cell's overall efficiency.

Additionally, carbon-based electrodes, especially at the positive side, are vulnerable to corrosion if high potentials persist for extended periods. This so-called carbon corrosion can be summarized by

$$C + 2\,H_2O \longrightarrow CO_2 \uparrow + 4\,H^+ + 4\,e^-, \tag{1.6}$$

and it can compromise electrode integrity over the long term. Moreover, residual oxygen or other impurities in the negative half-cell may gradually oxidize V(II) to V(III), causing additional inefficiencies and electrolyte imbalances if the system is not tightly sealed [44].

Taken as a whole, these parasitic reactions contribute to self-discharge, reduce the battery's capacity and cycle life, and increase operational costs by demanding more rigorous control of potentials and periodic electrolyte maintenance. From a research perspective, understanding the detailed mechanisms, particularly of hydrogen evolution, is critical for advancing VRFB technology. Gas bubble formation in the negative electrode not only reduces accessible surface area but can also trigger local inhomogeneities in current distribution and hamper mass transfer [12, 36, 45]. While our current studies primarily investigate bubble dynamics in electrode. Such investigations will help guide the design of electrode materials, and operating conditions to minimize parasitic reactions and improve the durability and efficiency of VRFB systems.

1.4. State of the Art: Hydrogen Evolution Reaction in VRFBs

In recent years, considerable research has been conducted to understand and mitigate the parasitic gas evolution reaction occurring in VRFBs. The undesired reactions significantly compromise battery efficiency, primarily through the formation of gas bubbles that obstruct electrolyte flow, hinder ion transport, and reduce effective reaction surfaces, thus negatively affecting overall performance and durability [46, 47].

1.4.1. Experimental Research on HER

The HER is recognized as one of the most critical parasitic reactions negatively affecting the performance of VRFBs. Initial experimental investigations of HER mainly employed conventional electrochemical methods, such as cyclic voltammetry, polarization measurements, and differential electrochemical mass spectrometry (DEMS), to study the fundamental electrochemical behavior at the electrode-electrolyte interface. For instance, Eifert et al. [48] systematically employed DEMS to investigate the influence of different electrode pretreatment methods, including thermal and chemical aging, on the side reactions occurring at carbon-felt electrodes in VRFBs. Their findings demonstrated that electrode degradation and side reactions such as HER and carbon corrosion significantly depend on the electrode's surface structure and chemical composition. These results provided macroscopic insights into electrode aging but did not elucidate bubble dynamics or transport behavior within the electrode itself. Ma et al. [46] quantitatively analyzed the impact of HER on VRFB performance, demonstrating a pronounced decrease in energy efficiency (average energy efficiency reduction by 2.92%) and significant capacity losses after extended cycling. The detrimental effects of HER include bubble formation, which blocks electrolyte flow channels and electrodes, increasing both pressure drop and ohmic resistance, thus adversely affecting overall battery operation.

To mitigate the adverse impacts of HER, substantial experimental research efforts have been dedicated to enhancing electrode performance [49–51], electrolyte optimization [52–55], and operational condition adjustmentss [56–58]. One common approach is electrode surface modification, which aims at suppressing HER by enhancing the catalytic selectivity of carbon-based electrodes towards the desired vanadium redox reactions [59, 60]. Najjar et al. [49] used tungsten oxide to modify carbon cloth electrodes on the negative half-cell. The results showed that the V^{2+}/V^{3+} reaction kinetics was significantly improved compared to untreated carbon cloth, and the hydrogen evolution reaction (HER) was inhibited. Kim et al. [61] demonstrated that introducing oxygen-containing functional groups onto carbon nanotube-modified graphite felt electrodes effectively increases HER overpotential, improving the selectivity for the desired V^{3+}/V^{2+} redox reactions. Similarly, Wen et al. [50] and Schneider et al. [51] explored the use of bismuth additives in electrolyte solutions, finding that these additives significantly enhance

the selectivity of V^{3+}/V^{2+} redox couples over HER. They demonstrated through in-situ mass spectrometry that a bismuth concentration of 750 ppm provides optimal catalytic activity, selectively promoting the vanadium redox reaction over HER. Alternatively, operating the negative electrode within a more restricted potential window can limit HER, but this approach may also reduce the efficiency of the desired redox reactions [62]. Other impurities or additives could also benefit the electrode kinetics and inhibit hydrogen release at the negative electrode (e.g. $PbCl_3$, $InCl_3$, or Sb_2O_3) [54]. Fetyan et al. [56] operated the VRFB at different temperatures. They found that increasing temperature significantly enhances the HER at the negative half-cell, leading to a decrease in coulombic efficiency. Wei et al. [58] conducted in-situ experiments and found that the HER is more sensitive to temperature variation than the V^{3+} reduction. Zhang et al. [63] systematically studied the relationship between in-situ hydrogen evolution and electrolyte flow resistance in porous carbon felt electrodes, highlighting that carefully managing the operating parameters, such as controlling current density and electrolyte flow rate, could significantly reduce bubble-induced flow resistance. Their results suggest that limiting HER activity through optimal operational conditions can substantially enhance electrolyte transport and system performance. Similarly, Ye et al. [64] explored strategies to break the vicious cycle caused by bubble trapping. By demonstrating how accumulated gas bubbles increasingly restrict electrolyte flow, their work emphasized the need for electrode structure optimization and flow field design to improve electrolyte uniformity and minimize the negative impacts of bubbles on battery performance. The work of Eifert et al. [65] shows that the maximum saturation of carbon felt is achieved by a flat flow field after the first injection and by a serpentine flow field after continuous flow. Köble et al. [66] revealed the multifaceted impacts of electrode modifications for VRFB and found that iron-doped carbon-nitrogen materials exhibit better wettability and permeability, leading to improved electrolyte saturation. Effective bubble management not only improves the flow dynamics within the battery but also ensures that electrochemical reactions proceed unhindered, thus maintaining optimal performance.

While these approaches have demonstrated efficacy in mitigating HER and improving macroscopic battery performance, the fundamental mechanisms of bubble formation and distribution within the electrode microstructure remain relatively unexplored, largely due to limitations in experimental methodologies. Recently, advanced imaging techniques, especially synchrotron

X-ray tomography and radiography, have begun addressing these limitations. Bevilacqua et al. used synchrotron X-ray tomography to investigate the impact of compression ratio on the electrolyte distribution. They found that remaining air bubbles in the carbon felt material and compression ratios significantly influence electrolyte saturation [67]. Eifert et al. [65] presented a synchrotron-based experimental setup capable of in-situ imaging of electrolyte flow geometry and gas bubble formation, revealing correlations between electrolyte saturation and electrochemical response during cyclic voltammetry. Köble et al. [68] conducted pioneering work using deep-learning-based segmentation techniques to precisely quantify bubble distribution at the microscale in porous carbon electrodes, observing that bubbles preferentially nucleate at electrode edges and cutting surfaces, thus highlighting the role of electrode heterogeneity in bubble formation. Li et al. [58] employed in-situ transparent VRFB cells to capture the sequential processes of hydrogen bubble nucleation, growth, coalescence, and eventual blockage of electrolyte transport pathways.

1.4.2. Numerical Modeling of Gas Evolution

Numerical modeling has played a crucial role in elucidating the effects of HER on VRFB performance. Initial numerical investigations into HER in VRFB systems began as early as 2010, when Shah et al. [69] developed the first two-dimensional transient multiphase computational model that integrated mass transport, momentum conservation, and electrochemical reaction kinetics. This pioneering model highlighted how HER significantly reduces the battery coulombic efficiency by consuming electrons intended for the primary vanadium reactions. However, their model overestimated the hydrogen evolution due to unsuitable HER kinetic parameters derived from alkaline conditions (originally reported by [70]), which are significantly different from the acidic environment of VRFBs. Additionally, the model lacked realistic representation of porous electrodes such as carbon felt, limiting its practical applicability. Qian et al. [71] employed an Eulerian-Eulerian multiphase model coupling species transport and electrochemical reactions to investigate parasitic gas evolution in VRFBs. By updated HER kinetic parameters, particularly the activation energy, they improved model accuracy, which demonstrated excellent agreement with Wei et al.'s experimental observations [58].

Despite significant progress, traditional numerical methods, such as finite volume methods and continuum-based multiphase flow models, faced inherent limitations when attempting to capture detailed microstructural processes, especially bubble dynamic behavior and interactions within complex porous electrodes. Recognizing these constraints, from approximately 2017 onwards, research began to adopt the Lattice Boltzmann Method (LBM) as a novel and powerful computational tool for simulating multiphase flow at the microscale. The LBM offers several distinct advantages over conventional computational methods: it naturally accommodates complex porous geometries without requiring complicated meshing strategies, allows for efficient parallel computation, and precisely captures the dynamic interface evolution between gas bubbles and electrolyte at the pore level.

Chen et al. [72] employed the pseudo-potential model of Shan and Chen [73, 74] LBM to simulate liquid-gas multiphase flow within porous fibrous electrodes. In their study, they first reconstructed a series of electrodes with varying fiber diameters and porosities, enabling the calculation and validation of permeability and diffusivity against established empirical relationships. Significantly, their simulations also examined the reactive surface area reduction resulting from gas bubble coverage. They systematically studied the influences of electrode porosity, fiber diameter, gas saturation, and electrode wettability, demonstrating a detailed dependence of these parameters on the average bubble size and subsequent reduction in reactive surface area. An important finding of their work was that gas coverage on solid surfaces was notably lower than previously assumed by macroscopic empirical models, suggesting an overestimation of bubble-related performance losses in earlier studies.

Subsequently, Zhang et al. [75] extended the application of LBM to explore the effects of electrode wettability on VRFB performance. Specifically, they modeled bubble dynamics within three-dimensional carbon paper electrodes, highlighting the detrimental impact of bubble trapping due to limited wetted areas. They quantitatively demonstrated that wettability significantly influences battery performance, particularly by affecting polarization losses associated with increased concentration polarization and activation overpotential. However, their model was limited to structural considerations without integrating reaction kinetics explicitly, indicating a gap between physical transport phenomena and electrochemical reaction coupling.

Further bridging this gap, Zhang et al. [76] developed an experimentally validated three-dimensional

pore-scale LBM framework to comprehensively describe the interplay between electrode microstructure, multiphase transport, and electrochemical reactions within redox flow batteries. This study combined LBM simulations with X-ray computed tomography (CT) measurements, successfully capturing coupled fluid transport and electrochemical reactions at the electrode-electrolyte interface. Validation against experimental data confirmed the model's accuracy in predicting electrode performance under realistic operational conditions. Their results provided a systematic analysis of how pore-scale structures influence electrochemical performance, further underscoring the importance of accurately resolving multiphase interactions within electrode structures.

Overall, these numerical studies have progressively refined the description of multiphase phenomena within VRFB electrodes. However, despite these advances, previous works have not explicitly simulated the detailed, dynamic bubble evolution processes triggered specifically by the HER. Recognizing this critical research gap, our current study represents the first attempt to apply a lattice Boltzmann model to capture and visualize bubble nucleation and evolution processes driven explicitly by HER at the microscale. This novel numerical approach offers interesting detail and insights, directly linking reactions to microscale multiphase transport phenomena within VRFB electrodes.

1.5. Aims of present research

Despite extensive research on VRFBs, there remains a significant knowledge gap in understanding HER-induced gas evolution and its impact on electrode performance. Existing studies have provided insights into bubble formation, electrolyte flow, and mass transport limitations; however, comprehensive investigations that integrate experimental observations with numerical simulations to achieve a more complete understanding of bubble dynamics are still limited. Although our experimental and numerical approaches are independently performed and do not directly validate each other, the numerical simulations in this work complement the experimental findings by capturing phenomena that are challenging to observe experimentally. Specifically, our LBM simulations provide detailed insights into bubble nucleation and transient evolution processes, thereby enabling a more comprehensive and multi-faceted analysis of

bubble dynamics in VRFBs.

This dissertation aims to integrate high-resolution imaging, deep learning-based image processing, and LBM simulations to advance the understanding of HER-driven bubble dynamics in VRFBs. The findings of this study will contribute to improving VRFB performance and durability, paving the way for their large-scale deployment in renewable energy systems.

While synchrotron X-ray studies provide valuable spatial resolution of bubble formation sites and distribution, most existing research focuses primarily on macroscale observations or bubble aggregations. There remains a significant research gap regarding the detailed characterization of individual bubble morphology, including their sizes, shapes, nucleation mechanisms, and transient dynamics within porous electrodes. No existing study has provided a complete microscopic picture of how bubbles individually evolve or how their morphology impacts fluid transport at the pore scale. Addressing this gap is essential, as bubble dynamics fundamentally influence electrolyte distribution and electrochemical reaction uniformity.

To overcome these limitations, our work uniquely adopts three-dimensional synchrotron imaging combined with advanced image-processing techniques. For the first time, we visualize and characterize individual bubble morphologies within carbon-felt electrodes under realistic operating conditions, capturing the detailed process of bubble formation, growth, coalescence, and detachment. This comprehensive, micro-scale understanding represents a significant step beyond previous experimental studies, providing novel insights that will inform future electrode and flow-field designs, thus significantly improving the operational efficiency and longevity of VRFB systems.

2. Experimental Methodology

2.1. Methodological Overview

This study combines experimental observation, image analysis, and numerical simulation to investigate gas bubble dynamics and their interaction with porous electrode microstructures in VRFB systems. The methodology is divided into two work parts, as illustrated in Figure 2.1.

The first work part focuses on the characterization of hydrogen bubble evolution during the HER. Synchrotron X-ray tomography was conducted in collaboration with Prof. Roswitha Zeis' group using a custom-designed VRFB cell. The acquired image datasets were manually annotated by the author and then used to train and validate a deep learning-based segmentation pipeline. Bubble distribution data were further processed using ITK-based post-processing and analyzed to extract quantitative morphological features.

To investigate the interaction between bubbles and the electrode microstructure, the second part of the work focused on simulations based on the lattice Boltzmann method. Synchrotron X-ray imaging of compressed carbon felt was performed to obtain the structural basis for fluid simulation, which was conducted by Prof. Roswitha Zeis' group. Then I reconstructed the electrode microstructure from the tomographic data and used this as input for pore-scale modeling based on LBM. All simulation work, including preprocessing, model development, and post-analysis, was performed by the author of this thesis.

Together, these two components provide a comprehensive framework for understanding gas evolution phenomena and their coupling with transport-limiting features in porous electrodes.

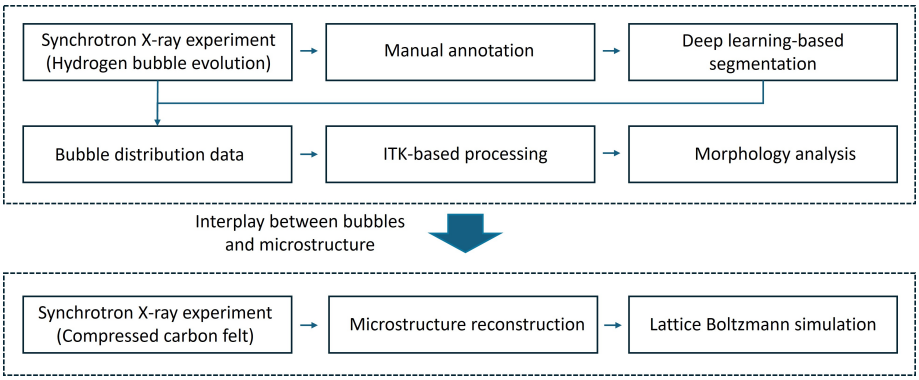

Figure 2.1.: Schematic workflow of the experimental and computational methodology. The first part (top) illustrates the hydrogen bubble imaging and analysis pipeline, combining synchrotron X-ray tomography, manual labeling, deep learning-based segmentation, and morphology evaluation. The second part (bottom) shows the microstructure-based simulation framework, which includes compressed carbon felt imaging, microstructure reconstruction, and pore-scale Lattice Boltzmann modeling. The linkage between the two parts emphasizes the interplay between bubble behavior and electrode structure.

2.2. Hydrogen Evolution Reaction (HER) Experiment and Bubble Analysis

The experimental procedures and imaging conditions described in this section are based on synchrotron X-ray studies in which the author was actively involved in image data processing and analysis [68, 77].

2.2.1. Experimental Setup

A synchrotron-adapted VRFB cell [65], specifically designed for synchrotron X-ray imaging experiments, was used to observe gas bubbles in a carbon felt electrode. These include residual air bubbles from incomplete electrolyte filling and hydrogen gas formed by applying negative potentials to initiate HER. A commercial graphitized carbon felt (SIGRACELL® GFD 4.6 EA, SGL Carbon) based on a polyacrylonitrile precursor was selected as the electrode and thermally treated according to a standard procedure at 400 °C for 25 h [66, 78–80]. The vanadium (IV) electrolyte used in the experiments was prepared by dissolving 0.1 mol/L $VOSO_4$ (99.9% metal-based, Thermo Fisher) in 2 mol/L H_2SO_4 (96%, Suprapur®, Merck). The oxidation state of the electrolyte was considered constant, due to the large volume of the reservoir compared

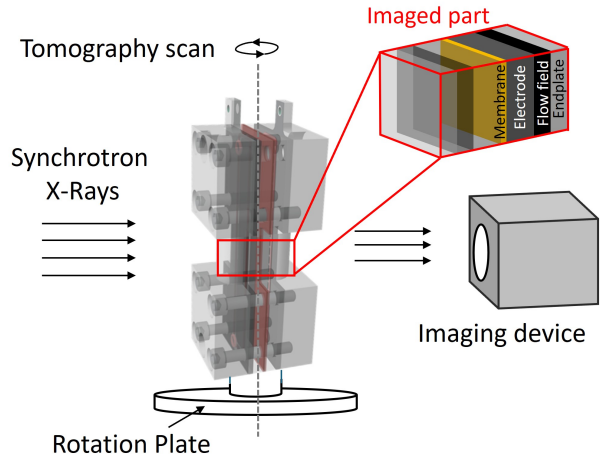

Figure 2.2.: Schematic of Synchrotron X-ray scanning setup for HER experiment

to the electrode and the short reaction time.

Figure 2.2 shows the schematic of the scanning experiment. During each measurement, the cell was placed on a high-precision air-bearing rotation stage, allowing fine alignment with the beam. Tomograms were collected before and after electrolyte injection using 2000 projections at 200 fps (frames per second). Dark field and flat field images were used to correct thermal noise and pixel sensitivity. In each experimental cycle, the electrolyte was first pumped into the battery at a constant rate until the open circuit voltage (OCV) stabilized, and no gas bubbles were observed at the outlet pipe. A reference tomogram was then collected while maintaining the battery under OCV and ensuring proper electrical contact. Subsequently, a constant negative potential was applied to induce HER. After maintaining the potential for three minutes, the potential control was switched off, and a second scan was conducted. This procedure constituted one experimental cycle for a given voltage condition. The electrode potential was then decreased stepwise by 25 mV from –175 mV to –300 mV, repeating the same sequence at each voltage level.

Measurements were performed using a white beam from a superconducting wiggler at the IMAGE beamline of the KIT Light Source. The wiggler provided a photon flux up to 1.7×10^{15} ph s^{-1} mm^{-2} and energy up to 180 keV. After filtering with 6 mm pyrolytic graphite, a flux of 2.7×10^{13} ph s^{-1} mm^{-2} at the sample position and a spectrum centered at 14.5 keV

was obtained. To enhance the contrast, a free-space propagation distance of 40 cm was set between the sample and detector. The detector pixel size was 4.5 µm, with a system resolution of 9 µm [65, 81].

2.2.2. Image Processing

Tomography scans were performed over 180° and then reconstructed using the Tofu image processing toolkit, to get the three-dimensional (3D) volume of bubbles in the electrode [82]. To better distinguish the voids from the remaining components, the 3D reconstruction was performed with phase retrieval [83].

To standardize and facilitate image segmentation, a sufficient number of images were annotated manually to train a two-dimensional U-Net segmentation model with a ResNet-34 backbone [84, 85], as show in Figure2.3. Subsequently, this model was employed to identify and label the bubbles, the membrane, and the gaskets around the membrane for the remaining experimental data. The results obtained from the deep learning model were thoroughly examined and manually aligned when required. An accurate mask of the electrode volume is essential for further analysis since the uneven membrane and the gaskets define the border of the non-cuboid electrode shape. The overall volume fraction of bubbles within the electrode was determined by calculating the ratio of the bubble volume to the electrode volume, both measured in voxels. This calculation was applied to all tomograms, enabling a comprehensive comparison between the initial and bubble distributions after the HER.

2.2.3. Bubble Morphological Characterization

After segmenting the detected bubbles in the working electrode using the deep learning model, the Insight Segmentation and Registration Toolkit (ITK) was employed to analyze the bubbles' sizes, shapes, and statistical distributions [86]. The bubble shape was characterized in terms of roundness, elongation, and flatness [87].

For computational efficiency, consistency, and comparability, the bubble's equivalent radius r_{eq} and boundary length P are used to determine the roundness R_{d}. The equivalent radius r_{eq} is calculated from the actual volume V of the respective bubble, which represents the total

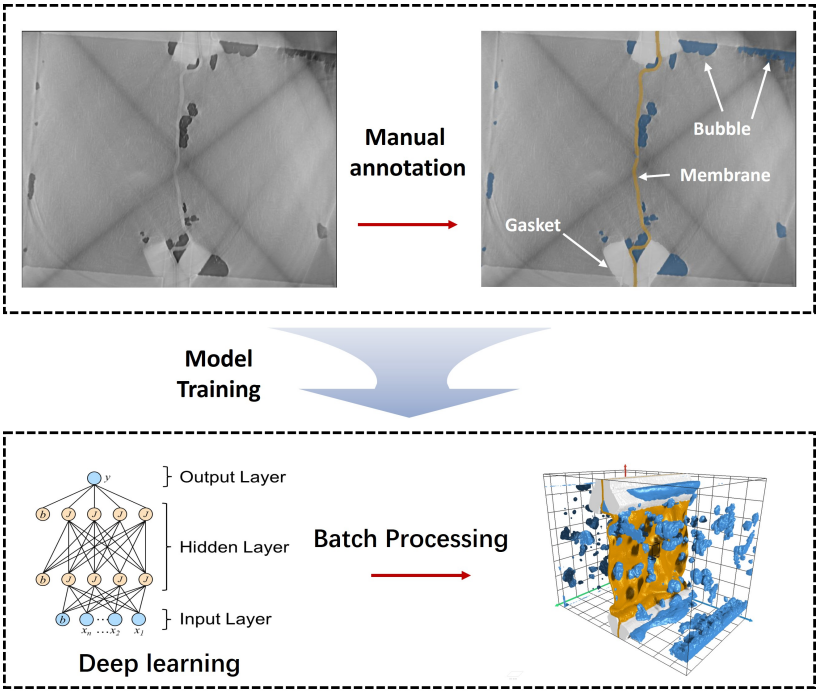

Figure 2.3.: Workflow of image processing

number of voxels comprising the bubble. For the calculation, it is assumed that each bubble is a perfect sphere with the same volume V. The equivalent radius r_{eq} can thus be derived from the volume formula of a sphere,

$$r_{\text{eq}} = \left(\frac{3V}{4\pi}\right)^{1/3} \tag{2.1}$$

The bubble's boundary length P corresponds to the estimated perimeter of the bubble in a plane determined by its principal axis direction. In a 3D image, bubble boundaries are typically composed of discrete pixels. The ITK employs a method based on intercept counts (also known as discretized boundary counts) to estimate the boundary length P. This method estimates the perimeter by scanning the volumetric data, counting the number of planes or lines intersecting the bubble boundary, and multiplying by the pixel pitch of the image.

Although this technique does not yield an exact perimeter calculation, it provides a meaningful measure of the complexity of the bubble shape. Finally, the roundness R_{d} of each bubble is

calculated by dividing its equivalent circumference by the estimated boundary length,

$$R_{\mathrm{d}} = \frac{2\pi r_{\mathrm{eq}}}{P} \tag{2.2}$$

Elongation and flatness refer to the size difference of the bubble in the direction of the three principal axes. First, the centroid of the bubble, described by the coordinates x_c, y_c, and z_c, was determined by calculating its first moment (Eqs. 2.3–2.5). Then, the second covariance matrix of the bubble was calculated, which describes the distribution of bubbles in the three principal axis directions,

$$x_c = \frac{\sum x\, m(x,y,z)}{\sum m(x,y,z)}, \tag{2.3}$$

$$y_c = \frac{\sum y\, m(x,y,z)}{\sum m(x,y,z)}, \tag{2.4}$$

$$z_c = \frac{\sum z\, m(x,y,z)}{\sum m(x,y,z)} \tag{2.5}$$

where m is the local binary value of the segmented images. Then, the second covariance matrix of the bubble was calculated, which describes the distribution of bubbles in the three principal axis directions. The principal axes and their lengths are determined by computing the eigenvalues and eigenvectors of the centered second-order matrix. This process can be expressed as

$$A^{\mathrm{T}} A\, \xi = \lambda\, \xi, \tag{2.6}$$

where A describes the position of all voxels relative to the centroid, and A^{T} denotes the transpose of matrix A. Using the centered second-order matrix, the principal axes and their lengths are obtained by performing eigenvalue decomposition, as shown in Eq. 2.6. The eigenvalue matrix λ and eigenvector matrix ξ are obtained accordingly. The eigenvalues are sorted in ascending order as $\lambda_1 \leq \lambda_2 \leq \lambda_3$ and paired with their corresponding eigenvectors to define the three principal directions. The axis length is inversely related to its eigenvalue, meaning the longest axis (main axis) corresponds to the smallest eigenvalue λ_1. The elongation E is calculated as the square root of the ratio between the largest and middle eigenvalues (λ_3 and λ_2), while the flatness F is defined by the square root of the ratio between the middle and

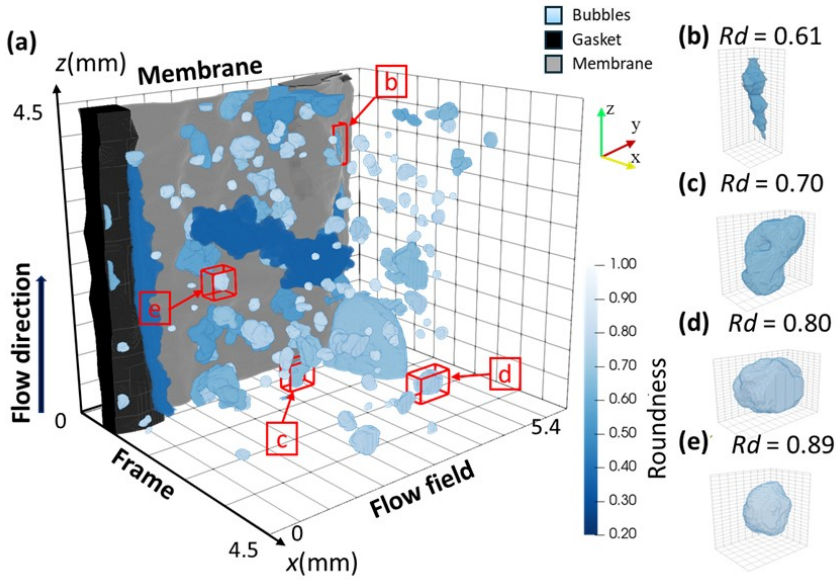

Figure 2.4.: (a) 3D visualization of bubble distribution at −250 mV color-coded by roundness; (b)–(e) Representative individual bubbles showing distinct shape characteristics.

smallest eigenvalues (λ_2 and λ_1), as follows:

$$\text{Elongation} = \sqrt{\frac{\lambda_3}{\lambda_2}}, \tag{2.7}$$

$$\text{Flatness} = \sqrt{\frac{\lambda_2}{\lambda_1}}. \tag{2.8}$$

Figure 2.4(a) shows an example of a 3D visualization of the segmented bubble distribution within the electrode. The visualization domain spans $600 \times 500 \times 500$ voxels. The electrode volume is bounded by two frames along the yz plane, the membrane at the back along the xz plane, and the flow field at the front along the xz plane. The electrolyte flow proceeds in the direction of the z-axis. In this specific example, the bubble colors represent their calculated roundness values. Four individual bubbles with distinct shapes were extracted from the 3D distribution and enlarged to a similar display scale, as shown in Figures 2.4(b)–(e). These examples illustrate specific values of roundness, flatness, and elongation derived from the aforementioned calculations for reference. The detailed morphological characteristics of these bubbles are summarized in Table 2.1. It is worth noting that the same color code will be

consistently used in later chapters to indicate bubble geometrical properties and their spatial distribution within the electrode volume.

Table 2.1.: Shape characteristic values of selected bubbles in Figure 2.4

Bubble	Volume (pixels)	Elongation	Flatness	Roundness
(b)	3969	2.13	2.06	0.61
(c)	15036	1.99	1.49	0.70
(d)	33147	1.57	1.34	0.80
(e)	9395	1.10	1.31	0.89

2.3. Microstructure Characterization for Simulation

The experimental procedures and imaging conditions described in this section are based on synchrotron X-ray studies previously conducted by Prof. Roswihta's gruop [67]. The microstructure reconstruction from dry-state tomography images, as well as all subsequent simulation setup and modeling, were independently performed by the author.

2.3.1. Experimental Setup

To obtain the microstructural geometry needed for the simulations, tomography images of dry carbon felt electrodes were used. In this study, only the dry-state scans were used, which is captured before any electrolyte was introduced.

The carbon felt electrodes (GFA 6EA, SIGRACELL®, SGL Carbon, Germany) were thermally treated in air at 400 °C for 25 h, following the same procedure as in the HER experiments [66, 78–80]. Figure 2.5 shows the setup used for synchrotron X-ray tomography of the dry electrodes. This non-destructive method enables high-resolution, three-dimensional imaging of the internal structure of the electrode.

The carbon felts were cut into cylindrical samples with a diameter of 3 mm and mounted in a custom sample holder. The compression ratio (CR) of each sample was adjusted by stacking stainless steel washers and polyethylene naphthalate films of known thickness. The outer housing of the holder could move independently of the central shaft, which also contained

the electrolyte flow pipe. This design allowed for precise control of the sample thickness by adjusting the height of the stacked spacers.

Compression ratios of 25%, 50%, and 70% (relative to the uncompressed felt thickness) were applied to the samples. A minimum compression of 25% was chosen to ensure good contact between the electrode and the current collector in practical applications [88, 89]. For each compression level, tomography scans were taken before any liquid was introduced.

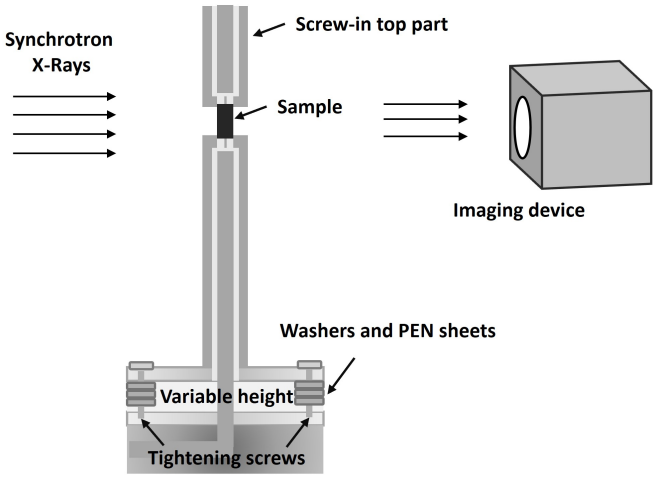

Figure 2.5.: Schematic of synchrotron X-ray scanning setup for compressed carbon felt electrode.

The experiments were carried out at the Topo-Tomo beamline of the Karlsruhe Research Accelerator (KARA, Germany). The uncompressed electrode was scanned with a resolution of $2015 \times 2015 \times 2015$ voxels, and each voxel represents $2.44^3\ \mu m^3$, using a LuAg:Ce scintillator and a polychromatic X-ray beam centered at 13.5 keV. During scanning, the beam current remained above 70 mA. A total of 3000 radiographic projections were acquired over a 180° rotation with a step size of 0.06°.

2.3.2. Numerical Reconstruction

Figure 2.6(a) shows a representative two-dimensional grayscale image after pre-processing. The gray ring surrounding the porous structure corresponds to the tube that held the electrode during scanning [67]. The average diameter of the carbon fibers is approximately 10 µm, and the pore sizes are mostly in the range of 10 µm to 100 µm [67, 90]. Binary segmentation was

performed using ImageJ and the FIJI plugin by applying an intensity threshold to distinguish between pores (assigned as 0) and carbon fibers (assigned as 1). The threshold value was determined based on the theoretical porosity under different compression levels. This porosity can be calculated using the following equation [91]:

$$\varepsilon_{\text{comp}} = \frac{\varepsilon_0 - \zeta}{1 - \zeta} \tag{2.9}$$

where ε_0 is the original porosity (0.95 for GFA6 carbon felt), and ζ is the compression ratio.

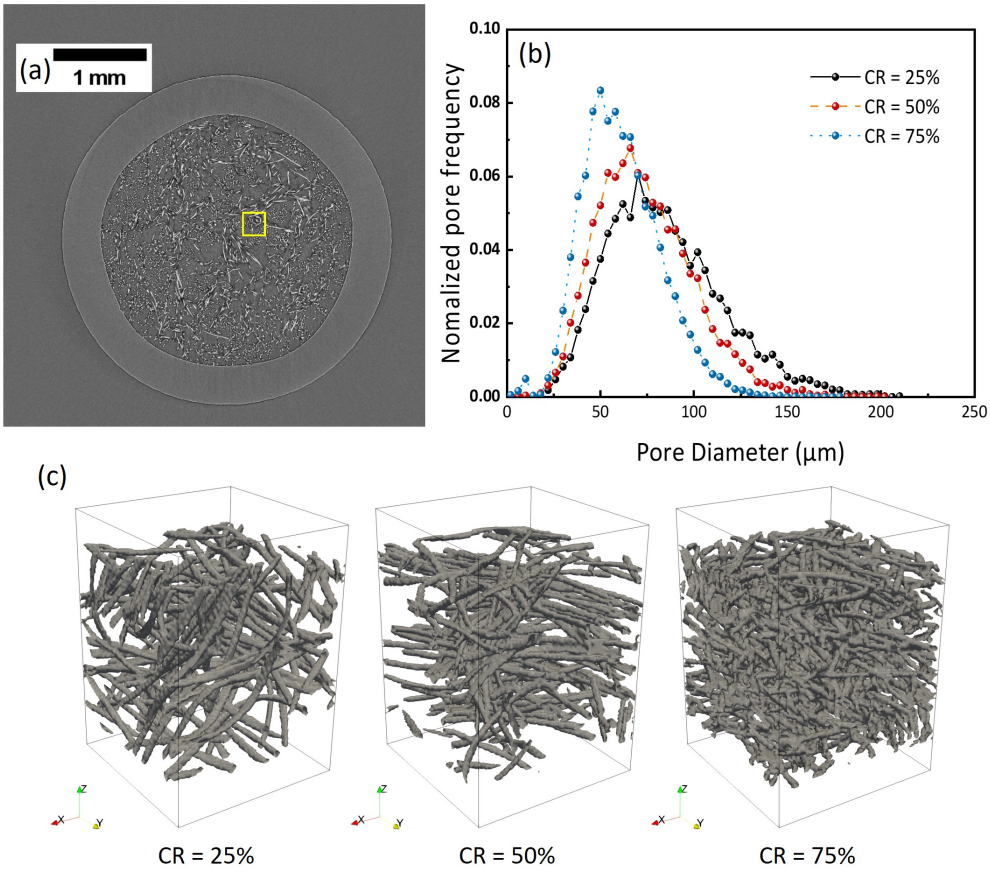

Figure 2.6.: (a) Synchrotron tomography image (yellow box indicates selected region); (b) pore size distribution under different compression ratios; (c) 3D visualizations of microstructures corresponding to different compression ratios.

To generate simulation geometries, a cubic region of 100^3 voxels was extracted from the center of the tomography data, as marked by the yellow box in Figure 2.6(a). Figure 2.6(b) shows

the pore size distributions at different compression ratios, and Figure 2.6(c) provides the three-dimensional reconstructions of the electrode structures used in subsequent simulations. In these images, the gray region represents the solid carbon fibers.

3. Lattice Boltzmann Method for Multiphase Flow

3.1. Introduction

The Lattice Boltzmann Method, a mesoscopic computational approach, has garnered substantial research interest in recent years [92]. Evolving from its predecessor lattice gas automata (LGA), this method has been widely adopted for simulating multiphase flows [93]. Unlike LGA models that track individual particle movements, LBM focuses on statistical velocity distribution functions, enabling efficient modeling of complex fluid interactions. Particularly effective in simulating two-phase flows through porous media, LBM demonstrates superior adaptability to intricate geometries compared to conventional macroscopic approaches (e.g., finite volume methods), offering simplified implementation of boundary conditions in complex domains.

3.2. Theoretical Background

3.2.1. Boltzmann Equation

The Boltzmann equation forms the theoretical backbone of LBM, describing the statistical behavior of a large number of particles in a fluid system. To bridge the microscopic particle motion with macroscopic fluid dynamics, Ludwig Boltzmann introduced a probability-based approach to model how particles are distributed in phase space over time [94]. Considering a dilute gas in a three-dimensional domain, where an infinitesimal control volume located at position $\mathbf{x}$ contains N particles at time t, each particle possesses a velocity vector $\boldsymbol{\xi}_i = (u, v, w)$, where

$i = 1, 2, \ldots, N$. The number of particles with velocities within the range $\boldsymbol{\xi}$ to $\boldsymbol{\xi} + d\boldsymbol{\xi}$ and located within the spatial interval $d\mathbf{x}$ is given by:

$$N = f(x, \xi, t)\, dx\, d\xi. \tag{3.1}$$

Here, $f(\mathbf{x}, \boldsymbol{\xi}, t)$ is the velocity distribution function, which represents the probability of finding a particle at position $\mathbf{x}$ with velocity $\boldsymbol{\xi}$ at time t. The goal is to derive an equation governing the evolution of f over time. Solving such an equation allows the determination of the velocity distribution function at any given moment.

The first macroscopic property, density ρ, is derived from the velocity distribution function. Considering each particle has a mass m and and that the total number of particles in a volume element $\Delta\mathbf{x}$ can be obtained by integrating the distribution function $f(\mathbf{x}, \boldsymbol{\xi}, t)$ over velocity space, the mass density ρ, defined as mass per unit volume, is given by [95]:

$$\rho = \lim_{\Delta x \to 0} \frac{Nm}{\Delta x} = m \int_{-\infty}^{+\infty} f(x, \xi, t)\, d\xi. \tag{3.2}$$

All macroscopic properties, such as density, velocity, pressure, can be derived from the velocity distribution function through its moments. To determine these properties at any given instant, it is necessary to know how the distribution function evolves. This evolution is governed by the Boltzmann equation.

Before introducing the Boltzmann equation, the concept of the velocity distribution function is generalized to a system of N particles. In such a system, the full distribution function f_N is defined in the $6N$-dimensional phase space $(\mathbf{q}, \mathbf{p})$ and gives the probability that the system lies within an infinitesimal volume element $d\mathbf{q}\, d\mathbf{p}$. Here, $\mathbf{q} = (\mathbf{q}_1, \mathbf{q}_2, \ldots, \mathbf{q}_N)$ denotes the generalized spatial coordinates of the N particles and $\mathbf{p} = (\mathbf{p}_1, \mathbf{p}_2, \ldots, \mathbf{p}_N)$ denotes their corresponding conjugate momenta. The evolution of f_N is governed by the Liouville equation [96]:

$$\frac{\partial f_N}{\partial t} + \sum_{j=1}^{N} \left(\frac{\partial H_N}{\partial \mathbf{q}_j} \cdot \frac{\partial f_N}{\partial \mathbf{p}_j} - \frac{\partial H_N}{\partial \mathbf{p}_j} \cdot \frac{\partial f_N}{\partial \mathbf{q}_j} \right) = 0, \tag{3.3}$$

where H_N is Hamiltonian of the system. From f_N, reduced s-velocity distribution functions can be defined by integrating over the coordinates and momenta of the remaining $(N - s)$

particles [97]:

$$F_s(\mathbf{q}_1, \mathbf{p}_1, \ldots, \mathbf{q}_s, \mathbf{p}_s) = \int f_N(\mathbf{q}_1, \mathbf{p}_1, \ldots, \mathbf{q}_N, \mathbf{p}_N)\, d\mathbf{q}_{s+1} d\mathbf{p}_{s+1} \ldots d\mathbf{q}_N d\mathbf{p}_N. \tag{3.4}$$

This construction leads to the BBGKY (Bogoliubov–Born–Green–Kirkwood–Yvon) hierarchy. The first equation in the chain describes the evolution of the single-velocity distribution function and includes the two-particle distribution. In general, the s-th equation in the hierarchy involves the $(s+1)$-particle distribution. Solving the full hierarchy is as difficult as solving the original Liouville equation, but under certain assumptions, it is possible to truncate the hierarchy at first order, ultimately yielding the well known Boltzmann equation for velocity distribution function f, which is defined as.

$$f(x, \xi, t) = mNF_1(\mathbf{q}_1, \mathbf{p}_1, t), \tag{3.5}$$

where notation has been changed from phase space to physic space: $x = \mathbf{q}_1$ is the position of particle and $\xi = \mathbf{p}_1/m$ is the velocity. Boltzmann equation is the required equation for evolution of velocity distribution function, which is described by total time derivative of f:

$$\frac{df}{dt} = \frac{\partial f}{\partial t} + \frac{\partial f}{\partial x_\beta}\frac{dx_\beta}{dt} + \frac{\partial f}{\partial \xi_\beta}\frac{d\xi_\beta}{dt}. \tag{3.6}$$

where subscript β represents the direction in velocity space. The particle velocity is expressed as:

$$\frac{dx_\beta}{dt} = \xi_\beta, \tag{3.7}$$

and particle acceleration is related to external forces as follows:

$$\frac{d\xi_\beta}{dt} = \frac{F_\beta}{\rho}. \tag{3.8}$$

These equations reflect the principle of molecular chaos, as the velocities of colliding particles are independent of their positions. The Boltzmann equation can be derived under the following approximations:

1. Only binary particle collisions are considered.

2. The velocities of two colliding particles are uncorrelated before collision.

3. External forces do not affect local collision dynamics.

If no collisions occur between particles, the right-hand side of the above equation is zero, giving:

$$\frac{df}{dt} + \xi_\beta \frac{\partial f}{\partial x_\beta} + \frac{F_\beta}{\rho} \frac{\partial f}{\partial \xi_\beta} = 0 \tag{3.9}$$

However, in real fluids, collisions between particles occur, leading to both loss and gain of particles with velocities between $\boldsymbol{\xi}$ and $\boldsymbol{\xi} + d\boldsymbol{\xi}$, represented as [95]:

$$\frac{df}{dt} + \xi_\beta \frac{\partial f}{\partial x_\beta} + \frac{F_\beta}{\rho} \frac{\partial f}{\partial \xi_\beta} = \Omega(f) \tag{3.10}$$

where Ω is the collision operator. In the Boltzmann model, particles behave like billiard balls, with each collision causing an abrupt change in velocity.

3.2.2. BGK Approximation

The original Boltzmann equation describes all possible outcomes of binary collisions, resulting in a complex and mathematically demanding collision operator. While this formulation is appropriate for dilute gases, it becomes less practical for liquids, where the much higher particle density leads to more complex interactions involving three or more molecules.

At first glance, it might seem necessary to include these higher-order interactions through more complicated integrals. However, this is not required when the goal is to recover the correct macroscopic behavior, such as mass, momentum, and energy conservation, which can be obtained from the moments of the distribution function. These moments are essentially weighted integrals of the distribution function in velocity space, and many different functions can yield the same moment values.

This insight that the exact microscopic details are not essential for capturing macroscopic dynamics, allows for a major simplification of the collision operator. Specifically, the use of a discrete velocity model enables the replacement of the continuous velocity space with a small number of discrete velocity directions, while still preserving the correct macroscopic equations.

As a first step in this simplification, the distribution function f is decomposed into an equilibrium part f^{eq} and a non-equilibrium part f^{neq} [95]:

$$f = f^{eq} + f^{neq} \tag{3.11}$$

This separation forms the foundation for constructing simplified collision models that are easier to implement numerically without sacrificing physical accuracy at the macroscopic level.
In the fluid-dynamic approximation of the Boltzmann equation, it is assumed that the mean free path of particles is much smaller than the characteristic length scale of the system, i.e., $Kn \ll 1$. In this case, it can be approximated that the equilibrium velocity distribution function f^{eq} follows the Maxwell distribution function for monatomic gases [98, 99]:

$$f^{eq}(\boldsymbol{\xi}) = \rho \left(\frac{m}{2\pi k_B T} \right)^{3/2} \exp \left(-\frac{m|\boldsymbol{\xi} - \mathbf{u}|^2}{2k_B T} \right) \tag{3.12}$$

where k_B is the Boltzmann constant. The distribution function for equilibrium disturbance f^{neq} can be approximated as the first Chapman-Enskog expansion of the distribution function f. By assuming that each collision drives the velocity distribution function proportionally away from equilibrium, the collision operator can be conceptualized. The collision operator typically used in LBM is based on the much simpler Bhatnagar-Gross-Krook (BGK) collision operator [100].

$$\Omega(f) = -\frac{1}{\tau}(f - f^{eq}) \tag{3.13}$$

This operator directly captures the relaxation of the distribution function toward equilibrium. The time constant τ that determines this equilibrium velocity is called the relaxation time. The value of τ directly determines transport coefficients such as viscosity and thermal diffusivity. Physically, it represents the tendency of the velocity distribution function f to approach the equilibrium state f^{eq} after some time. This process is also called relaxation to equilibrium. Therefore, the BGK form of the Boltzmann equation is also known as single relaxation time approximation.

$$\frac{df}{dt} + \xi_\beta \frac{\partial f}{\partial x_\beta} + \frac{F_\beta}{\rho} \frac{\partial f}{\partial \xi_\beta} = -\frac{1}{\tau}(f - f^{eq}) \tag{3.14}$$

3.2.3. Lattice Boltzmann Equation

It is well known that hydrodynamic equations are generally difficult to solve, and analytical solutions can only be found for very basic cases such as Couette or Poiseuille flow. For cases with more complex geometries and boundary conditions, numerical methods must be employed. However, numerical methods for solving hydrodynamic equations are both difficult to implement and challenging to parallelize. Since the Boltzmann equation can recover the hydrodynamic equations at the macroscopic level, the solution to the Navier-Stokes equations for a given scenario can in principle be obtained from the solution of the Boltzmann equation. The problem is that solving the Boltzmann equation analytically is even more difficult than solving the hydrodynamic equations, because its fundamental variable is the velocity distribution function - a function of seven parameters. Therefore, numerical methods must be employed to solve the Boltzmann equation, from which the solution to the hydrodynamic equations can be indirectly obtained.

The lattice Boltzmann equation is a discretized form of the Boltzmann equation. The discretized Boltzmann equation is not only easier to implement but also offers certain numerical advantages compared to conventional methods that directly discretize hydrodynamics (such as finite difference or finite volume methods). The main difficulty with these methods lies in discretizing the convection term. To address this, they introduce complex iterative numerical schemes with approximation errors. In contrast, the discrete Boltzmann equation takes a completely different approach, leading to more accurate convection. First, the velocity distribution function $f(\mathbf{x}, \boldsymbol{\xi}, t)$ is reduced to a discrete distribution function $f_i(\mathbf{x}, t)$ in physical space and time. Then the velocity space is discretized so that each discrete distribution function has an associated discrete velocity $\mathbf{e}_i$. The discretized form is:

$$f_i(\mathbf{x} + \mathbf{e}_i \delta t, t + \delta t) = f_i(\mathbf{x}, t) - \frac{f_i(\mathbf{x}, t) - f_i^{\mathrm{eq}}(\mathbf{x}, t)}{\tau} \tag{3.15}$$

The mass density ρ and momentum density $\rho\mathbf{u}$ at $(\mathbf{x}, t)$ can be obtained through weighted sums of moments of f_i:

$$\rho = \sum_i f_i \tag{3.16}$$

$$\rho \mathbf{u} = \sum_i f_i \mathbf{e}_i \tag{3.17}$$

The discrete velocities $\mathbf{e}_i$ require further explanation. Together with their corresponding weight coefficients w_i, they form the velocity set $\{\mathbf{e}_i, w_i\}$. Different velocity sets are used for different purposes. These velocity sets are typically denoted by DdQq, where d is the spatial dimension covered by the velocity set and q is the number of velocities in the set. The most commonly used velocity sets for solving the Navier-Stokes equations are D1Q3, D2Q9, D3Q15 and D3Q27. In this work, we adopt the D3Q19 model (shown in Figure 3.1), where $c_s = 1/\sqrt{3}$ ($\delta r = \delta t = \delta = 1$). The corresponding subset velocities and weights are given below:

$$\mathbf{e}_i = \begin{cases} (0,0,0) & i = 0 \\ (\pm 1,0,0),(0,\pm 1,0),(0,0,\pm 1) & i = 1-6 \\ (\pm 1,\pm 1,0),(\pm 1,0,\pm 1),(0,\pm 1,\pm 1) & i = 7-18 \end{cases} \tag{3.18}$$

$$w_i = \begin{cases} 1/3 & i = 0 \\ 1/18 & i = 1-6 \\ 1/36 & i = 7-18 \end{cases} \tag{3.19}$$

The Taylor expansion form of Equation (3.12) can be used to calculate the equilibrium density

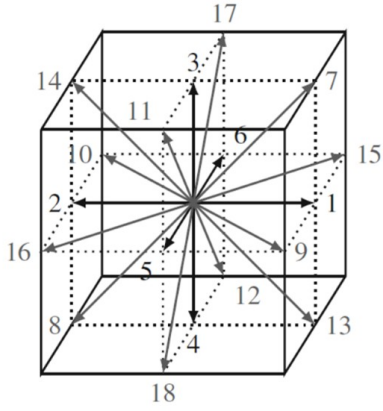

Figure 3.1.: Schematic of velocity vectors in the D3Q19 lattice Boltzmann model

distribution within the LBM framework, which is defined as:

$$f_i^{eq} = w_i \rho \left[1 + \frac{\mathbf{e}_i \cdot \mathbf{u}}{c_s^2} + \frac{(\mathbf{e}_i \cdot \mathbf{u})^2}{2c_s^4} - \frac{\mathbf{u}^2}{2c_s^2} \right] \tag{3.20}$$

where $\mathbf{e}_i$ is the lattice speed vector, corresponding to unit lattice space and unit lattice time. The lattice Boltzmann method mainly consists of two parts: collision and streaming. The right-hand side of Equation (3.15) represents the collision process of particles in the simulated system; the left-hand side corresponds to the streaming process, which captures the migration of particles to their neighboring lattice spaces after collision. Figure 3.2 shows a schematic of the LBM cycle.

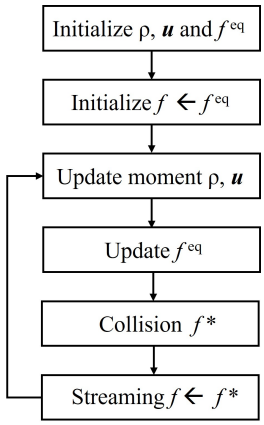

Figure 3.2.: An overview of one cycle of the LB algorithm.

3.3. Color-Gradient Model for Immiscible Two-Phase Flow

The color-gradient lattice Boltzmann model is one of the earliest approaches developed for simulating immiscible multiphase flows. It was first proposed by Gunstensen et al. [101]. Grunau et al. [102] later extended the model to support variations in fluid density and viscosity. A key advantage of the color-gradient model is that surface tension and viscosity ratio can be controlled independently, making it suitable for a wide range of flow conditions. Compared to the Shan–Chen pseudopotential model [103], which is widely used for its simplicity and ease of implementation, the color-gradient model offers better control over interface properties. While

the pseudopotential model is often limited to cases with small density and viscosity contrasts, the color-gradient model is more flexible in this regard. However, in this work, only moderate density and viscosity ratios are considered. In the present work, a three-dimensional 19 velocity (D3Q19) color-gradient lattice Boltzmann model is adapted to investigate the immiscible two-phase flow, which is developed based on the work by Leclaire et al. [104, 105]. The evolution equation for the distribution function is given by

$$f_i(\mathbf{x} + \mathbf{e}_i\,\delta t,\ t + \delta t) = f_i(\mathbf{x}, t) + \Omega_i + F_i, \tag{3.21}$$

where $f_i(\mathbf{x}, t)$ is the single velocity distribution function at lattice site $\mathbf{x}$ and time t, $\mathbf{e}_i$ is the discrete velocity in the i-th direction, Ω_i is the collision operator, and F_i represents the forcing term. Here, the time increment δt and lattice spacing δx are taken as unity. In this model, two sets of distribution functions, f_i^r (red) and f_i^b (blue), are introduced to represent the two different fluids. The total distribution function is defined as

$$f_i = f_i^r + f_i^b. \tag{3.22}$$

The collision operator Ω_i consists of three parts,

$$\Omega_i = \Omega_i^{\mathrm{BGK}} + \Omega_i^{\mathrm{pert}} + \Omega_i^{\mathrm{rec}}, \tag{3.23}$$

where Ω_i^{BGK} is the single-phase collision operator, Ω_i^{pert} is the perturbation operator which generates an interfacial tension, and Ω_i^{rec} is the recoloring operator used to enforce phase segregation and to maintain an interface between components.

Based on the simple and popular Bhatnagar-Gross-Krook (BGK) collision operator, the single-phase collision operator is written as

$$\Omega_i^{\mathrm{BGK}} = -\frac{1}{\tau}\left(f_i - f_i^{\mathrm{eq}}\right), \tag{3.24}$$

where $\tau = 3\,\bar{\nu} + 0.5$ is the effective relaxation time. The mixed fluid viscosity $\bar{\nu}$ is defined via a harmonic density-weighted average of the red fluid kinematic viscosity ν_r and the blue fluid

kinematic viscosity ν_b.

$$\frac{1}{\bar{\nu}} = \frac{\rho_r}{\rho_r + \rho_b} \cdot \frac{1}{\nu_r} + \frac{\rho_b}{\rho_r + \rho_b} \cdot \frac{1}{\nu_b}, \tag{3.25}$$

The equilibrium distribution function f_i^{eq} is obtained by expanding the Maxwell–Boltzmann distribution in a Taylor series of the local fluid velocity $\mathbf{u}$ up to second order,

$$f_i^{\mathrm{eq}} = w_i \, \rho \left[1 + \frac{\mathbf{e}_i \cdot \mathbf{u}}{c_s^2} + \frac{(\mathbf{e}_i \cdot \mathbf{u})^2}{2c_s^4} - \frac{\mathbf{u} \cdot \mathbf{u}}{2c_s^2} \right], \tag{3.26}$$

where $c_s = 1/\sqrt{3}$ is the speed of sound, w_i is a weighting factor depending on the lattice direction ($w_0 = 1/3$, $w_{1-6} = 1/18$, $w_{7-18} = 1/36$), and ρ is the total density, with $\rho = \rho^r + \rho^b$, and ρ^r, ρ^b being the densities of the red and blue fluids, respectively. The density of each fluid is given by the zeroth moment of its distribution functions,

$$\rho^\alpha = \sum_i f_i^\alpha, \quad \alpha = r, \, b, \tag{3.27}$$

and their reference densities, ρ_0^r and ρ_0^b, are both set to 1 in lattice units (l.u.) in the present study. The total momentum is defined as the first moment of the color-blind distribution functions,

$$\rho \, \mathbf{u} = \sum_i f_i \, \mathbf{e}_i \; + \; \frac{\delta_t}{2} \, \mathbf{F}, \tag{3.28}$$

and the pressure is calculated as follows:

$$\mathbf{P} = c_s^2 \, \rho. \tag{3.29}$$

In the present study, a pressure gradient is introduced to drive the flow, which is modeled as a body force $\mathbf{F}$ using Guo's forcing scheme [106]. Phase separation is implemented using the color gradient method, which introduces an interaction between different fluid components resulting in the separation of phases in three steps [101, 104, 105]. In the first step, the direction of the steepest increase in the density of the respective fluid component (the color gradient) is calculated as

$$\mathbf{G} = \nabla \phi = \frac{3}{\delta t} \sum_i w_i \, \mathbf{e}_i \, \phi(t, \mathbf{x} + \mathbf{e}_i \, \delta t), \tag{3.30}$$

where ϕ is a so-called color function (order parameter) used to identify the interface. It is defined by

$$\phi = \frac{\rho^r - \rho^b}{\rho^r + \rho^b}. \tag{3.31}$$

In the subsequent perturbation step, populations aligned with the gradient of the density field of fluid component α are increased, while those perpendicular to the gradient are diminished, resulting in the emergence of surface tension:

$$\Omega_i^{\text{pert}} = A\,|\mathbf{G}|\left[w_i \frac{(\mathbf{e}_i \cdot \mathbf{G})^2}{|\mathbf{G}|^2} - B_i\right], \tag{3.32}$$

where $A = \frac{9\sigma}{4\tau}$ is a parameter (space- and time-dependent) that controls the interfacial tension σ at the fluid interface, and the weights B_i are chosen to ensure mass conservation.

$$B_i = \begin{cases} -2/9 & i = 0 \\ 1/54 & i = 1-6 \\ 1/27 & i = 7-18. \end{cases} \tag{3.33}$$

In the final step, known as the recoloring step, the two phases are separated by redistributing the two fluid populations in opposite directions:

$$f_i^r = \frac{\rho^r}{\rho} f_i + \beta \frac{\rho^r \rho^b}{\rho^2} \cos(\theta_i)\, f_i^{\text{eq}}(\rho, 0), \tag{3.34}$$

$$f_i^b = \frac{\rho^b}{\rho} f_i - \beta \frac{\rho^r \rho^b}{\rho^2} \cos(\theta_i)\, f_i^{\text{eq}}(\rho, 0), \tag{3.35}$$

where β controls the interface thickness, with $\beta = 0.99$ used in all simulations to keep the interface as thin as possible, and θ_i is the angle between the color gradient $\mathbf{G}$ and the lattice connectivity vector $\mathbf{e}_i$.

3.3.1. Validation

Two-phase model validation

In this study, the color-gradient model is validated with two standard benchmarks: Laplace's law and the Washburn capillary displacement. Figure 5.6(a) shows the Laplace test for three surface–tension values. The capillary pressure varies linearly with 1/R and the fitted slopes match the prescribed σ, confirming accurate interfacial tension. The lattice resolution used here is deliberately coarse so this test verifies performance under the intended mesh. Figure 5.6(b) compares the LBM results with the non-dimensional Washburn prediction for three imposed pressure gradients. All cases captured the underlying physics properly, where the fluids interface moved more rapidly at higher pressures, and it quickly moved at first, then slowed down as it progressed through the tube. Together, these benchmarks demonstrate that the model reliably captures capillarity-driven displacement in small pores at coarse resolution.

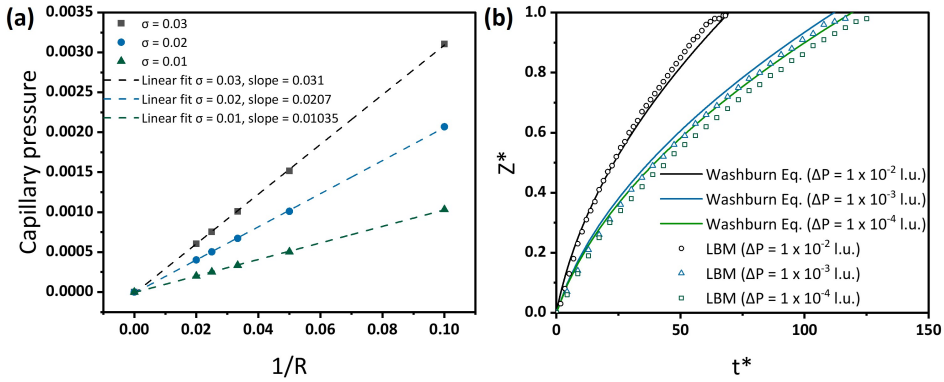

Figure 3.3.: Benchmarks: (a) Laplace law test results for three surface tension values; (b) comparison between the Washburn prediction and LBM simulations for three imposed pressure gradients.

Domain-size sensitivity

Figure 3.4 reports the average electrolyte saturation varies as the porous domain size increases (in lattice units), with error bars indicating maximum and minimum transient values. The 50^3 l.u. case exhibits noticeably larger error bars. We attribute this to the interaction of bubbles with the periodic sidewalls in a small domain, since truncated fibers at the periodic cuts

can create artificial pinning sites. As the domain size increase, average electrolyte saturation decreases mildly, consistent with longer internal pathways and reduced boundary influence. For sizes $\geq 100^3$ l.u., the average saturation and its variability stabilize; the change from 100^3 to 150^3 l.u. remains within 5-10%. We therefore adopt 100^3 l.u. as the baseline size, it is large enough to capture the relevant pore-scale patterns while saving the computational cost.

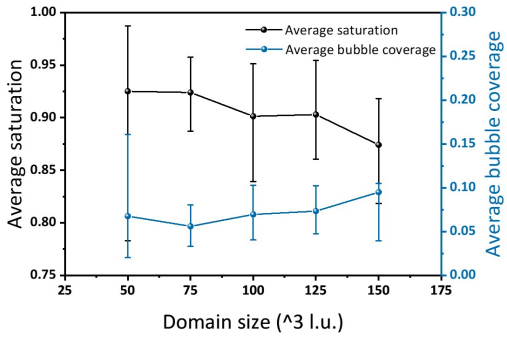

Figure 3.4.: Average saturation varies with domain size.

Sample uncertainty

To provide a baseline sense of sampling reliability without an exhaustive ensemble, we simulate five non-overlapping interior subvolumes for each compression ratio (CR = 25%, 50%, 75%). Each subvolume is $100 \times 100 \times 100$ lattice units and uses the same boundary and source settings as in the main text. Statistics are sampled only in the interior porous region. We report the ensemble mean and standard deviation across the five subvolumes for average electrolyte saturation and bubble coverage in Table 3.1. It could be found that all standard deviations are below 5%. The curves in Figure 3.5 shows the average of the five cases and the error bars span the minimum–maximum range across the five cases, which is not the standard deviation. The trends are consistent with that in the main text. As compression ratio increases, the average saturation decreases while the average bubble coverage increases, and the error bars widen with compression, indicating larger size of trapped bubbles at higher CR.

Table 3.1.: Ensemble statistics across five interior subvolumes per compression ratio.

Variable	Condition	Mean	Standard deviation
Electrolyte saturation	CR = 25%	0.9000	0.0204
	CR = 50%	0.8652	0.0240
	CR = 75%	0.7852	0.0339
Bubble coverage	CR = 25%	0.0757	0.0060
	CR = 50%	0.1001	0.0249
	CR = 75%	0.1587	0.0430

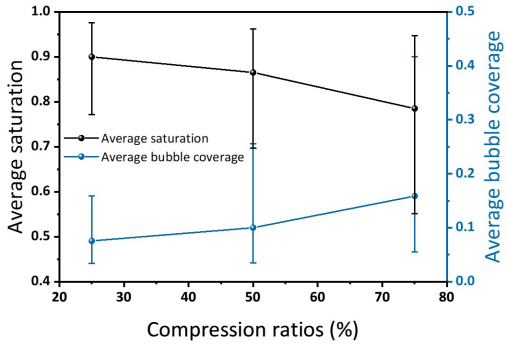

Figure 3.5.: Ensemble average electrolyte saturation and bubble coverage for different compression ratios.

3.3.2. Model set-up

To simulate the bubble evolution over a longer time, The author uses a simulation domain of $100 \times 100 \times 100$ lattice sites (as shown in Figure 3.6). The electrochemical reaction is introduced through reactive boundary conditions (Eq. (3.36)) at lattice nodes adjacent to the reactive boundary, converting all 19 fluid populations of one fluid species into another one governed by the reaction rate k_r [107],

$$\frac{\partial \rho^r}{\partial t} = -k_r\, \rho^r, \quad \frac{\partial \rho^b}{\partial t} = k_r\, \rho^b, \tag{3.36}$$

In this study, k_r is treated as a nominal conversion rate prescribed to generate bubbles at the reactive boundary. It controls the bubble generation rate but is not linked to a predictive electrochemical current. Consequently, this study focuses on the investigation of kinematic bubble visualization and is limited to a qualitative pattern. To provides a dimensional anchor only for the nominal boundary conversion rate k_r used in Eq. 3.36, Representative electrochemical currents are mapped to an order-of-magnitude source so that trends in the discussion section can

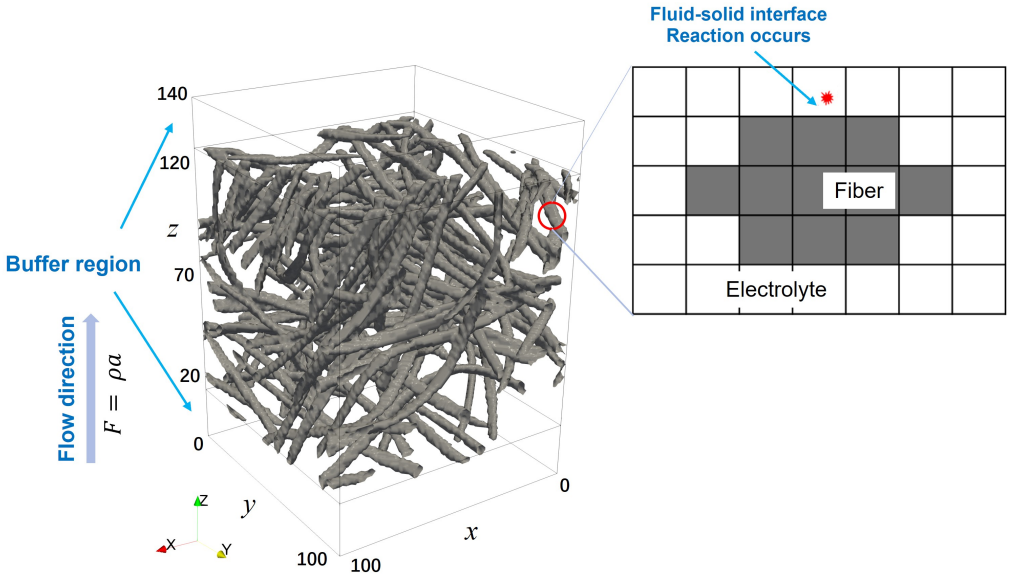

Figure 3.6.: Schematic diagram of the simulation geometry.

be expressed via non-dimensional controls. It is not intended for predictive HER kinetics. For the HER, a cathodic kinetic expression gives the local current density

$$j_{H_2/H^+} = a_v j_0^{H_2/H^+} \exp\left(\frac{-2(1-\beta)F\,\eta_{H_2/H^+}}{RT}\right) \tag{3.37}$$

where a_v is the geometric specific surface area, j_0 is the exchange current density (e.g. 6.6×10^{-5} to $2.7 \times 10^{-1}\,\mathrm{mA\,cm^{-2}}$ as reported by Schweiss et al. [108]), β is the transfer coefficient, F is Faraday's constant, R is the general gas constant, T is temperature, and η_{H_2/H^+} is the overpotential. In present work, we assume a hydrogen-ion concentration of 4 M and an applied potential of $-0.26\,\mathrm{V}$. The nominal reaction rate k_r is then estimated as

$$k_r = \frac{j_{H_2/H^+} M_{H_2}}{2F\rho_{H_2}} C_t \tag{3.38}$$

where M_{H_2} is the molar mass, rho_{H_2} is hydrogen density and C_t is LBM time scale conversion factor. This back-of-the-envelope estimate indicates that k_r in lattice units is very small (typically 10^{-11}–10^{-7}), which would make bubble generation too slow to observe within feasible runtimes

under our equal-density, incompressible setting. To accelerate bubble generation for qualitative visualization, we apply a factor based on the liquid-to-gas density ratio (order 10^5). It is thus reasonable to explore k_r in the range 10^{-6} to 10^{-2} (l.u.) in the main text, while interpreting results through non-dimensional trends rather than quantitative kinetics.

To model the porous medium, the carbon fiber geometry is incorporated into the LBM domain, and a bounce-back boundary condition is applied at all solid–fluid interfaces to enforce a no-slip condition on the carbon fibers [109]. The contact angle is prescribed as 60°, consistent with the hydrophilic behaviour of VRFB carbon felts in sulphuric electrolyte [110, 111], and is chosen to ensure sufficient wettability and numerical robustness with the current fictitious-density wetting scheme [112]. Because this scheme is reliable only over a moderate range of contact angles [113], we do not investigate wettability dependence here, and our conclusions are limited to the hydrophilic regime. The four faces parallel to the flow direction are set as periodic boundaries to emulate an interior representative sub-volume of the felt and to avoid unknown wall-wettability effects and artificial wall pinning. The inlet and outlet use the recoloring boundary to remove bubbles, as expressed in Eqs. (3.39) and (3.40). This boundary is numerically robust for two-phase color-gradient LBM, reducing spurious interface reflections compared with standard open boundaries. The recoloring coefficients are determined based on the initial component densities $\rho_0^r = 1$ and $\rho_0^b = 1 \times 10^{-10}$.

$$f_i^r\left(x_{\text{boundary}}, t\right) = \frac{\rho_0^r}{\rho_0^r + \rho_0^b} f_i\left(x_{\text{boundary}}, t\right), \tag{3.39}$$

$$f_i^b\left(x_{\text{boundary}}, t\right) = \frac{\rho_0^b}{\rho_0^r + \rho_0^b} f_i\left(x_{\text{boundary}}, t\right). \tag{3.40}$$

where x_{boundary} represents a list of the lattice sites that belong to the inlet and outlet boundary. To eliminate the influence of complex geometry on the inlet and outlet boundary condition settings, The author inserts a buffer region with a thickness of 20 lattice sites at both ends [109].

3.3.3. Unit conversion

To connect the parameters in the LBM simulation with real physical quantities, the lattice units must first be defined in terms of basic SI units, including the length scale C_l, the time scale C_t, and the mass scale C_m. These scales are chosen appropriately based on the physical properties such as surface tension, viscosity, and the resolution of the lattice,

$$C_t = \frac{C_l^2\, \nu_{r,LB}}{\nu_{r,Phys}}, \tag{3.41}$$

$$C_m = \frac{\rho_{Phys}\, C_l^3}{\rho_{LB}}. \tag{3.42}$$

Here C_l is determined by the lattice resolution, ν_b is the kinematic viscosity of the blue fluid, and σ is the surface tension. The subscripts Phys and LB represent physical and lattice Boltzmann units, respectively. Once these base units are defined, all other parameters in the LBM simulation can be computed using the corresponding dimensionless relations,

$$\sigma_{Phys} = \frac{\sigma_{LB}\, C_m}{C_t^2}, \tag{3.43}$$

$$P_{Phys} = \frac{P_{\mathrm{LB}}\, C_m}{C_l\, C_t^2}. \tag{3.44}$$

We assess the relative importance of body forces and interfacial tension using the Bond number (buoyancy-to-capillary) and the Capillary number (viscous-to-capillary). Taking the average pore size as the characteristic length, $L \approx 60$–$80\ \mu$m for CR $= 25\%$–75% in present study, we obtain $\mathrm{Bo} = \dfrac{\Delta\rho\, g\, L^2}{\sigma}$ lies in the range of 10^{-5} to 10^{-3} and the capillary number $\mathrm{Ca} = \dfrac{\rho\, \nu\, u}{\sigma}$ is much smaller than 10^{-6}. These ranges indicate a capillary-dominated regime in which buoyancy is negligible for pore-scale detachment, rise, and trapping. Consequently, we adopt an equal-density setting in the model ($\rho^r_{phys} = \rho^b_{phys} = 1.325 \times 10^3\,\mathrm{kg\,m^{-3}}$) as a kinematic simplification within this applicability domain. Previous work has applied and validated the color–gradient LBM for capillarity-driven phenomena, including droplet coalescence [105], evaporation [114], and bubble growth and departure [107]. Furthermore, color-gradient LBM method have been used by different groups [104, 115, 116] for bubble transport in porous media, which demonstrate its general applicability for mesoscale-macroscale phenomena. Then

Physicochemical parameters	Physical values	Lattice values
Characteristic length, L_0	2.44×10^{-6} m	1 l.u.
Surface tension, σ	7.2×10^{-2} N m^{-1} [117]	0.069 l.u.
Kinematic viscosity of H_2, ν_b	1×10^{-5} m^{2}s^{-1}	0.228 l.u.
Kinematic viscosity of electrolyte, ν_r	4.38×10^{-6} m^{2}s^{-1} [54]	0.1 l.u.
Electrolyte density, ρ^r	1.325×10^3 Kg m^{-3} [54]	1 l.u.
Pressure, P	4.27×10^5 Pa	1 l.u.
Characteristic time, t	1.36×10^{-2} s	1×10^5 l.u.

Table 3.2.: Parameters used in the present study.

the pressure drop could be evaluated by the liquid density:

$$\Delta P = \rho^r a L, \tag{3.45}$$

where a is the acceleration, which is applied uniformly on both fluids at all fluid nodes, and L is the distance between the inlet and outlet boundaries. For the sake of clarity, all simulation parameters discussed are presented in lattice unit.

4. Investigating Bubble Formation and Evolution in Vanadium Redox Flow Batteries via Synchrotron X-Ray Imaging

4.1. Introduction

As discussed in Section 1.4, previous research on the HER in VRFBs has primarily focused on the electrochemical mechanisms at the electrode–electrolyte interface and strategies to suppress the HER. These efforts have included electrode surface modification, electrolyte additives, and operational parameter optimization. While such methods have improved macroscopic performance, they provide limited insight into the microscale phenomena associated with bubble formation and transport.

Among the various investigations related to bubbles within VRFB electrodes, no research study has yet investigated the individual bubble morphologies. Since the presence of bubbles directly impacts the electrolyte's transport pathway, it is just as essential to study their size and shape as it is to investigate the structure and morphology of the electrode pores.

In other research areas focusing on pore-scale morphology, a wealth of existing studies provides valuable insights and ideas for present work. Hoehl et al. [118] conducted *operando* experiments using synchrotron X-ray radiography to investigate proton exchange membrane (PEM) water electrolysis cells. They focused on analyzing the frequency and volume of gas

bubbles released from the porous transport layer (PTL) into the flow channels. The study revealed that a water-saturated PTL exhibited selective transport pathways for the evolved gas, with more pathways occurring at higher current densities. Panchenko et al. [119] employed in-plane synchrotron radiography to investigate transport phenomena in a PEM electrolysis cell. Their study successfully visualized individual bubbles occupying the pores and propagating through the PTL, along with the gas flow from the cathode catalyst layer to the flow channels. Jo et al. [120] employed image processing techniques to investigate the bubble mechanisms within a 2D-packed bed at the pore level. Through extensive analysis of a substantial collection of images, they identified two bubble coalescence mechanisms and three breakup mechanisms. Furthermore, they derived valuable data on numerous two-phase parameters, including local void fraction, bubble velocity, size, number, and shape. These studies on bubble dynamics are highly intriguing because they provide critical insights into characterizing and analyzing bubbles. Investigating bubble morphology at various stages offers a valuable understanding of bubble formation and growth mechanisms within the electrode.

In this chapter, the author presents results obtained by employing high-resolution synchrotron X-ray tomography in combination with deep learning-based image segmentation to systematically analyze gas bubble growth, coalescence, and spatial redistribution within VRFB electrodes [58, 118]. The author has characterized the distribution, size, and morphology of the formed hydrogen bubbles and elaborated on the impact of the working electrode potential on bubble formation and evolution. Unlike traditional strategies that focus on suppressing HER through material or operational optimization, the present work shifts the focus to the bubbles themselves. By enabling a quantitative, three-dimensional characterization of individual bubble morphology inside VRFB electrodes, previously inaccessible with conventional techniques, this study provides new insight into how electrode potential controls bubble evolution and transport within porous carbon felts. This approach lays the groundwork for future studies by establishing quantitative correlations between bubble morphology, electrode microstructure, mass transport, and electrochemical performance. Ultimately, the data presented here will offer new insights for optimizing battery design and mitigating the negative impact of HER.

4.2. Detailed Bubble Analysis

This section focuses on one experiment for a detailed bubble analysis, which includes the bubble size distribution and characteristic shape descriptions such as bubble roundness, flatness, and elongation. During the experiment, a working electrode potential of $-200\,\mathrm{mV}$ was applied when the electrolyte flow was stopped. Thus, the bubble growth and movement processes were only affected by surface tension and buoyancy.

At the electrode–electrolyte interface, HER produces gas molecules that initially form nanobubble nuclei via homogeneous or heterogeneous nucleation. According to classical nucleation theory, gas bubble nuclei form when local hydrogen supersaturation reduces the nucleation free-energy barrier, set by surface tension and Laplace pressure, such that stable critical nuclei can be created. As the HER proceeds, these nanobubbles grow by absorbing additional hydrogen molecules—a process governed by diffusion-limited growth—and are simultaneously subject to buoyancy forces that promote their detachment and upward migration [121]. However, in a static system, the absence of convective mixing means that coalescence becomes the dominant growth mechanism [122]. When adjacent bubbles come into contact, capillary forces drive their merging, and the resulting bubble shape is influenced by both the viscous resistance of the electrolyte and the anisotropic microstructure of electrode fibers.

Figure 4.1 presents how the bubble size evolves from the initial electrolyte filling after the applied negative potential has set-off the HER. In this study, the size intervals in all histograms are set as 10 pixels. As shown in Figure 4.1(a), most bubbles in the initial distribution have an equivalent diameter of 10–20 pixels, corresponding to a 90–180 µm size. A few bubbles with equivalent diameters smaller than 10 pixels were observed, where as the number of bubbles gradually decreased with sizes larger than 20 pixels. The largest bubble size was 66 pixels in equivalent diameter, corresponding to around 600 µm. This observation is consistent with diffusion-limited growth theory, where bubbles rapidly absorb additional gas and coalesce, leading to a marked shift in the bubble size distribution. After the HER, the number of bubbles with an equivalent diameter below 10 pixels (90 µm) decreases, while the number of bubbles with an equivalent diameter greater than 10 pixels increases significantly. Most bubbles are still observed in the equivalent diameter range of 10–20 pixels, but the largest bubble has an

equivalent diameter of 82 pixels, corresponding to around 740 µm.

Figure 4.1(b) displays the cumulative bubble volume as a function of increasing equivalent diameter, with each data point representing one bubble in the overall volume. It can be concluded that the overall cumulative bubble volume increases quite distinctly from 1.48×10^6 voxels before the HER to 5.08×10^6 voxels afterward. Furthermore, in both cases, there is a sharp increase in the cumulative bubble volume for bubbles in the equivalent diameter range of 20–50 pixels (180–450 µm). From a theoretical standpoint, this sharp increase indicates a transition point where diffusion-limited growth and bubble coalescence accelerate, leading to a significant volume contribution from bubbles within this size range [122].

The pie charts in Figure 4.1(c) illustrate that bubbles with diameters under 20 pixels are negligible in terms of volume, likely because they represent early-stage nuclei that either grow or merge, whereas bubbles in the 20-50 pixel range dominate the cumulative volume.

A comparison with Figure 4.2(a) reveals that at $-300\,\mathrm{mV}$ the HER is significantly more intense, producing more large-sized bubbles. At this higher potential, the nucleation rate is so high that small, independent bubbles quickly grow and merge, resulting in fewer overall bubbles but a greater prevalence of super-sized bubbles. Such behavior aligns with theoretical predictions: as the applied potential becomes more negative, the rate of hydrogen production increases exponentially (per the Tafel equation), and bubble growth becomes more pronounced due to the rapid accumulation of gas molecules.

Figure 4.2 displays the bubble size distribution analysis at $-300\,\mathrm{mV}$ performed analogously to the data presented in Figure 4.1. A comparison of Figure 4.2(a) with Figure 4.1(a) shows that the HER at $-300\,\mathrm{mV}$ is significantly more intense and generates more large-sized bubbles. The number of bubbles whose equivalent diameter is below 40 pixels (360 µm) is significantly reduced after the HER period, while the number of larger bubbles remains quite similar up to a size of 80 pixels (720 µm). However, several super-sized bubbles appear with the maximum equivalent diameter reaching 240 pixels (2160 µm). At a higher potential, the nucleation rate is so high that small, independent bubbles quickly grow and merge, resulting in fewer overall bubbles but a greater prevalence of super-sized bubbles. Such behavior aligns with theoretical predictions: as the applied potential becomes more negative, the rate of hydrogen production increases exponentially (per the Tafel equation), and bubble growth becomes more pronounced

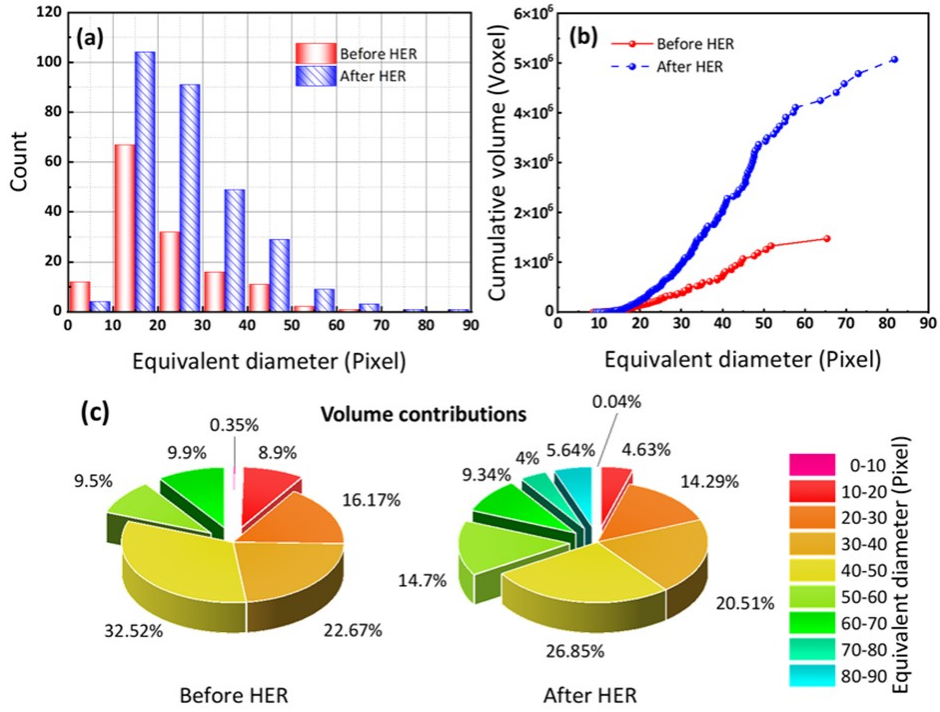

Figure 4.1.: Comparison of the bubble sizes and their contribution to the cumulative bubble volume before and after the HER period at $-200\,\mathrm{mV}$: (a) size histograms, (b) cumulative bubble volumes as a function of equivalent diameter, and (c) volume contributions of different bubble size intervals.

due to the rapid accumulation of gas molecules.

Due to the more negative potential of the working electrode at $-300\,\mathrm{mV}$, the HER becomes more vigorous. In this case, it is difficult for new independent small bubbles to persist since they grow and coalesce rapidly. This leads to a significant reduction in the total number of bubbles and the formation of several major super-sized bubbles. These observations are clearly reflected in the cumulative bubble volume curve in Figure 4.2(b). In the region of small bubbles, the cumulative volume after HER is even lower than before HER. Furthermore, the majority of the volume is contributed by these large, super-sized bubbles. Figure 4.2(c) shows the relative volume contributions of different bubble sizes. After HER, the two largest bubbles alone account for over 75% of the total bubble volume. Such large bubbles are undesirable as they hinder electrolyte transport and reduce the accessible active area, thereby impairing battery

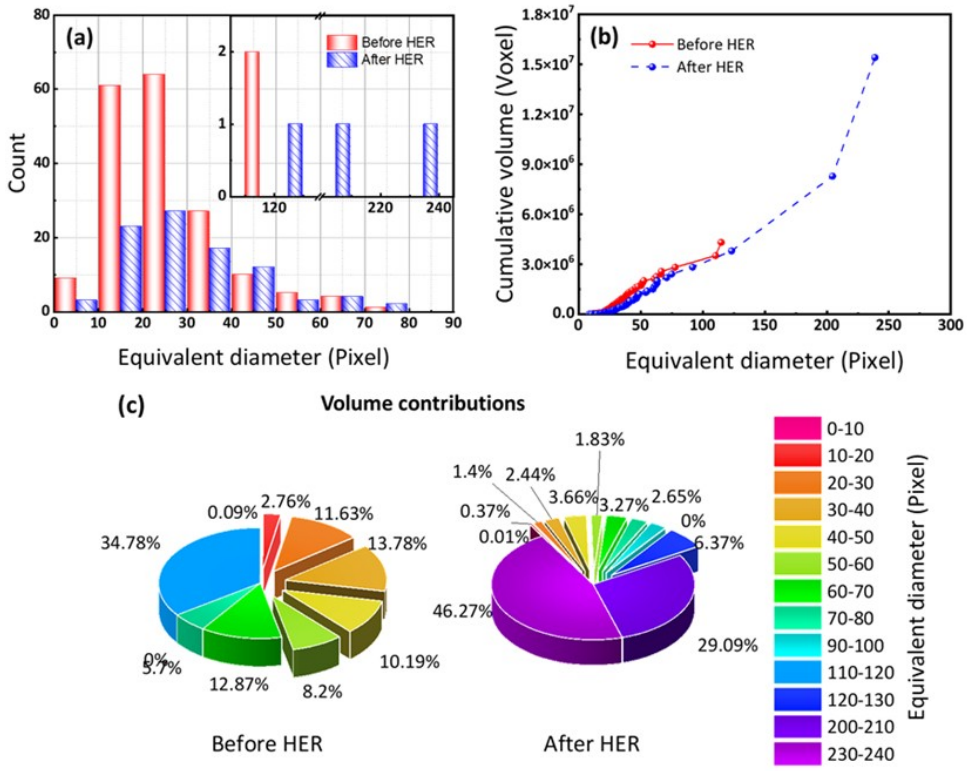

Figure 4.2.: Comparison of the bubble sizes and their contribution to the cumulative bubble volume before and after the HER period at $-300\,\mathrm{mV}$: (a) size histograms; (b) cumulative bubble volume as a function of equivalent diameter; (c) volume contributions of different bubble sizes.

performance.

As previously reported, bubbles in VRFB electrodes are unavoidable in the operated potential range if the state of charge is not strongly limited [71]. Due to the electrode microstructure, some bubbles are entirely trapped in the electrode, blocking the pores for electrolyte transport. Studying their shape and distribution in the VRFB electrodes is meaningful to optimizing the electrolyte transport process. Thus, this study characterizes the bubbles' characteristic parameters in detail using the bubble statistical analysis tool library.

4.3. Bubble Shape Evolution and Spatial Distribution

The evolution in bubble shape can be understood through the interplay of surface tension, buoyancy, and viscous forces within the electrode's heterogeneous microstructure. Figure 4.3 displays how the bubble shapes change from the initial bubble distribution to after the HER period. For the roundness distribution histogram, the interval is set to 0.1, while the elongation and flatness distribution histograms have intervals of 0.5. The selection of interval sizes is based on their respective value ranges.

Before HER, most residual bubbles are nearly spherical (with an average roundness of approximately 0.83) due to the dominance of surface tension, which tends to minimize the surface area. However, once HER is initiated, rapid bubble growth and frequent coalescence introduce distortions; the bubbles deviate from spherical shapes due to limited relaxation time and additional constraints from the surrounding porous structure. After HER, the average roundness in the electrode decreased by 13%, and average elongation and flatness increased by 8% and 11%, respectively, as shown in Figure 4.3(a). This change in shape is theoretically expected when bubbles coalesce in confined or anisotropic media, where spatial constraints force bubbles into irregular configurations.

The observation that the average flatness is slightly higher than the average elongation in both cases may be attributed to the intrinsic anisotropy of the electrode material, which is further enhanced by compression, thereby promoting preferential deformation along certain axes [123]. Notably, in Figure 4.3(b), the roundness frequency distribution is increased within the 0.6–0.7 interval, which is close to the average roundness. The frequency distributions for both elongation and flatness (Figures 4.3(c) and (d)) shift towards higher values after HER. However, some highly elongated bubbles can be observed in the elongation distribution both before and after HER. Such bubbles often appear in the edge areas of the electrodes, where the electrode is in contact with other components, such as the flow field, gasket, or frame.

To relate these observed shape characteristics to specific bubbles and their position within the electrode volume, Figure 4.4 displays the 3D visualized bubbles color-rendered according to their shape characteristics, further linking the observed morphology to the underlying electrode structure. Figure 4.4(a) highlights the roundness distribution, whereas Figure 4.4(b) shows

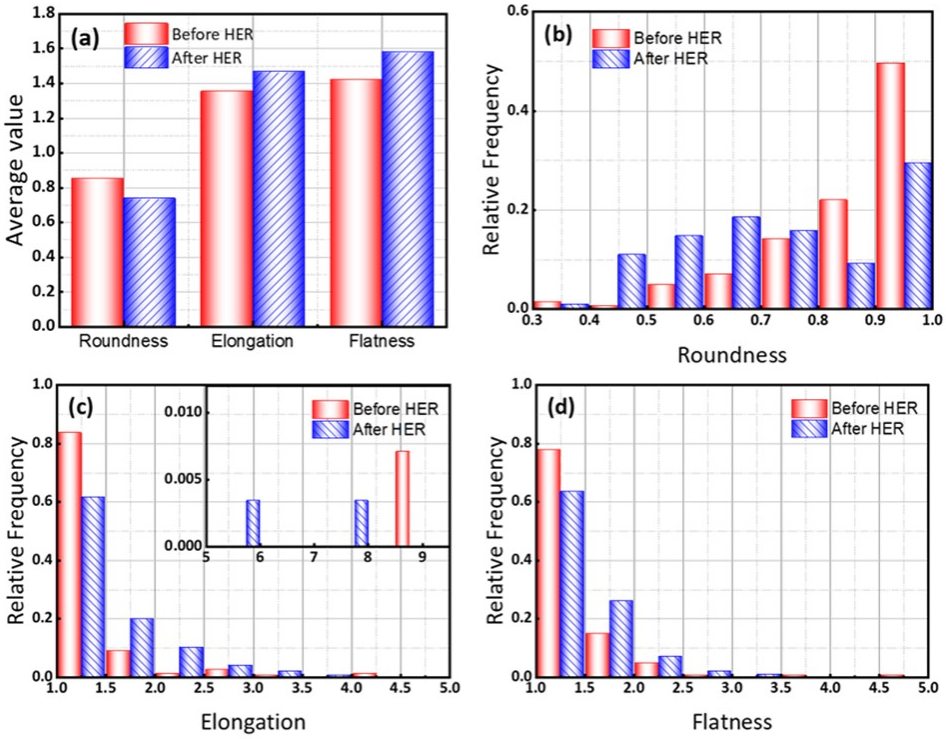

Figure 4.3.: Statistical analysis of bubble shape parameters before and after HER at $-200\,\mathrm{mV}$: (a) average values of roundness, elongation, and flatness; (b) roundness histogram; (c) elongation histogram; (d) flatness histogram.

elongation, and Figure 4.4(c) displays flatness values.

Before the HER, the electrolyte refill removed most bubbles near the edges, while bubbles remained in the electrode center. This may be caused by the inhomogeneous porosity distribution of the electrode due to uneven assembly stress, as indicated by membrane deformation (Figure A.1).

Figure 4.5 shows the bubble shape analysis, analogous to Figure 4.3. The bubble shape becomes more irregular after HER. At $-300\,\mathrm{mV}$, the average roundness decreases by 21%, while elongation and flatness increase by 11% and 16%, respectively. Compared to $-200\,\mathrm{mV}$, roundness is lower and the other two metrics are slightly higher. In Figure 4.5(b), a sub-peak appears in the roundness frequency within the 0.5–0.6 interval, shifted slightly lower compared to the $-200\,\mathrm{mV}$ case. The exponential decline in elongation and flatness distributions remains

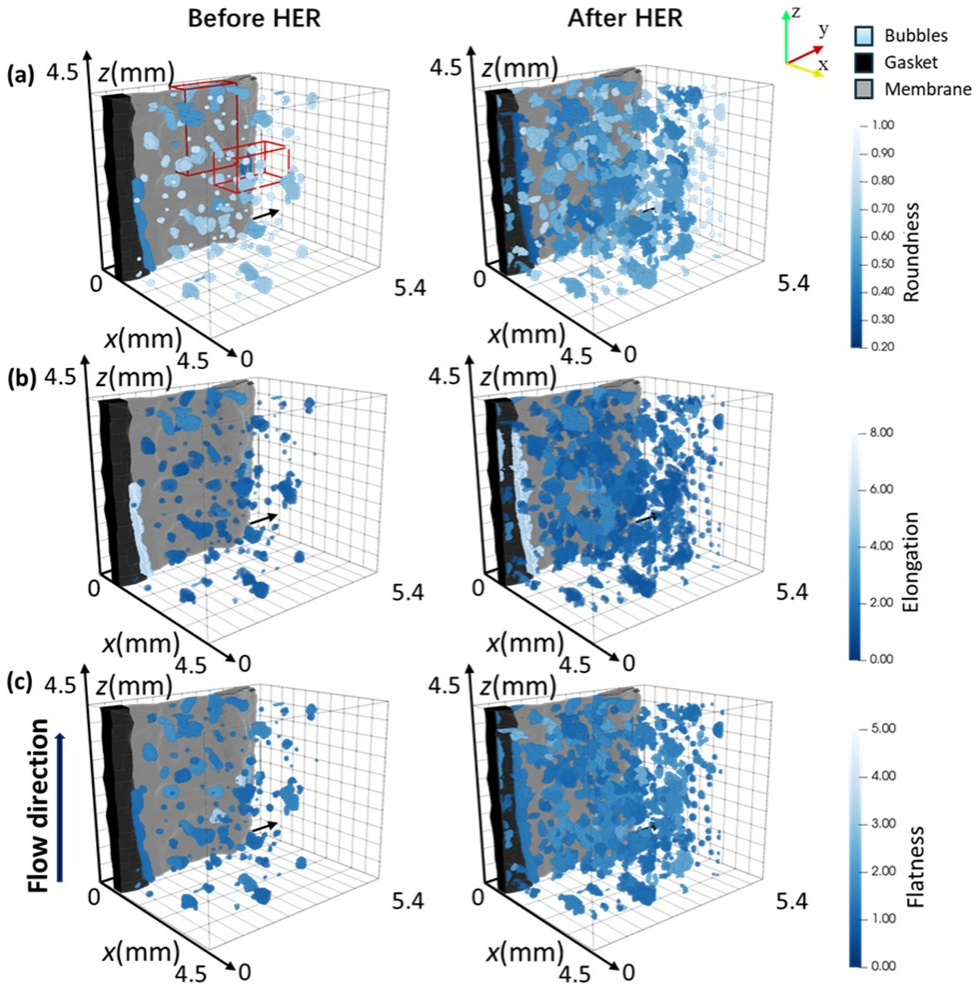

Figure 4.4.: 3D visualization of bubble shape distributions before and after HER at $-200\,\mathrm{mV}$: (a) color-coded roundness; (b) elongation; (c) flatness.

consistent.

Figure 4.6 shows 3D visualization of shape characteristics similar to Figure 4.4. During HER at $-300\,\mathrm{mV}$, gas generation is more concentrated at the electrode edges. Unlike the discrete, regular bubbles seen at $-200\,\mathrm{mV}$, bubbles at more negative potentials tend to accumulate and fuse at the edges, forming continuous gas paths along the frame.

Compared to the measurement at $-300\,\mathrm{mV}$ (Figure S3), significantly fewer residual bubbles were left in the electrode, especially in the center region.

Figure 4.7 compares the local bubble distribution in the red-marked region of Figure 4.4(a)

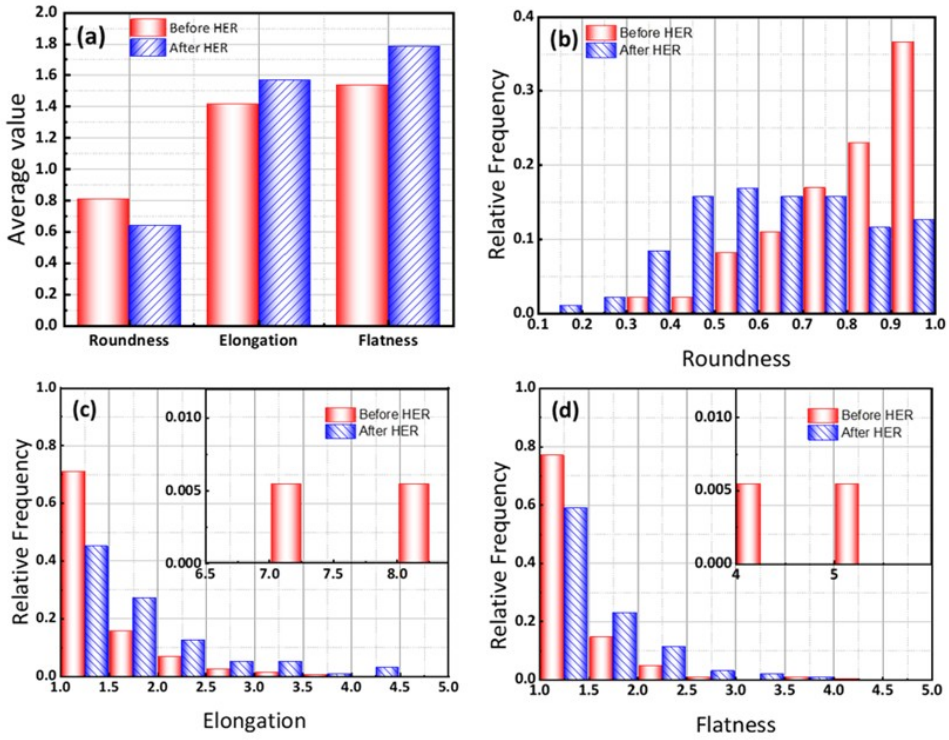

Figure 4.5.: Comparison of bubble shape statistics before and after HER at $-300\,\mathrm{mV}$: (a) average shape characteristics; (b) roundness histogram; (c) elongation histogram; (d) flatness histogram.

with that at $-300\,\mathrm{mV}$ before HER. Residual bubbles in both cases appear in similar positions, and many bubbles of comparable shape can be found at matching locations. This implies that the electrode microstructure plays a critical role in trapping bubbles. These fixed positions are likely unfavorable to bubble removal, contributing to long-term accumulation.

Spherical bubbles with high roundness are primarily located in the electrode center, while highly elongated and flat bubbles are more common at the edges. Furthermore, rounder bubbles are generally smaller, suggesting that shape irregularity arises from the combined effects of growth and spatial confinement within the heterogeneous fiber structure, where larger bubbles are more strongly deformed due to confinement. A notable trend emerges upon completion of the HER period: many high-roundness bubbles appear at the electrode edges, while central bubbles grow larger and more deformed. This is likely because edge areas, initially devoid of bubbles, permit the nucleation of new independent bubbles, while central areas dominated by

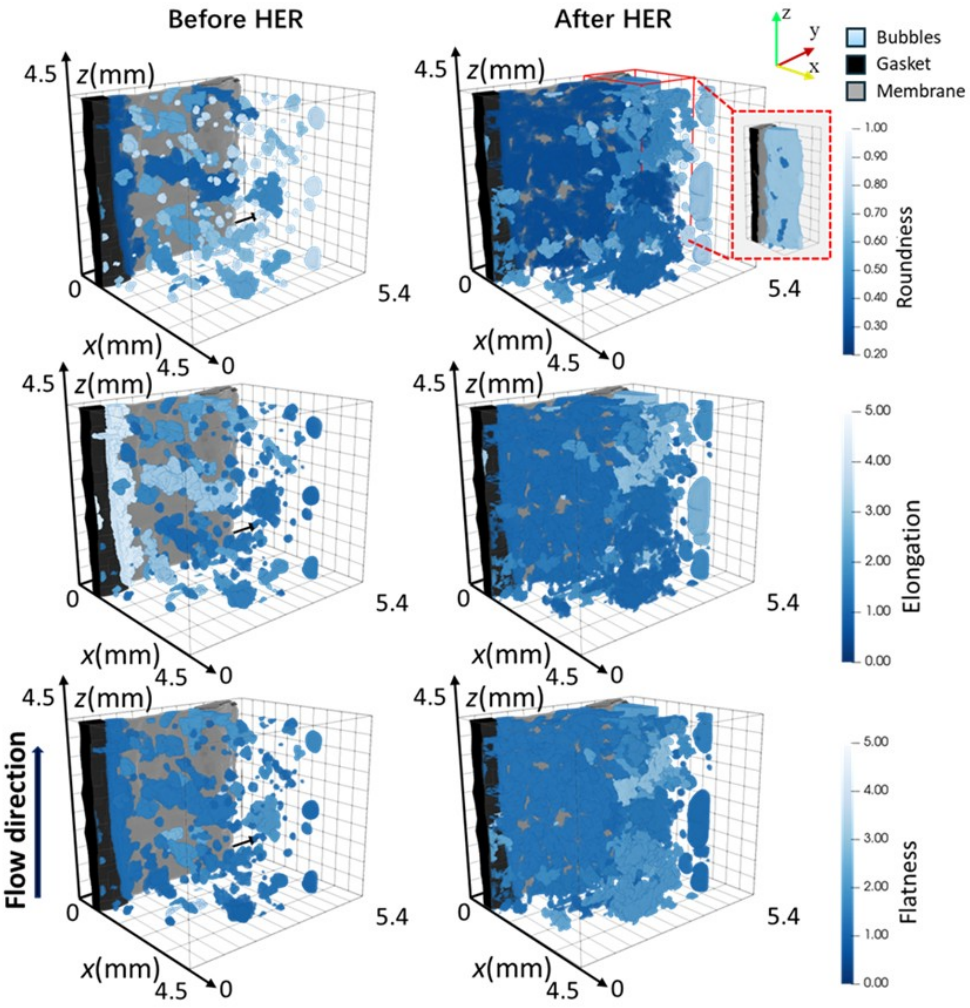

Figure 4.6.: 3D visualization of bubble shape distributions for −300 mV before and after HER: (a) roundness; (b) elongation; (c) flatness.

residual bubbles promote further growth and coalescence. Therefore, forming new spherical bubbles in the center becomes increasingly difficult, resulting in lower roundness in that region. Overall, the experimental observations are consistent with established theories of nucleation, diffusion-limited growth, and bubble coalescence. These theoretical considerations not only help explain the statistical distributions of bubble size and shape observed in our experiments but also underscore the critical role of the electrode microstructure in governing bubble dynamics and, ultimately, electrolyte transport.

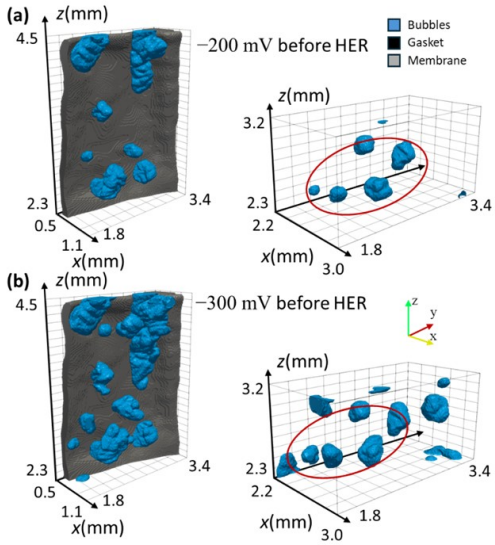

Figure 4.7.: Comparison of residual bubble distributions in the marked region of Figure 4.4(a): (a) at $-200\,\mathrm{mV}$; (b) at $-300\,\mathrm{mV}$ before HER.

4.4. Effect of Applied Electrode Potential

Figure 4.8 presents the bubble size distribution in the working electrode before and after the HER triggered by applying various electrode potentials between $-175\,\mathrm{mV}$ and $-300\,\mathrm{mV}$. As shown in a recent study, at moderately negative working electrode potentials, hydrogen evolution remains weak, resulting in a low and nearly time-invariant bubble population, whereas pronounced HER activity and rapid bubble growth are only observed at more negative potentials [68]. The bubble size distribution shows a similar trend at each working electrode potential. In all instances, the interval with the highest bubble count consistently falls within an equivalent diameter range of 10–30 pixels (90–270 µm), whether before or after the HER.

When the applied potential is $-175\,\mathrm{mV}$, the overall bubble count is significantly lower than in the other experiments, which can be related to the lower HER activity at this potential. At $-200\,\mathrm{mV}$ (Figure 4.8(b)), the most independent bubbles are detected after the HER, which implies that a significant amount of new tiny bubbles evolved at this potential. As the applied potential becomes more negative, the number of bubbles after the HER period gradually decreases, while more bubbles with larger sizes appear. For example, the largest bubble before the HER at $-250\,\mathrm{mV}$ has an equivalent diameter of 123 pixels (around 1100 µm), whereas after HER, a

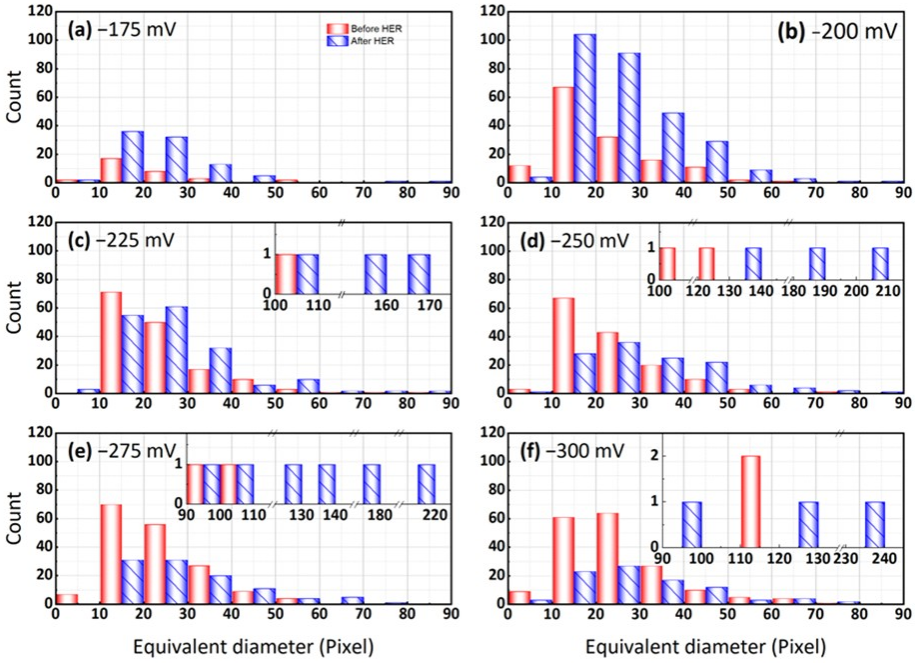

Figure 4.8.: Histograms of the bubble size distributions before and after the HER period at various working electrode potentials from (a) $-175\,\mathrm{mV}$ to (f) $-300\,\mathrm{mV}$.

bubble with a diameter of 201 pixels (around 1800 µm) was detected. Moreover, fewer bubbles with sizes below 30 pixels (270 µm) are observed after HER, indicating that these bubbles must have grown or coalesced into larger ones.

Similar observations were made at more negative potentials of $-275\,\mathrm{mV}$ and $-300\,\mathrm{mV}$, where fewer small bubbles were detected and larger ones dominated. Thus, these bubble size distributions provide insights into the amount of independently generated bubbles and the extent of bubble growth and coalescence under different electrode potentials.

A previous publication from our group has shown that the bubble volume fraction within the electrode increases when more negative potentials are applied [68]. This observation supports the understanding that HER activity intensifies at more negative electrode potentials.

Figure 4.9 presents two metrics to evaluate the influence of potential on bubble size. Figure 4.9(a) classifies bubbles into two size categories, using an equivalent diameter threshold of 90 pixels (270 µm), based on the maximum bubble size after HER at $-175\,\mathrm{mV}$. It shows

the HER-induced volume change for both small and large bubbles, calculated as the volume difference before and after HER. In all cases, residual bubbles before HER fall within the small bubble category. When the potential exceeds $-200\,\mathrm{mV}$, large bubbles emerge and dominate the volume increase. At $-300\,\mathrm{mV}$, the volume of small bubbles even decreases, indicating that newly formed small bubbles are absorbed into larger ones.

Figure 4.9(b) shows the cumulative bubble volume after HER as a function of equivalent diameter. The data for $-175\,\mathrm{mV}$ and $-200\,\mathrm{mV}$ are clearly distinguishable from those at more negative potentials. At $-175\,\mathrm{mV}$, bubble formation is minimal and dominated by small bubbles. At $-200\,\mathrm{mV}$, bubble generation is more active, with a sharp increase in cumulative volume up to a bubble size of 82 pixels (around 740 µm). Beyond this point, no larger bubbles appear. In contrast, at more negative potentials, the slope of the cumulative volume curve flattens at small sizes and steepens at larger sizes, reflecting coalescence and growth of residual bubbles. These large bubbles often form near the electrode corners, possibly by merging with center-located bubbles (Figure 4.6).

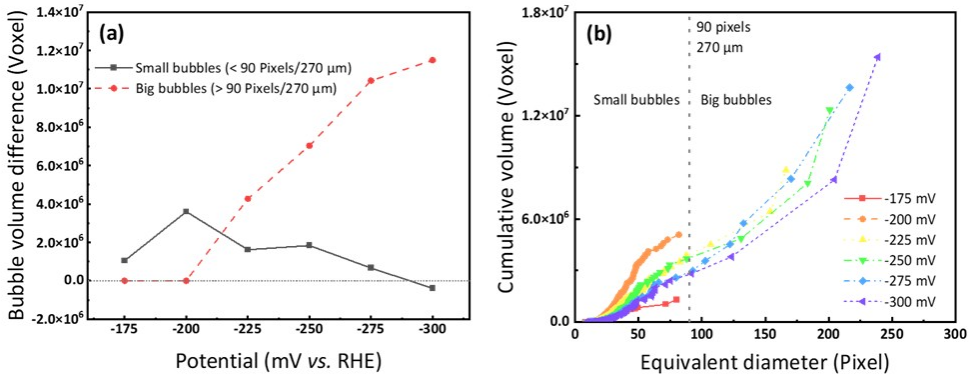

Figure 4.9.: Potential-dependent bubble volume changes: (a) HER-induced volume changes in small and big bubble classes (threshold: 90 pixels / 270 µm); (b) cumulative bubble volume after HER as a function of equivalent diameter.

In addition to bubble size and volume, we also investigated the effect of electrode potential on bubble shape. Figure 4.10(a–c) show the average values of roundness, elongation, and flatness at different electrode potentials, both before and after HER. Before HER (red line), shape parameters are similar across all conditions: roundness ≈ 0.83, elongation ≈ 1.39, and flatness ≈ 1.48. After HER, bubbles became more irregular, with decreasing roundness and

increasing elongation and flatness, especially at more negative potentials. This trend reflects enhanced HER activity leading to anisotropic bubble growth and coalescence.

Interestingly, the $-250\,\mathrm{mV}$ case slightly deviates from the trend, showing bubbles that are less round, more elongated and flatter than expected. This might be due to the onset of the vanadium(III)/vanadium(II) redox reaction, which has a standard equilibrium potential around $-255\,\mathrm{mV}$ vs. SHE [124]. As vanadium(IV) is reduced to V(III), and further to V(II), this competing reaction may reduce the rate of HER and thus alter bubble formation dynamics.

Figure 4.10(d) supports this interpretation: the coulombic efficiency curve exhibits a turning point at $-250\,\mathrm{mV}$, indicating that part of the charge is consumed by the V(III)/V(II) redox couple rather than HER, leading to fewer bubbles and less gas evolution. While we cannot yet conclude whether this behavior is statistically significant or an experimental outlier due to limited data, these findings suggest that the V(III)/V(II) reaction competes with HER and modifies gas evolution behavior and bubble morphology.

4.5. Relationship Between Bubble Shape and Size

This final section combines the previous analyses by showing the relationship between the bubbles' size and shape. Due to the limited number of bubbles within a single experiment, we pooled all bubble data from all applied potentials before and after triggering the HER to finalize the study. To reduce the disturbance of statistical trends by extreme cases, the smallest two and the largest two bubbles were excluded from the analysis.

Figure 4.11 shows the statistical relationship between the bubble size and the characteristic shape parameters. In general, the shape of a bubble becomes gradually more irregular as its volume increases, i.e., its roundness decreases, and elongation and flatness become larger at higher bubble volumes. The shape changes are more pronounced at smaller bubble sizes and diminish when the bubble size reaches a certain value (equivalent diameter of around 320 µm in this experiment). The elongation and flatness remain nearly constant at larger sizes, with values of approximately 1.8 and 1.6, respectively. This indicates that smaller bubbles, typically generated under low HER activity, tend to be rounder. In contrast, bubble growth and coalescence in the disordered fiber structure lead to more irregular shapes in larger bubbles.

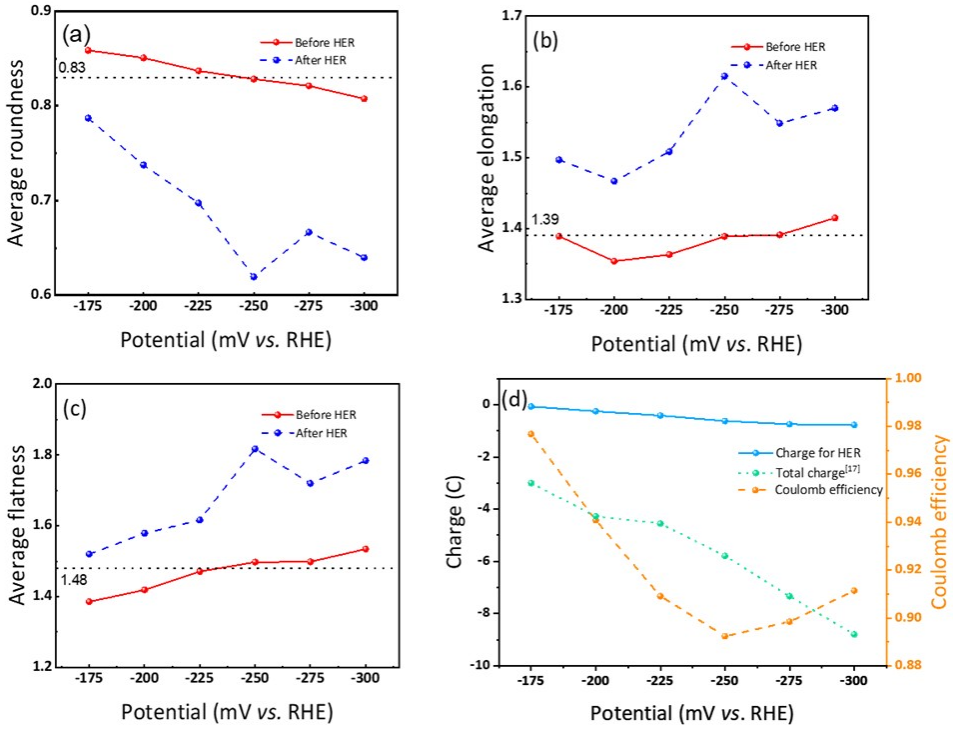

Figure 4.10.: Potential-dependent metrics: (a) average roundness, (b) average elongation, (c) average flatness, and (d) total integrated charge, HER-related charge, and coulombic efficiency in the negative half-cell.

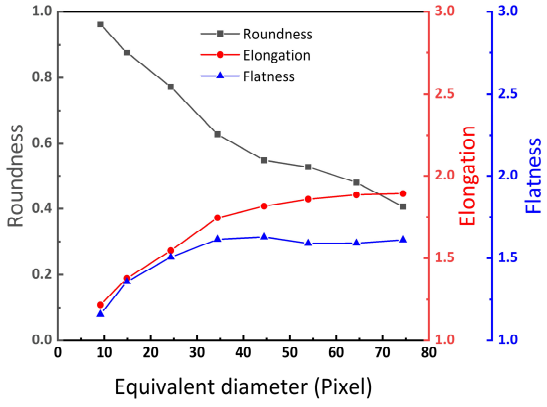

Figure 4.11.: Relationship between bubble size (given by the equivalent diameter) and the characteristic shape parameters: roundness, elongation, and flatness.

4.6. Conclusion

In this study, we employed high-resolution synchrotron X-ray tomography in combination with deep learning-based image segmentation to systematically analyze hydrogen bubble evolution within VRFB electrodes under different applied potentials. Our quantitative analysis revealed that increased HER activity leads to the formation of larger, more irregular bubbles, which can impede electrolyte transport and reduce the effective electrochemical active area.

Importantly, our findings offer practical guidance for the optimization of VRFBs. First, my detailed characterization of bubble morphology underscores the significant influence of electrode microstructure on bubble retention. Optimizing the electrode design—by improving pore connectivity and tailoring fiber wettability through targeted surface treatments—may facilitate bubble release and promote a more uniform electrolyte distribution. Such modifications are anticipated to minimize bubble-induced blockage, thereby preserving the effective reaction area and enhancing overall battery performance.

Second, my study suggests that operational strategies can be refined to mitigate the adverse effects of HER. For example, implementing an intermittent or pulsatile pumping strategy could periodically increase electrolyte flow to sweep away accumulated bubbles, thus preventing flow choking and ensuring efficient mass transport. Future research, including numerical simulations such as the Lattice Boltzmann Method, will further elucidate the interplay between bubble dynamics and electrode microstructure. This, in turn, will support the development of semi-empirical models to guide the optimization of both electrode design and operating conditions.

In summary, our work not only advances the understanding of bubble evolution in VRFB electrodes but also provides concrete directions for optimizing electrode structure and operational strategies. These insights pave the way for enhanced battery performance and extended cycle life in practical applications.

5. A Deep Learning Approach for High-Throughput 3D Visualization and Bubble Quantification

5.1. Introduction

In chapter 4, the author demonstrated a deep learning-based image processing method for bubbles in VRFBs. Compared to traditional image analysis methods, deep learning can significantly improve the efficiency and accuracy of tomographic data processing, providing a powerful tool for studying bubble distribution and morphology in complex electrode structures. However, within this pipeline, the functional modules remain relatively fragmented: automatic bubble segmentation relies on a deep learning model, 3D reconstruction and morphological analysis are implemented using ITK toolkit, and feature parameter statistics and visualization require separate tools [77]. Due to the varying input and output formats between these tools, the research process often requires tedious data conversion and manual intervention, which is not only inefficient but also prone to introducing additional errors.

To address this limitation, the goal of this chapter is to develop an integrated image processing tool. This tool, with deep learning segmentation as its core, integrates all the functional modules in the previous chapter's pipeline, including automatic bubble identification, 3D reconstruction, morphological parameter extraction, and visualization, thereby automating and streamlining image processing within a unified software framework. This integrated workflow significantly reduces the need for manual intervention and cross-tool data conversion, enabling researchers to more directly and efficiently extract bubble statistics and geometric features

from experimental imaging data.

In this collaborative research, the pipeline concept and design were proposed by the authors. The data required for deep learning model training was prepared by the author and group members from Helmholtz Institute of Ulm. Data processing and analysis were also performed by the author. The specific software implementation and code development were completed by collaborator André Colliard-Granero. This chapter's work can be seen as a natural extension of the research in chapter 4. Its core contribution lies in integrating previously discrete analysis processes, achieving standardization and tooling for image processing. This work has been published as ref. [125], and subsequent content builds on this research.

5.2. Methodology

To achieve multi-category automatic segmentation of bubbles, electrolytes, membranes, and gaskets in tomographic images, several state-of-the-art deep learning network architectures were evaluated. Given the similarities in intensity and morphological characteristics between these target classes, traditional thresholding or shallow machine learning methods are insufficient. Therefore, U-Net and its variants were selected as the core framework, owing to their encoder–decoder architecture that has been widely validated in medical and materials image segmentation.

Four representative adaptations of the U-Net architecture were explored and assessed: U-Net with a ResNeXt101 backbone, Attention U-Net, U-Net 3+, and Swin U-Net.

- **ResNeXt101 U-Net**: integrates the ResNeXt101 backbone with the U-Net framework. Its split-transform-merge strategy increases the model's "cardinality", i.e., the number of parallel paths within each block, enhancing feature extraction without significantly increasing network depth or width [126]. This design improves the ability to capture complex patterns.

- **Attention U-Net**: augments the baseline U-Net with attention gates at each decoder skip connection. This mechanism emphasizes relevant pixels and suppresses irrelevant background information, enabling better delineation of fine structures and boundaries [127].

- **U-Net 3+**: incorporates deep supervision and multi-scale skip pathways to facilitate direct feature transfer between encoder and decoder layers [128]. This design bridges semantic gaps and strengthens recognition of structures at varying scales.
- **Swin U-Net**: combines the Swin Transformer with U-Net, enabling efficient modeling of long-range dependencies while retaining the hierarchical encoder–decoder structure. Its self-attention mechanism captures both global and local contextual information, improving segmentation accuracy across different scales [129].

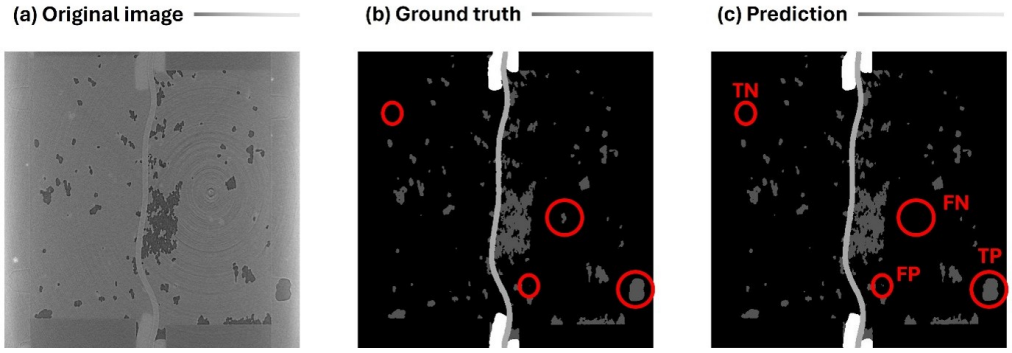

Figure 5.1.: Comparison of (a) tomographic slice extracted from a VRFB along with the manually annotated ground truth and predicted mask. The comparison of (b) and (c) denote examples of true-positive (TP), true-negative (TN), false-positive (FP), and false-negative (FN) predictions.

Following model training, their performance was systematically evaluated using established metrics. Precision, recall, and the F1-score were employed to quantify segmentation quality by comparing the predicted class labels with ground-truth annotations. In this context, true positives (TP) are pixels correctly classified into their respective classes, true negatives (TN) are pixels accurately identified as background, false positives (FP) are pixels incorrectly assigned to a class, and false negatives (FN) are pixels omitted from their correct class. These metrics collectively provide a comprehensive assessment of model performance, balancing detection accuracy and error minimization. The three metrics are defined as,

$$\text{Precision} = \frac{TP}{TP + FP} \tag{5.1}$$

$$\text{Recall} = \frac{TP}{TP + FN} \tag{5.2}$$

$$F1 = 2 \times \text{Precision} \times \frac{\text{Recall}}{\text{Precision} + \text{Recall}} \tag{5.3}$$

Once the segmentation maps were generated, they were stacked into three-dimensional volume fractions to enable subsequent statistical analyses. Key descriptors extracted from the segmented data included the total bubble volume, bubble-to-electrolyte ratio, and bubble density distributions across multiple planes. In addition, individual bubbles were isolated and further analyzed using advanced computer vision algorithms (OpenCV) [130], allowing quantification of morphological features such as volume fraction, elongation, flatness, sphericity, wall proximity, and orientation. These descriptors provide insights into both the statistical and spatial characteristics of bubbles in the electrode microstructure.

In challenging examples, the predictive model occasionally introduced artifacts or noise into the segmentation maps. We implemented two corrective functions to mitigate these inaccuracies and preserve the integrity of our statistical analyses. Initially, a filter was applied across the entire 3D volume stack to eliminate detections of bubbles that appeared one-dimensional (1D), based on the fact that real bubbles should span at least two voxels in depth, with 1D detections likely arising from model-induced noise. Subsequently, a second function assessed the morphological characteristics of the bubbles, excluding artifacts characterized by significant non-convexity and irregular shapes, which provoked errors in the determination of bubble metrics.

The derived measurements were systematically visualized to elucidate the system's characteristics. Advanced 3D visualization techniques were developed using the Visualization Toolkit (VTK) library [86, 131], enabling interactive volume exploration with customizable color mappings based on the measured parameters. Furthermore, the software enabled users to create and export short GIFs depicting the rotating volume, thus enhancing the presentation and visualization of the results.

5.3. Model Comparison

Accurate segmentation of tomographic images is essential for quantitative analysis of bubble dynamics in VRFBs. To this end, four U-Net variants were evaluated: a U-Net with a ResNeXt101 backbone, Attention U-Net, U-Net 3+, and Swin U-Net. Each model was initialized with pre-trained ImageNet weights to leverage transferable features and trained on a dataset comprising 1894 annotated training images and 400 validation images. Training was conducted for 200 epochs with a batch size of 8 using the Adam optimizer [132] and a categorical focal loss function [133]. The learning rate was dynamically adjusted during training, ranging from 10^{-4} to 10^{-6}, depending on convergence performance.

Quantitative performance metrics, including precision, recall, and F1-score, were used to assess model accuracy (Table 5.1). All models demonstrated high effectiveness, with F1-scores above 94%. Among them, the ResNeXt101 U-Net achieved the best overall balance, attaining a precision of 98%, recall of 97%, and F1-score of 97%. The slightly higher recall of this architecture reduced the likelihood of false negatives, while maintaining high precision minimized the misclassification of background regions as bubbles. It reinforces its applicability to complex segmentation tasks where precise detection and the reduction of false positives are paramount.

Table 5.1.: Comparison of different U-Net models trained on a unique dataset. The performance of the models is assessed by employing precision, recall, and F1-score as metrics.

Model	Precision (%)	Recall (%)	F1-score (%)
U-Net with ResNeXt101 backbone	98	97	97
Attention U-Net	98	96	97
U-Net 3+	97	94	96
Swin U-Net	96	92	94

Beyond quantitative metrics, visual evaluation was performed using datasets not encountered during training, encompassing four representative electrode states: completely gas-filled (dry), half-filled (half soaked), fully electrolyte-filled (soaked), and post-HER cycling. As illustrated in Figure 5.2, all models exhibited acceptable performance across different configurations. However, the U-Net with a ResNeXt101 backbone consistently provided superior delineation of bubbles and membranes, while simultaneously reducing false positive detections compared to other models. Attention U-Net and U-Net 3+ occasionally misclassified empty electrode

regions as bubbles, and Swin U-Net struggled with sparse bubble configurations, resulting in overprediction.

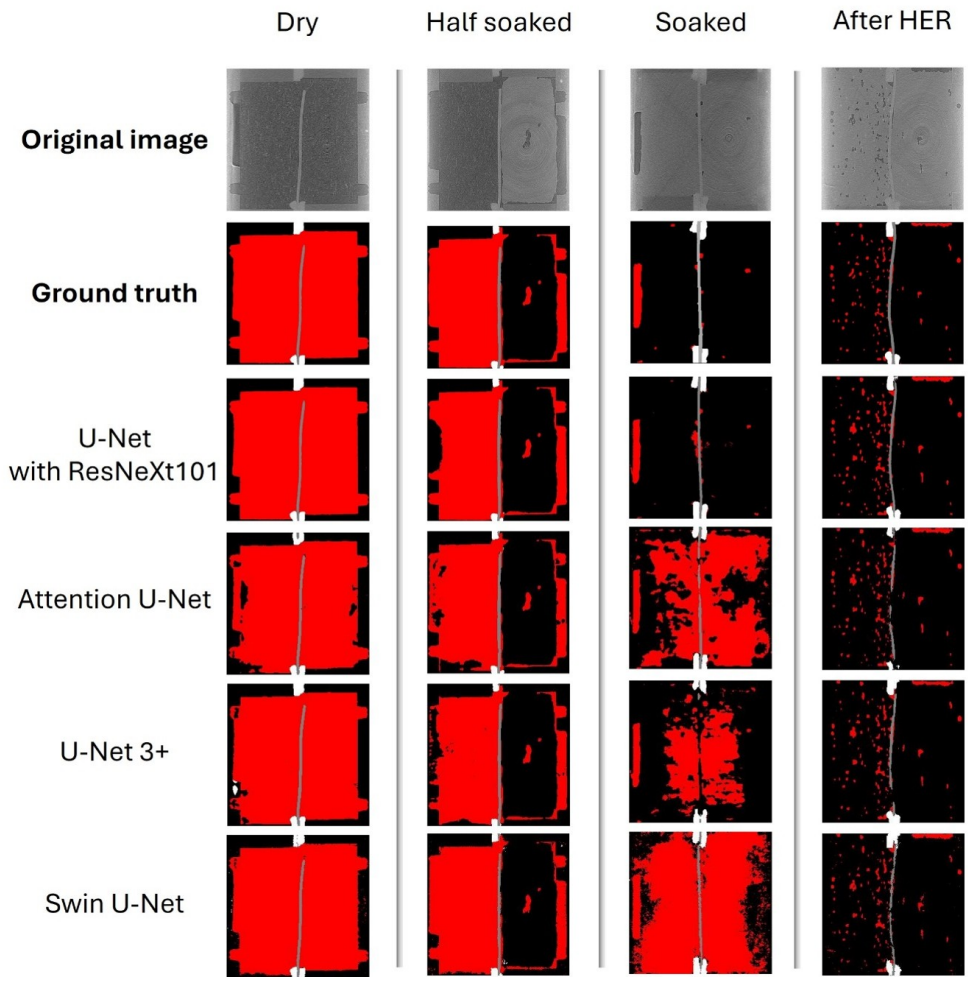

Figure 5.2.: Comparative visualization of the original tomographic images, manual annotations, and predictions from four U-Net architectures across distinct electrode states: completely gas-filled (dry), half-filled (half soaked), fully electrolyte-filled (soaked), and post-HER cycling. Red: bubbles, grey: membranes, white: gaskets, black: electrolyte.

A filtering step was further applied to reduce artifacts and spurious detections in challenging cases. Quantitative evaluation on an unseen dataset revealed that prior to filtering, 3255 bubbles were detected, corresponding to a total bubble volume fraction of 4.25%. After filtering, the bubble count was reduced to 488, while the total bubble volume fraction decreased only slightly to 4.20%, representing a change of 1.2%. These results confirm that the filtering

process effectively removes noise and false positives without compromising volumetric quantification, thereby ensuring reliable individual bubble analysis.

5.4. Software Capabilities and Visualization

The developed software provides an integrated environment for region-specific analysis, bubble quantification, and advanced visualization of tomographic datasets. Figure 5.3–5.5 illustrate the main functionalities.

Figure 5.3a demonstrates the software's ability to conduct region-specific analysis tailored to specific requirements. Although analyses can encompass the entire cell, specialized computer vision algorithms were developed to discern between the cathode and anode sections. To achieve this, the membrane on both sides was delineated, enabling pixel-exact separation of the electrodes. This approach is particularly advantageous for membranes with irregular shapes, which cannot be separated through conventional, arbitrary methods. Once the region of interest is identified, the feature extraction process can be initiated from the segmented volumes. By classifying voxels into four distinct categories, it becomes feasible to quantify the total gas volume within the cell and determine the bubble-to-electrolyte ratio for system characterization.

An additional outcome derived from the segmentation process is the generation of a two-dimensional bubble density distribution plot across the cell, which is depicted as a density map from the orthogonal planes XY, XZ, and ZY, as illustrated in Figure 5.3b. Predictions across each plane are aggregated by filtering to retain only bubble voxels (set to "1"), while designating the background as "0." These density maps are then created by consolidating the segmented bubble data into a singular image from various perspectives. This aggregation results in regions densely populated with bubbles being assigned higher values, visually represented by warmer hues on the density map. Cooler colors indicate areas with fewer bubbles, while greener hues mark intermediate zones. The density maps from the XY and XZ planes in Figure 5.3b qualitatively suggest that, in this example, bubbles are uniformly distributed across the cell, with an increasing concentration near the central membrane. This visual representation aids in qualitatively assessing bubble distribution and accumulation within the cell from a

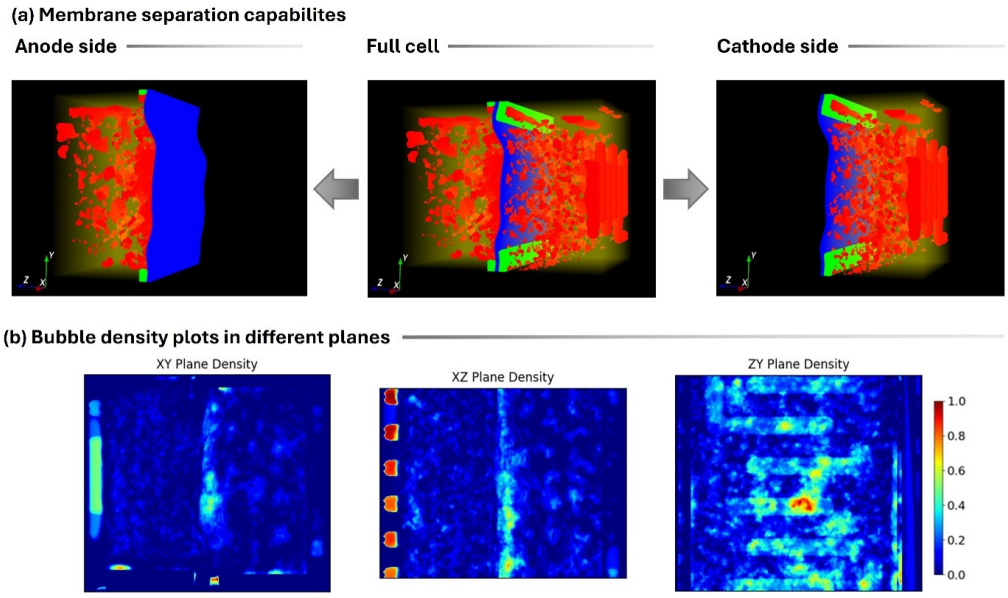

Figure 5.3.: (a) Precise electrode separation achieved by delineating the membrane for pixel-wise segmentation of the electrodes. (b) Bubble density distribution across orthogonal planes XY, XZ, and ZY.

two-dimensional perspective, avoiding the need for 3D rendering.

The methodology further enables the rendering of volumes in three dimensions, facilitating the extraction of specific features of interest. In this process, segmented bubbles are isolated by a function that segregates each bubble surrounded by background voxels and assigns a unique identifier. This segregation permits detailed analysis of each bubble, including the extraction of morphological attributes through computer vision techniques. These analyses provide insights into the structural properties of individual bubbles, elucidating characteristics commonly investigated in material science. The derived parameters collectively provide a comprehensive characterization of bubble morphology, thereby enhancing the understanding of bubble behavior and interaction within the electrode environment. As depicted in Figure 5.4, these measurements are subsequently visualized in corresponding histograms to provide an overview of the system. Furthermore, direct visualization of these measurements is supported by rendering the 3D volume, in which each bubble is color-mapped according to its measured values. This interactive 3D visualization capability significantly improves comprehension of property distributions throughout the cell and can be generated automatically. In addition, the software

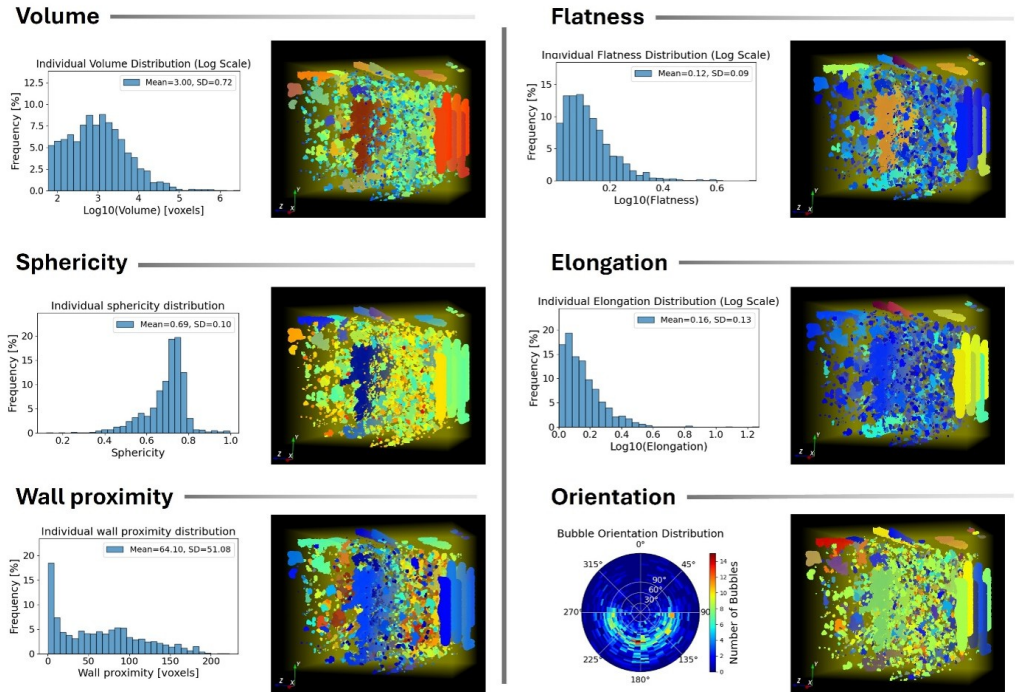

Figure 5.4.: Analysis of individual bubble shape characteristics within segmented volumes. Histograms show the distributions of volume, flatness, elongation, sphericity, wall proximity, and orientation, while 3D renderings visualize the corresponding color-mapped features.

includes functionality to create 360° GIFs of the volume of interest, facilitating later visualization or presentation of findings.

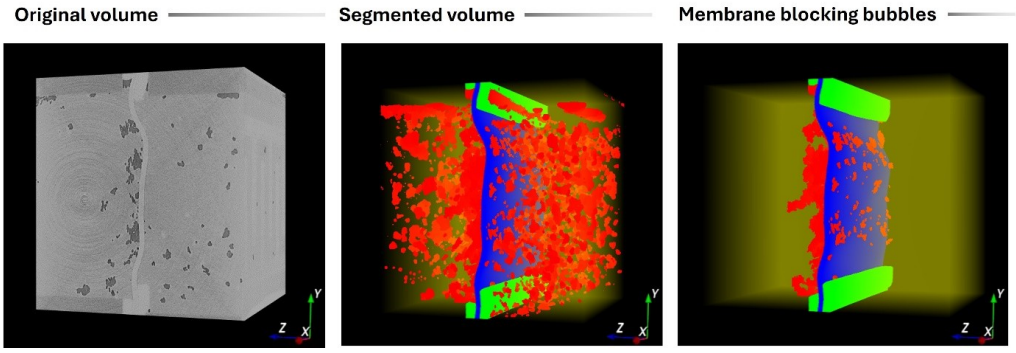

Figure 5.5.: Membrane blockage analysis. From left to right: original tomographic volume, segmented volume, and visualization of bubbles in direct contact with the membrane.

By integrating automated volume segmentation with advanced computer vision algorithms, specialized functions tailored for specific use cases have been developed, thereby enhancing

system-level understanding. A dedicated function was implemented to delineate the detailed contour of the central membrane combined with pixel-wise bubble segmentation, pioneering an approach for conducting membrane blockage analysis. As demonstrated in Figure 5.5, this methodology enables quantification and visualization of bubble voxels in contact with the membrane, laying the groundwork for subsequent correlation analyses.

As illustrated in Figure 5.5, the function computes the extent of the membrane's surface area obstructed by bubbles and visualizes the implicated bubbles using an interactive 3D tool, enabling detailed examination. The primary objective of this approach is to facilitate future studies that investigate correlations between membrane blockage and potential performance degradation in the system. By quantifying the membrane area affected by bubble obstructions, contributing factors to performance losses can be identified and analyzed, thereby providing insights into optimizing system efficiency and reliability.

5.5. Case Study: Validation with Modified Electrodes

To further illustrate the tool's capabilities, it was applied to a representative set of synchrotron X-ray tomography datasets of vanadium electrolyte electrodes modified with three different materials: poly(o-toluidine) (POT), Fe–N–C, and Vulcan. This use case was directly based on the study by Köble et al. [134], who had performed comprehensive electrochemical characterization of the same electrode samples, including cyclic voltammetry (CV), electrochemical impedance spectroscopy (EIS), and distribution of relaxation times (DRT) analysis. However, their study lacked 3D bubble image analysis of the accompanying tomography datasets.

In the tomography scanning experiment, a three-electrode setup was employed, featuring carbon felt electrodes with modification as the working electrode, a thermally activated carbon felt as the counter electrode, and an Ag/AgCl reference electrode (3 M NaCl, $E = 0.209$ V vs. SHE) [48, 134]. The electrolyte was 0.1 M $VOSO_4$ dissolved in 2 M H_2SO_4. Before inducing hydrogen evolution, electrodes were thoroughly wetted and scanned once by X-ray tomography to identify residual bubbles. Figure 5.6 shows the resulting 3D reconstructions of bubble distributions and the results of quantitative bubble analyses. In Figure 5.6a, the bubble volume fraction R_{bv} in the POT-modified electrode before HER was about 3.03%, indicating that

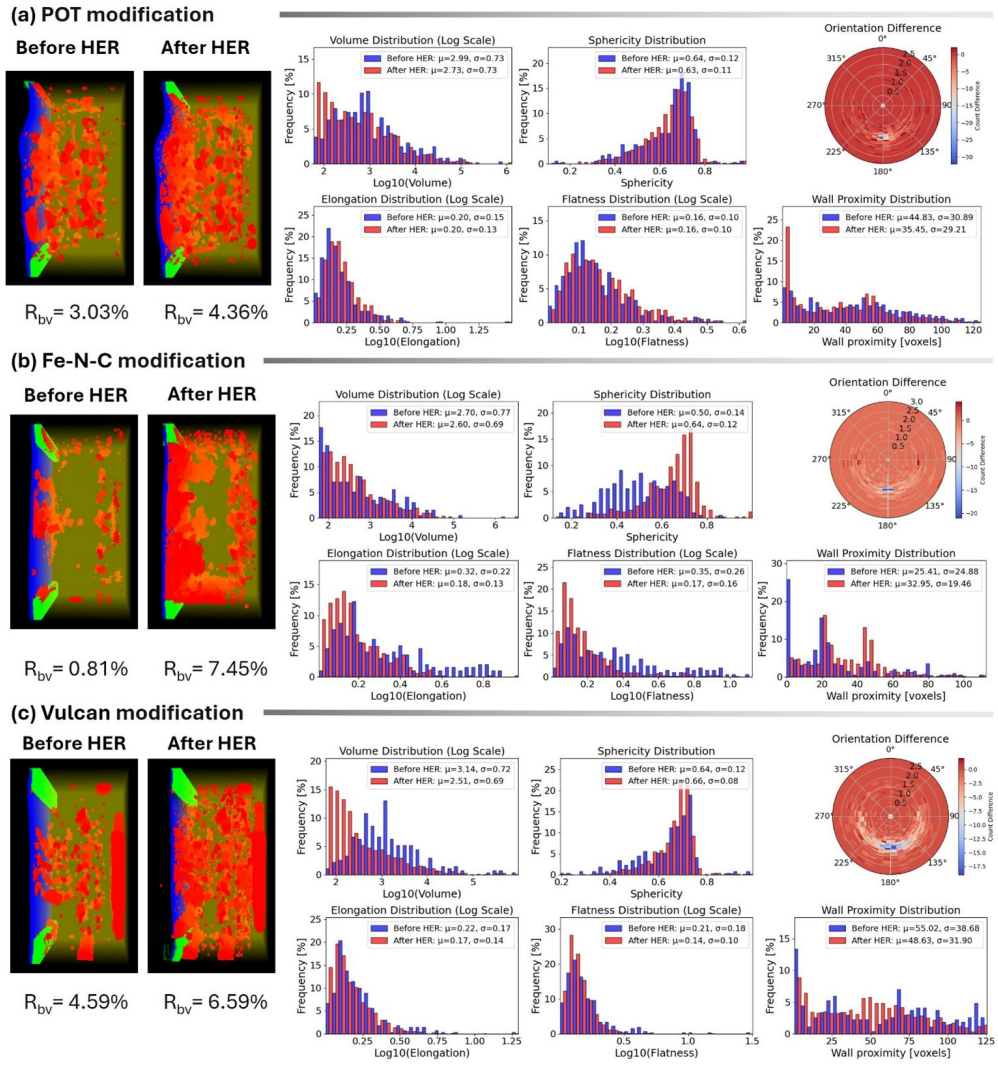

Figure 5.6.: Bubble spatial distribution and morphology of three modified electrodes: (a) POT, (b) Fe–N–C, and (c) Vulcan, before and after HER. Red indicates bubbles, while other colors correspond to the electrode and electrolyte phases. The bubble volume fraction (R_{bv}) is annotated. Histograms illustrate distributions of bubble morphological parameters, including volume fraction, sphericity, elongation, flatness, wall proximity, and orientation.

a moderate amount of air was trapped even after complete wetting. In the Fe–N–C-modified electrode (Figure 5.6b), R_{bv} was only 0.81%, implying an excellent ability to remove gaseous species and avoid the formation of large bubbles. In Figure 5.6c, the Vulcan electrode exhibited the highest residual bubble volume fraction at 4.59% before HER, suggesting that additional carbon particles hindered the effective removal of gas during the permeation process. The bub-

ble volume distribution histogram shows that the Fe–N–C-modified electrode contained mostly small bubbles, while the Vulcan electrode displayed a broader distribution. Moreover, bubbles in both the POT- and Vulcan-modified electrodes exhibited more obvious shape deformation (lower sphericity and higher elongation), indicating that the local pore structure may limit bubble release.

Analysis of bubble orientation further revealed that in electrodes with a more anisotropic pore structure, bubbles tended to align along specific directions. This preferential orientation was especially evident in the POT- and Vulcan-modified electrodes, where the directional bias likely reflected the influence of fiber alignment and pore connectivity on bubble nucleation and growth. These findings are consistent with experimental data (dynamic vapor sorption and flow injection experiments) reported by Köble et al. [134], indicating that the Fe–N–C-modified electrode possessed good porosity and wetting behavior under flow conditions. To induce bubble for-

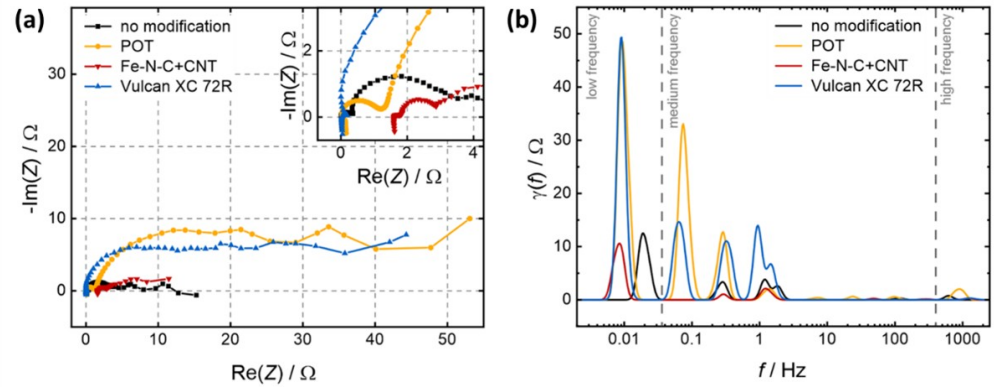

Figure 5.7.: (a) Nyquist plots from EIS of the thermally activated carbon felt without modification and the modified samples (inset: zoomed in on high frequencies) and (b) the corresponding DRT spectra. The measurements were conducted in 0.1 mol/L $VOSO_4$ dissolved in 2 mol/L H_2SO_4 at a potential of 1.05 V vs. RHE, at a flow rate of 15 mL/min, applying a perturbation of 5 mV. [134]

mation during the HER, a potential of –0.5 V vs. Ag/AgCl (approximately –0.3 V vs. RHE) was applied for 5 min. A second tomography scan was then performed, and the results were compared to the initial images (Figure 5.6). By comparing bubble ratios before and after HER, the catalytic effect of each modified electrode under negative potential could be rationalized. For the POT-modified electrode, R_{bv} increased from 3.03% to 4.36%, a modest rise indicating that the HER was partially suppressed. In contrast, R_{bv} in the Fe–N–C-modified electrode

increased markedly, from 0.81% to 7.45%, highlighting the strong catalytic activity of the iron-based sites for hydrogen production. This observation was consistent with electrochemical characterizations showing that Fe–N–C-modified electrodes significantly enhance side reactions at the negative half-cell of VRFBs (as shown in Figure 5.7) [134]. The Vulcan-modified electrode also showed a significant increase in R_{bv}, from 4.59% to 6.59%. The additional gas formed in this case can be attributed to carbon black agglomerates that promote bubble nucleation.

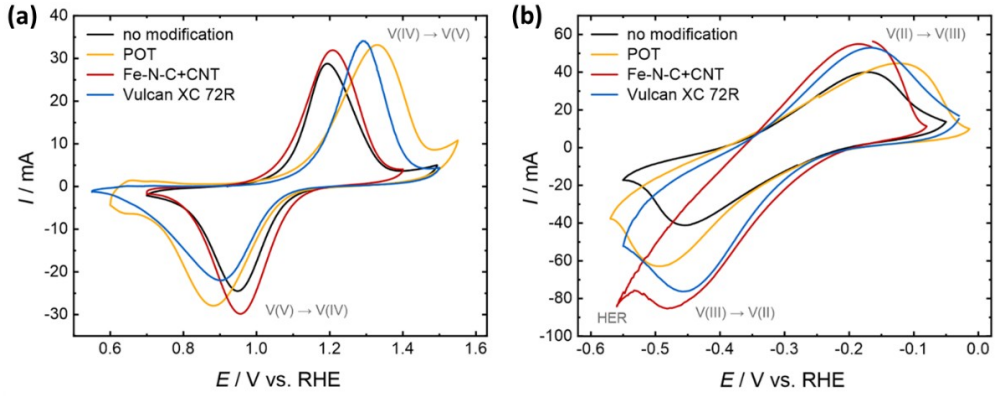

Figure 5.8.: CV measurements of the thermally activated carbon felt without modification and the modified samples conducted in a three-electrode setup in 0.1 mol/L $VOSO_4$ in 2 mol/L H_2SO_4 at a scan rate of 2 mV/s in (a) the positive half-cell (vanadium(IV) electrolyte) and (b) the negative half-cell (vanadium(II) electrolyte). [134]

These observations were in line with electrochemical trends reported by Köble et al. (as shown in Figure 5.8) [134]. In their CV measurements, Fe–N–C- and Vulcan-modified electrodes exhibited higher HER current densities at the negative half-cell, supporting the tomographic finding of increased bubble formation in these samples. Additionally, EIS and DRT analyses revealed that the POT-modified electrode displayed increased polarization resistance and mass transport impedance, likely due to gas entrapment—an effect also captured in the 3D reconstructions as persistent near-wall bubbles.

Together, the tomographic and electrochemical data highlight the distinct behavior of each electrode material: Fe–N–C demonstrates strong HER activity that leads to significant bubble growth despite favorable performance in the V(IV)/V(V) reaction; POT suppresses HER but may hinder liquid transport; and Vulcan exhibits intermediate behavior in both catalytic and

transport characteristics.

Overall, this use case demonstrates that the proposed 3D bubble image analytical tool can extract meaningful structural information from complex tomographic datasets and effectively link it with known electrochemical behavior. By capturing key features such as bubble volume, shape deformation, and spatial orientation, the tool enables detailed investigation of gas evolution and retention phenomena in porous electrodes. These insights contribute to a deeper understanding of gas–liquid interactions in electrochemical systems and provide a valuable basis for future efforts aimed at optimizing electrode architectures, operating conditions [77], and material selection. The successful application to existing datasets further illustrates the practicality and generalizability of the tool, paving the way for its broader adoption in the study of gas-involved electrochemical processes.

5.6. Conclusion

In conclusion, the work presented in this chapter establishes a general framework for an expedited investigation into the effects of trapped bubbles in vanadium redox flow batteries, utilizing three-dimensional tomographic images as a rich data source. Through this study, software has been developed that is capable of segmenting synchrotron X-ray tomographic images into four relevant categories: bubbles, electrolyte, membrane, and gasket. Furthermore, the framework enables the autonomous differentiation between electrodes, quantification of bubble volume fractions, individual bubble shape analysis, generation of two-dimensional bubble density maps, and computation of membrane blockage.

In the application example, electrodes modified with poly(o-toluidine) (POT), Fe–N–C, and Vulcan were compared. The analysis demonstrated that the tool is able to distinguish differences in bubble dynamics before and after the hydrogen evolution reaction. The results revealed that the Fe–N–C modification caused a pronounced increase in bubble volume after hydrogen evolution, indicating markedly enhanced catalytic activity for hydrogen production, whereas the POT modification showed only a modest increase. Although the extracted morphological descriptors are at present difficult to relate directly to electrochemical behavior, future work may combine them with numerical studies, such as multiphase flow or three-dimensional transport

simulations, to assess the potential impact of bubble morphology on fluid resistance, local reactant accessibility, and overall cell performance. These insights are valuable for understanding bubble dynamics in vanadium redox flow batteries and provide an important basis for electrode optimization.

The analytical tool presented here allows experimentalists to replace the time-consuming and error-prone manual analyses of synchrotron tomographic images of vanadium redox flow batteries. It enables the rapid quantification of bubbles. In addition, the tool's advanced automation and visualization capabilities allow swift visual comparisons across different volume fractions, facilitate comparative degradation analyses between cells, and pave the way towards four-dimensional analyses of bubble dynamics with resolution in both space and time. The tool can also be readily extended to other electrochemical systems, such as water electrolysers, where bubble formation and transport play a critical role in determining performance and durability. Plans are in place to make this tool publicly accessible, with a design that supports seamless incorporation of additional feature extraction functions, new models, and diverse visualization techniques according to the needs of theoretical and experimental research.

6. Parasitic Hydrogen Bubble Evolution in Vanadium Redox Flow Batteries: A Lattice Boltzmann Study

6.1. Introduction

In the previous chapter, synchrotron X-ray tomography was employed to investigate the evolution of hydrogen bubbles in porous carbon felt electrodes during HER. While these experiments provided valuable insights into the macroscopic distribution and size variation of bubbles under different operating conditions, the spatial resolution and limited field of view made it difficult to directly observe the interaction between individual bubbles and the local microstructure of the electrode.

To address this limitation, this chapter focuses on numerical simulations using LBM to study the dynamic behavior of bubbles at the pore scale. Specifically, the author applied a three-dimensional immiscible color-gradient LBM model [104, 105] to simulate reactive gas–liquid flow within carbon felt electrodes of varying compression ratios. The electrode geometries were reconstructed from high-resolution X-ray tomography scans, allowing users to resolve the interplay between bubble nucleation, growth, coalescence, and detachment, and the surrounding solid structure. This modeling framework complements experimental observations and enables a more detailed understanding of how local microstructural features influence bubble dynamics and mass transport, ultimately impacting the electrochemical performance of VRFB systems.

6.2. Channel flow

To gain a basic understanding of bubble evolution in complex geometries, we have simulated a reactive flow in a simplified flat channel. The boundary conditions remained as described in Section 3.3.2, but the geometry was simplified to a channel ($50 \times 10 \times 60$ lattice sites), with two planar walls perpendicular to the x-axis serving as reaction walls. Initially, the computational domain was filled with a uniform electrolyte density of 1, which was then accelerated by a pressure drop ($\Delta P = 6 \times 10^{-4}$ l.u.). Figure 6.1(a) shows the 3-D visualization of the bubble distribution in the channel. The removal of the gas phase was not continuous due to the formation of bubbles, which gradually grow. In order to conduct a qualitative analysis of bubble growth, we have calculated the electrolyte saturation, shown in Figure 6.1(b), and the bubble coverage, shown in Figure 6.1(c), in the computational domain. The electrolyte saturation is defined as the ratio of the liquid volume to the total pore volume in the computational domain, while the bubble coverage is defined as the ratio of the bubble-solid contact area to the total surface area of the electrode. In Figure 6.1(b), the saturation and in Figure 6.1(c), the bubble coverage are shown. Both electrolyte saturation and bubble coverage exhibit quasi-periodic fluctuations once the flow reaches a quasi-steady state. Each fluctuation indicates the coalescence, growth, and removal of a large bubble. However, at the maximum reaction rate case, $kr = 5\times 10^{-5}$ l.u., a sudden jump was observed at $t = 1.5 \times 10^4\ \delta t$, as visible in Figure 6.1(b) and Figure 6.1(c). This behavior occurred during the early developing stage, where the flow rate was low and bubble growth was rapid. The limited geometric width of pores in this case restricts the bubble's growth, causing it to transition from a hemispherical shape to a semi-cylindrical shape. Once the flow entered the steady state, the formation of semi-cylindrical bubbles no longer occurred. In this simplified geometry, saturation and bubble coverage serve as effective metrics for characterizing bubble evolution, including growth, coalescence, and removal. Therefore, the author continued using these two statistical variables in subsequent analyses.

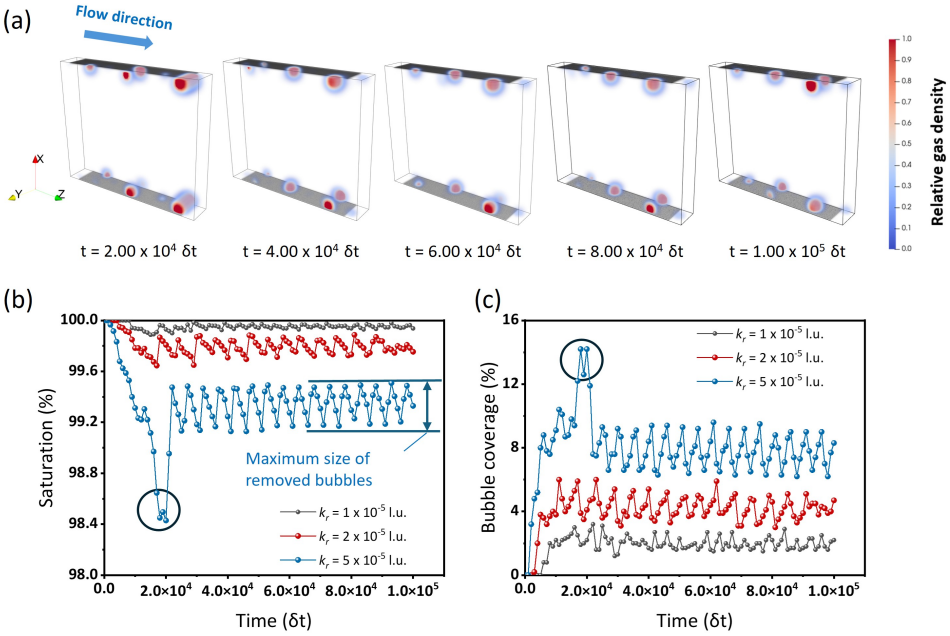

Figure 6.1.: a) 3D visualization of bubble distribution in the electrolyte domain during the simulation. The color map represents the relative gas density; b) electrolyte saturation curve plotted as a function of time steps for different reaction rates; c) bubble coverage curve over time, also plotted for the same reaction rates.

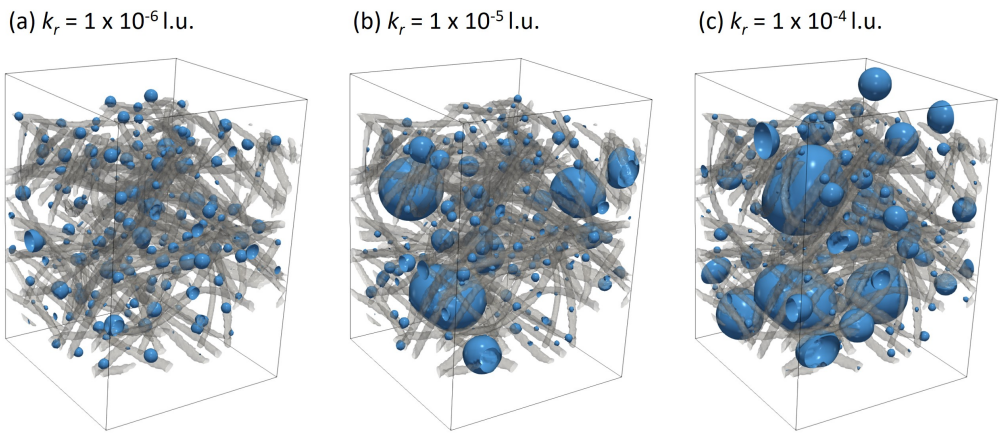

Figure 6.2.: 3-D visualization of the spatial bubble distribution at $t = 1.57 \times 10^5 \delta t$: (a) $k_r = 1 \times 10^{-6}$ l.u.; (b) $k_r = 1 \times 10^{-5}$ l.u.; (c) $k_r = 1 \times 10^{-4}$ l.u..

6.3. Effect of reaction rate

The rate of the HER is influenced by various factors, including electrode materials, electrolyte properties, operating conditions, and the aging of the electrode. To anchor the numerical range used here, a roughly derivation was conducted based the parameters measured by Schweiss et al. [108]. It was found that the reaction rate k_r should be on the order of 10^{-11} to 10^{-7}. The bubble evolution under this k_r value was too slow to be observed within this simulation timeframe, especially since the author ignored the volume expansion effect. Therefore, for a qualitative analysis of how the HER rate influences bubble evolution, the author accelerated the process by using reaction rate magnitudes ranging from 10^{-6} to 10^{-4}. Additionally, the pressure drop across the inlet and outlet was set to 1×10^{-2} l.u. to aid bubble transport within the simulation timeframe and the CR of the electrode was chosen as 25%.

Figure 6.2 illustrates the spatial distribution of bubbles at $t = 3.0 \times 10^5 \delta t$ for varying HER rates during reactive flow in the carbon felt. At the small reaction rate (Figure 6.2(a)). Bubbles grew slowly and remain mostly attached to the fiber surface. The movement of small bubbles toward each other and their coalescence were primarily driven by surface tension forces, which worked to minimize the overall surface energy. At moderate reaction rates (Figure 6.2(b)), bubbles grew more rapidly, and many of them detached from the fiber surface, moving under the influence of the flow. However, bubble movement was not always continuous; some bubbles coalesced

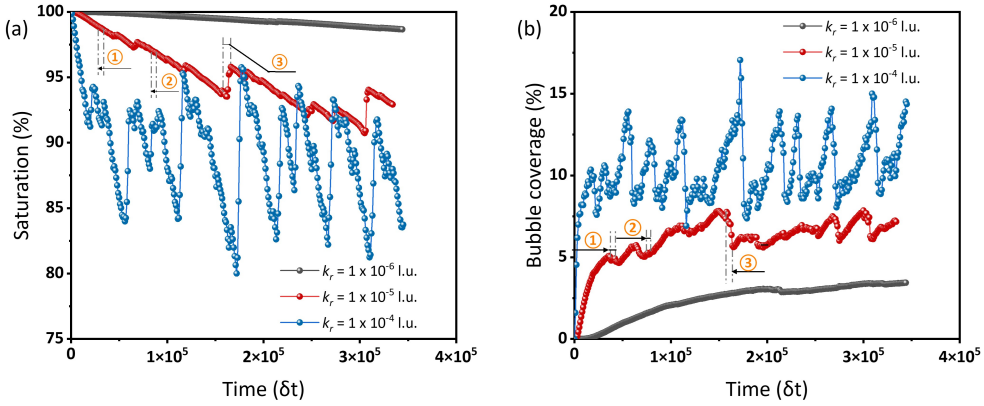

Figure 6.3.: Variation of (a) electrolyte saturation and (b) bubble coverage over simulation time at different reaction rates.

during transport, becoming temporarily blocked by dense fiber areas. Once these coalesced bubbles reached a larger size, they were able to resume movement. As the reaction rate increased, bubbles grew larger and detached more rapidly from their fiber surface. This leaded to a decrease in electrolyte saturation and a reduction in the effective reaction area, as larger bubbles occupied more space and obstructed the flow path. These effects were reflected in the electrolyte saturation and bubble coverage curves shown in Figure 6.3, which displayed regular fluctuations, consistent with the trends observed in the channel flow study (section 6.2). Each sudden change in these statistical curves corresponded to the detachment and removal of a large bubble. However, the increased reaction rate also resulted in uneven gas release and greater obstruction to electrolyte transport, ultimately inhibiting the overall performance.

The removal of a trapped bubble within the porous electrode was further investigated at a reaction rate of $k_r = 1 \times 10^{-5}$ l.u., providing insights into bubble evolution dynamics. Figure 6.4 illustrated three stages of the bubble evolution highlighted also in Figure 6.3: ① the coalescence of smaller bubbles to form Bubble 1, ② the coalescence of smaller bubbles form to Bubble 2, and ③ the merging of Bubbles 1 and 2 and detachment of the resulting larger bubble. The tracked area was indicated by the black dashed box. Figure 6.4(a) and 6.4(b) showed the formation processes of Bubble 1 and Bubble 2, respectively. Both were formed by the coalescence of smaller “seed bubbles”, which were newly-formed small bubbles either recently detached from the carbon surface or still adhered around it. The movement of ‘seed bubbles’ was primarily

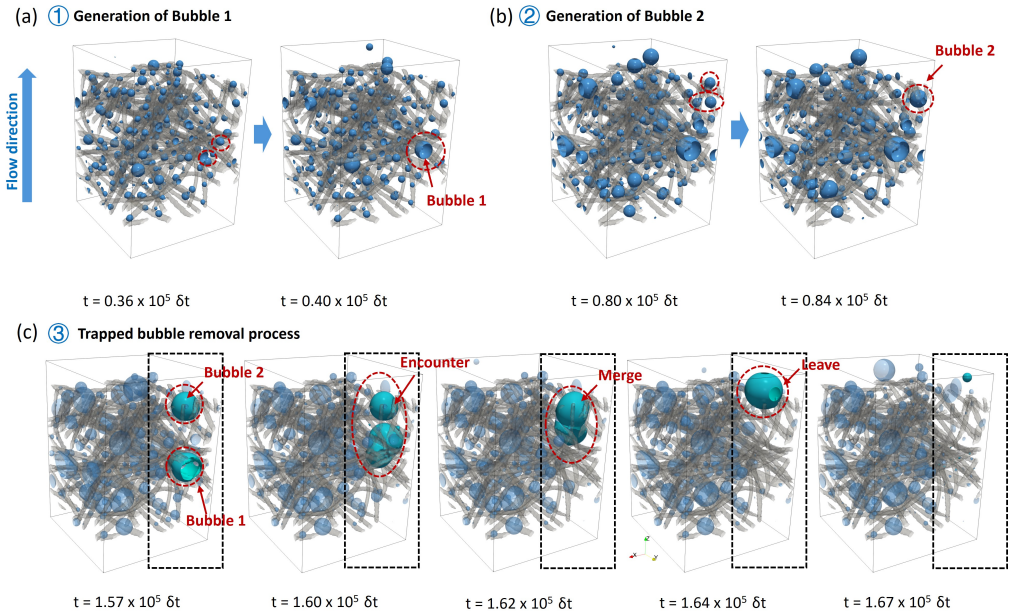

Figure 6.4.: Bubble evolution process: (a) generation of bubble 1; (b) generation of bubble 2; (3) removal process of trapped bubble.

governed by surface tension forces, including both solid–fluid (carbon surface) and fluid–fluid (electrolyte–bubble) interactions. These forces caused the bubbles to coalesce and influence their detachment from surfaces, which meant their movement direction was not always aligned with the flow. Figure 6.4(c) showed the bubble removal process. At $t = 1.57 \times 10^5 \delta t$, Bubble 1 and Bubble 2 were still observed to be trapped in the same position, with only their size increasing. Then Bubble 1 first broke away from the fiber restraint and started to move, eventually merging with Bubble 2 along its path and exiting the computational domain. From this perspective, bubbles were not trapped forever in so-called pinning sites. Each pinning site had different constraints on the bubble, depending on the surrounding microstructure. Once the bubble size exceeded its constraint limit, the bubble lifted off and moved away. Figure 7 only depicted a few examples of the movement of bubbles in the electrode. The overall picture was composed of many similar processes causing fluctuations in the overall performance, which could be treated in a statistical manner.

Figure 6.5(a) presented the average values of electrolyte saturation and bubble coverage at different reaction rates after $1.5 \times 10^5 \ \delta t$, indicated by solid dots. The error bars were com-

puted by tracking the saturation values over time during the quasi-steady state. The top of the error bar was the maximum value observed, and the bottom was the minimum value observed during that period. The results showed that when k_r was below 1×10^{-5} l.u., saturation decreased sharply, while bubble coverage increased rapidly with rising k_r. However, when k_r exceeded 1×10^{-5} l.u., both saturation and bubble coverage changed more gradually. Figure 6.5(b) showed variations in electrolyte slice saturation along the flow direction for different k_r, comparing their difference between the minimum, average, and maximum overall saturation levels. The horizontal axis in Figure 6.5(b) was normalized from 0 to 1, with the unit being the total flow length L. At $k_r = 1 \times 10^{-6}$ l.u., the difference in slice saturation curves was minimal due to the lack of bubble coalescence. However, at $k_r = 1 \times 10^{-5}$ and 1×10^{-4} l.u., significant variations were observed in the slice saturation curves around the relative position of 0.4–0.8 L, where a distinct trough appeared at the minimum saturation. This suggested the presence of a bubble pinning site in this region, aligning with the phenomenon observed in Figure 6.4. Another pinning site could be observed in the region of 0.1–0.4 L. At $k_r = 1 \times 10^{-5}$ l.u., the trapped bubbles remained largely unremoved, as indicated by the similar slice saturation values across average, maximum, and minimum saturation states. The lowest slice saturation in this region stays around 87%, suggesting that the flow conditions are insufficient to dislodge these bubbles, resulting in a stable, persistent bubble distribution. In contrast, at $k_r = 1 \times 10^{-4}$ l.u., a different behavior was observed. During the minimum saturation state, the lowest slice saturation in the region from 0.1 L to 0.4 L dropped below 85%, indicating the formation of more substantial gas voids. However, at the maximum saturation state, these trapped bubbles were effectively removed, suggesting that the higher reaction rate facilitates the periodic release of bubbles, which reduced localized gas accumulation. This observation aligned with Scheel et al.'s findings [107], which showed that larger bubbles were removed more efficiently because coalescence facilitated their detachment.

6.4. Effect of flow rate

The negative impact of bubbles on battery performance could be effectively reduced by adjusting the flow rate of the electrolyte. In present simulations, the flow rate was controlled by the

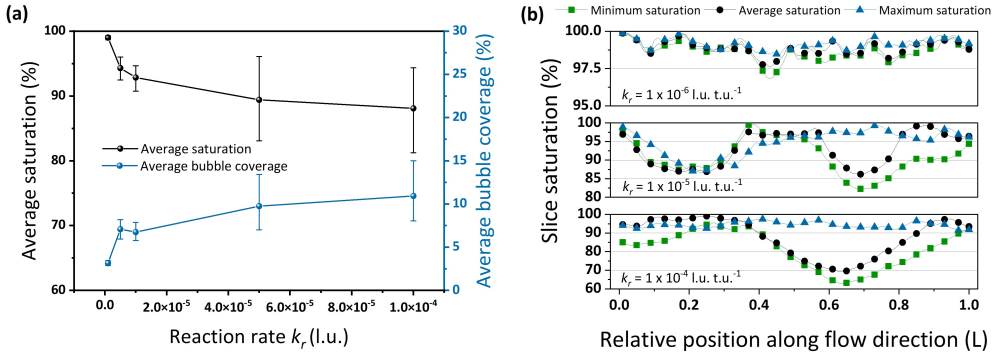

Figure 6.5.: (a) Average electrolyte saturation and bubble's coverage vary with reaction rate. Electrolyte slice saturation changes along the flow direction; (b) Electrolyte slice saturation changes along the flow direction.

pressure drop along flow direction. Here, $\Delta P = 1 \times 10^{-4}$ l.u. was equivalent to applying a pressure drop of 42.7 Pa between inlet and outlet of the porous media. The reaction rate k_r was fixed as 1×10^{-5} l.u., and the CR is 25%.

Figure 6.6 depicted the change of the electrolyte saturation and bubble coverage with time under different pressure drops. In order to more accurately analyze the bubble evolution, the author extended the simulation duration to $t = 1.0 \times 10^6 \delta t$ to better capture long-term bubble dynamics. At the lowest flow rate ($\Delta P = 1 \times 10^{-4}$ l.u.), the driving force was insufficient to promote efficient bubble removal process. As a result, bubble motion was significantly hindered, and gas accumulated within the porous structure. During the early stage of the simulation (before $t = 1.60 \times 10^5 \delta t$), the saturation decreased monotonically in Figure 6.6(a), while the bubble coverage exhibited a plateau in Figure 6.6(b). Although the volume of bubbles in the electrode was growing, the bubble coverage did not vary much. This was due to bubbles that were not large enough to completely fill the local pores. Over time, as bubbles grew to a certain size, their interaction with the fibrous structure leaded to deformation and wrapping around the fibers. This deformation initiated a phase of rapid growth in bubble coverage. Such behavior had also been observed in synchrotron imaging studies reported in the literature [67]. The wrapping effect facilitated coalescence with neighboring bubbles, leading to the formation of larger gas agglomerates. Once a bubble reached sufficient size, the hydrodynamic and buoyancy forces acting on it could overcome the capillary constraints imposed by the porous struc-

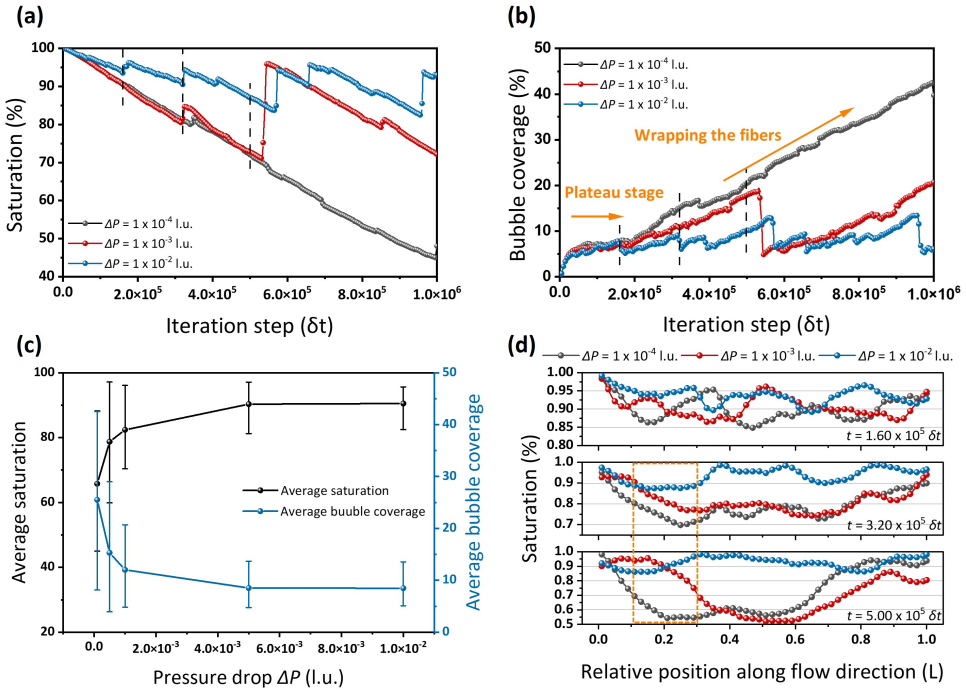

Figure 6.6.: Variation of (a) electrolyte saturation and (b) bubble coverage over time at different values of the pressure drop; (c) average saturation and bubble coverage for different pressure drops; (d) slice saturation at $t = 1.60 \times 10^5 \delta t$, $t = 3.20 \times 10^5 \delta t$ and $t = 5.00 \times 10^5 \delta t$.

ture, allowing it to detach and be carried away by the flow. This process repeated throughout the quasi-steady period, during which bubbles continuously nucleated, grow, coalesced, and detached in a dynamic equilibrium.

As the pressure drop increased, notable trends could be observed in bubble dynamics. From Figure 6.6(a), it was evident that the maximum bubble size decreased, and the bubble removal frequency increased (i.e., the period shortens) with increasing flow rate. This indicated that higher pressure drops promoted more efficient bubble detachment and transport. Meanwhile, Figure 6.6(b) showed that the fluctuation amplitude of bubble coverage gradually decreaseed with increasing flow rate, suggesting a more uniform and stable two-phase flow regime at higher flow conditions. Furthermore, based on the average saturation and bubble coverage values calculated after $t = 2.0 \times 10^5 \delta t$, a noticeable change in trend occurred at $\Delta P = 1 \times 10^{-3}$ l.u. in Figure 6.6(c). Below this threshold, the average saturation increased sharply with the pressure

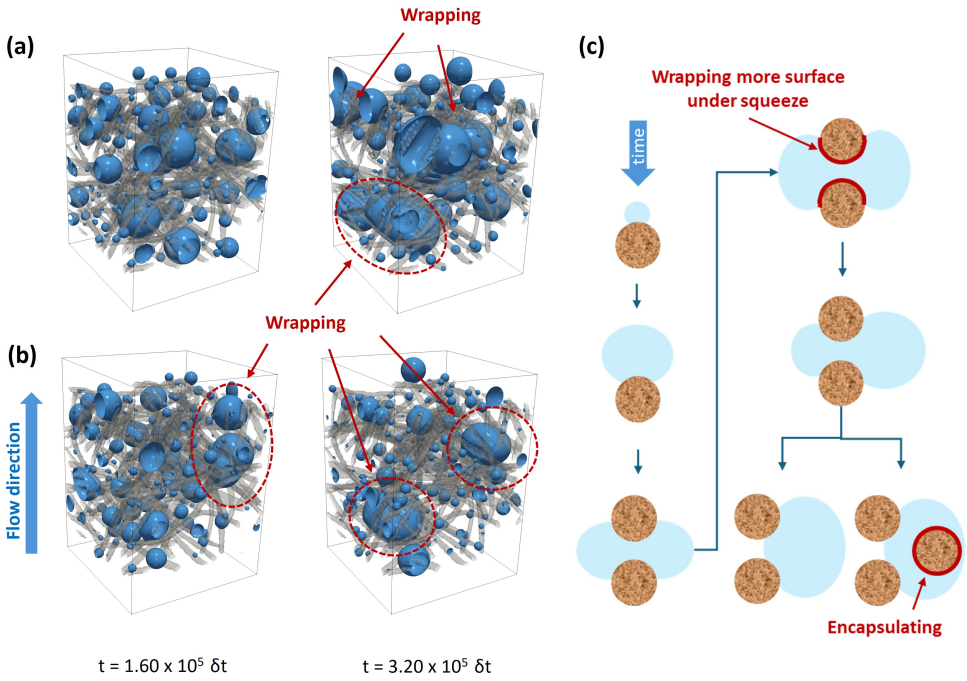

Figure 6.7.: Spatial distribution of bubbles during the plateau stage ($t = 1.60 \times 10^5 \delta t$) and rapid growth periods ($t = 3.20 \times 10^5 \delta t$) of bubble coverage indicated in Figure 6.6b). (a) Distribution at $\Delta P = 1 \times 10^{-4}$ l.u.; (b) distribution at $\Delta P = 1 \times 10^{-2}$ l.u.; (c) schematic representation of the bubble wrapping process.

drop, while bubble coverage decreased significantly. Beyond this point, both saturation and bubble coverage varied more gradually with further increases in flow rate. From an energy-saving perspective, setting pressure drop to $\Delta P = 1 \times 10^{-3}$ l.u. provided an optimal balance between bubble removal effectiveness and pumping energy input.

Figure 6.6(d) showed the variation in slice saturation along the flow direction at three time steps, as marked by grey lines in Figure 6.6(a) and Figure 6.6(b). At $t = 1.60 \times 10^5 \delta t$, all three cases exhibited relatively high bulk saturation values in Figure 6.6(a), which were 90.0%, 90.4%, and 93.7% respectively, and an overall even slice saturation distribution in Figure 6.6(b). Among them, the case with $\Delta P = 1 \times 10^{-2}$ l.u. showed the most stable and uniform distribution, with a fluctuation amplitude of approximately 5%, compared to about 10% in the other two cases. At $t = 3.20 \times 10^5 \delta t$ and $t = 5.00 \times 10^5 \delta t$, the slice saturation at $\Delta P = 1 \times 10^{-2}$ l.u. remained relatively stable. In contrast, saturation decreased by around 15% at $\Delta P = 1 \times 10^{-3}$ l.u. and by about 25% at $\Delta P = 1 \times 10^{-4}$ l.u.. In these lower-flow cases, bubbles grew large enough

to wrap around the fibers, leading to a significant increase in bubble coverage, as shown in Figure 6.6(b). The difference in the bubble coverage curve observed between $\Delta P = 1 \times 10^{-3}$ and 1×10^{-4} l.u. in Figure 6.6(b) was attributed to the presence of a pinning site in the region between 0.1 L and 0.3 L along the flow direction as shown in Figure 6.6(d). At the same reaction rate, a higher pressure drop facilitated the removal of trapped bubbles, improving saturation and reducing the number of bubbles wrapped around the fiber.

Figure 6.7 showed the spatial distribution of bubbles during the plateau satge ($t = 1.60 \times 10^5 \delta t$) and rapid growth periods ($t = 3.20 \times 10^5 \delta t$) of the bubble coverage as indicated in Figure 6.6(b). Figure 6.7(a) and 6.7(b) illustrated the distributions at $\Delta P = 1 \times 10^{-4}$ and 1×10^{-2} l.u., respectively. During the plateau period, bubble shapes were predominantly regular spherical caps in both cases, maintaining a stable contact with individual fibers. Due to the hydrophilic nature of the electrolyte, the interaction between bubbles and fibers at this stage did not result in significant wrapping, as the bubbles are limited to contacting single fibers and cannot spread further. In the rapid growth period ($t = 3.20 \times 10^5 \delta t$), as bubbles grew larger, they began to interact with multiple fibers, leading to wrapping under the constraints of the fibrous structure. At low flow rates, this wrapping was pronounced, with trapped large bubbles covering multiple fibers and significantly increasing surface coverage. However, at high flow rates, bubbles were more effectively removed, reducing the occurrence of fiber wrapping and maintaining better flow pathways within the electrode. To aid the understanding, Figure 6.7(c) provided a schematic representation of the bubble-wrapping process. Initially, at smaller sizes, bubbles maintained a spherical cap shape and interacted only with single fibers. As the bubbles grew larger, they extended to contact adjacent fibers, resulting in more wrapping due to spatial constraints within the porous structure. Under the influence of the hydrophobic surface, the bubbles gradually moved toward the large pores. However, in areas with dense fibers and under the influence of bubble coalesce growth behavior, bubbles might encapsulate some fibers.

6.5. Effect of compression ratios

The porous media in VRFB systems are typically composed of carbon, which can undergo significant structural alterations under different levels of compression or material stress. As

such, understanding the effects of compression on the pore structure of carbon and its porosity is critical for optimizing bubble transport. This section investigated the effects of different microstructures on bubble transport. To accelerate the analysis of bubble evolution in porous media, the reaction rate k_r was fixed as 1×10^{-5} l.u. and the pressure drop across the inlet and outlet was set to 1×10^{-2} l.u..

From the slope of the saturation curve in Figure 6.8(a) at the early stage of the simulation, it could be seen that higher CRs leaded to an increased gas generation rate. This trend was attributed to the enhanced spatial density of catalytic sites in the compressed carbon felt, which potentially increased spatial catalytic efficiency. However, the amplitude of the saturation curve also indicated that larger bubbles tend to be trapped under higher CRs. These larger trapped bubbles occupied more pore space, hindered the transport of reactants and reduced the effective reaction area, ultimately leading to a decrease in catalytic efficiency. The coverage curve in Figure 6.8(b) further highlighted that bubble coverage increased slightly as the CR increases from 25% to 50% but grew significantly when the CR increased from 50% to 75%. This trend could be observed intuitively in the average value curves shown in Figure 6.8(c). The sharp rise in bubble coverage was attributed to the larger bubble sizes and the denser fiber network structure under higher CRs, especially when increasing the CR from 50% to 75%. Figure 6.8(d) showed the specific surface area, which was defined as the geometric surface to volume ratio of the carbon felt, varies with compression ratio. The black curve represented an ideal, fully wetted case, while the red curve treated bubble-covered regions as unavailable. With increasing CR, the specific surface area raised markedly (densification of fibers), and the red curve showed more deviation from the black one due to more severe bubble shielding. This trend was consistent with the behavior observed in Figure 6.8(a). Lastly, Figure 6.8(e) illustrated the spatial bubble distribution for varying CRs, showing that trapped big bubbles in porous domain grew progressively larger with increasing CR, further exacerbating the obstruction of electrolyte flow.

Moreover, excessive compression could mechanically deform the carbon fibers, reduce pore connectivity, and compromise the structural integrity of the electrode over long-term cycling. Prior studies had shown that high CRs may exacerbate capacity decay by accelerating vanadium ion crossover and increasing hydraulic resistance [135–138]. On the other hand, com-

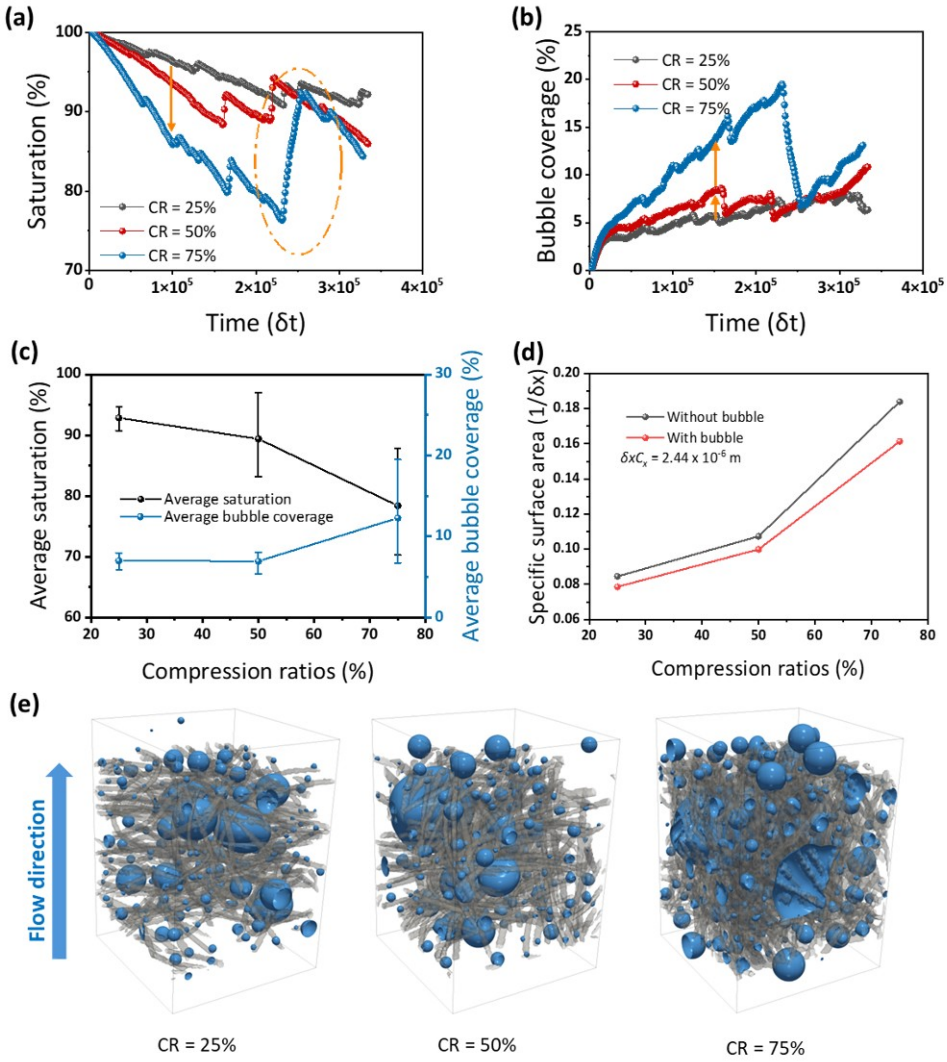

Figure 6.8.: Variation of (a) electrolyte saturation and (b) bubble coverage over time at different compression ratios; (c) average saturation and bubble coverage for different compression ratios; (d) specific surface area for different compressin ratios (with and without bubbles); (e) visualization of bubble distribution at $t = 2.0 \times 10^5 \delta t$.

pression is necessary to ensure good contact between fibers, reduce electronic resistance, and prevent electrolyte leakage. Li et al. [139] and Xiao et al. [140] demonstrated that increasing CR could reduce diffusivity but improve electronic conductivity, highlighting the trade-off between mass transport and charge conduction in porous electrodes. This trade-off between catalytic accessibility and transport limitation had also been emphasized in the design of structured carbon electrodes aiming to maximize spatial catalysis, where interstitial space utilization must be balanced against pore blockage and flow constraints [141]. Given these competing effects, including enhanced reaction site density, impeded mass transport, local bubble trapping, mechanical degradation risks, and electrical benefits, it is clear that compression must be carefully optimized. Based on the results and existing literature, a moderate CR in the range of 25% to 50% was recommended to strike a balance between catalytic accessibility, transport efficiency, and mechanical robustness in VRFB applications.

6.6. Conclusion

This study empolyed a color-gradient lattice Boltzmann model, combined with X-ray synchrotron images, to investigate bubble formation and transport in VRFBs, capturing the interplay between dynamic bubbles and electrode microstructures. The presented findings showed that bubble evolution could significantly obstruct electrolyte flow, hightlighting the needs to balance reaction rates, flow rates, and electrode microstructures to effectively manage bubble formation and transport in VRFBs.

Within the capillary-dominated pore-scale regime (Ca, $\mathrm{Bo} \ll 1$), I reported qualitative, dimensionless trends. Increasing the nominal reaction rate promotes bubble growth and detachment, while insufficient flow rates caused persistent bubble trapping. Higher compression ratio, though densified the felt (raising geometric specific surface area and electrical conductivity), while also exacerbated bubble retention.

Although this work focused on VRFBs, the mechanisms identified—bubble nucleation, growth, transport, and interactions with fibrous porous structures of electrode—were relevant to a broad class of electrochemical systems employing carbon fiber electrodes. While demonstrated here with a typical commercial carbon felt, the modeling approach would be applicable to other

porous electrode architectures, including gas diffusion layers in proton exchange membrane fuel cells and electrolyzers.

The present framework is a dynamic bubble investigation in porous electrode. It does not couple charge conservation, species transport, or dissolved-gas physics, and it uses equal-density, immiscible phases to isolate capillarity. As a result, the present framework is primarily suited for elucidating capillary-driven bubble dynamics and geometric trapping mechanisms at the pore scale, rather than for quantitatively predicting electrochemical performance. These simplifications allow the dominant hydrodynamic effects of bubble formation and retention to be isolated, while highlighting the need for future extensions that incorporate electrochemical reactions and dissolved-gas transport. Building on this, future work will introduce a minimal electrochemical coupling to relate bubble coverage to performance, and adopt a more accurate wetting boundary for a systematic study of electrode-surface properties.

7. Summary

7.1. Conclusion

HER is a well-known parasitic side reaction in VRFBs, especially under high charging potentials in the negative half-cell. While electrochemical performance losses caused by HER have been broadly acknowledged, the microscopic mechanisms—in particular, how HER-induced gas bubble formation and evolution disturb electrolyte transport and reduce electrochemically active surface area—have remained poorly understood. This is not merely a technical detail, but a fundamental gap that limits the ability to design more efficient and durable flow battery systems for long-term energy storage in renewable-based grids.

This dissertation tackles this challenge by exploring the bubble dynamics in VRFB electrodes across multiple scales, through a combination of high-resolution synchrotron X-ray tomography, deep learning-based image analysis, and pore-scale Lattice Boltzmann simulations. Synchrotron X-ray imaging, as employed in this work, is a powerful technique that allows for non-destructive, three-dimensional visualization of internal structures with high spatial resolution. With recent advances in beamline optics, detector technology, and image reconstruction, it is now possible to clearly observe bubbles inside fibrous electrodes and accurately measure their size, shape, location, and structural irregularity. This work has presented the first detailed statistical analysis of individual hydrogen bubbles inside a functioning VRFB electrode. Results show that the way bubbles form and grow strongly depends on the applied electrode potential. When the potential becomes more negative, hydrogen evolution becomes more intense, leading to the formation of fewer but larger and more irregular bubbles. These bubbles are more likely to form near the edges of the electrode and then accumulate in the center, where they block electrolyte flow and reduce the effective surface area available for electrochemical

reactions.

Based the first work, a deep learning-driven analytical framework was developed to automate the segmentation and quantification of synchrotron tomography datasets. This tool can distinguish between bubbles, electrolyte, membrane, and gasket regions, automatically separate electrodes, quantify bubble volumes, analyze individual bubble shapes, generate two-dimensional density maps, and assess membrane blockage. By replacing manual, time-consuming image analyses, this tool greatly accelerates data processing and enables systematic, high-throughput comparison of bubble distributions across different materials and operating conditions. The tool also serves as a bridge between experimental imaging and theoretical modeling by providing physically grounded morphological descriptors as input parameters for future pore-scale or continuum simulations. Its flexible, open-source design allows easy adaptation to other electrochemical systems where gas evolution plays a critical role, such as electrolyzers and fuel cells.

Nevertheless, experimental imaging, even at the synchrotron level, has inherent limitations. It remains extremely challenging to capture transient phenomena such as bubble detachment, migration, coalescence, or pinning in the complex porous architecture of carbon felt, especially under in-situ flow conditions. Temporal resolution, beam access, and image segmentation throughput impose practical constraints. To overcome these barriers, this thesis complements experimental observation with a color-gradient Lattice Boltzmann model (LBM), adapted for immiscible two-phase flow within real electrode geometries extracted from tomography. These simulations reproduce dynamic behaviors that are difficult to observe directly: bubble nucleation kinetics, detachment mechanisms, transport pathways, and their interaction with fiber geometry. By varying HER rates, flow conditions, and electrode compression, the simulations identify critical trade-offs—such as the balance between electrical conductivity and gas removal efficiency, or the optimal flow regime that minimizes energy loss while maximizing electrolyte saturation.

Crucially, the interplay between imaging and simulation enables a more holistic understanding of gas evolution phenomena in VRFBs. Imaging provides physical reality and morphological validation, while LBM simulations explore the unseen dynamics that link microstructure to macroscopic performance. Together, these approaches reveal how gas bubbles not only oc-

cupy volume but actively shape the local transport landscape, leading to persistent dry zones, increased resistance, and non-uniform reaction kinetics.

7.2. Future perspectives

The outcomes of this dissertation demonstrate that combining experimental imaging, automated analysis, and pore-scale simulations offers a powerful pathway for elucidating multiphase transport phenomena in electrochemical energy storage systems. Nevertheless, several open challenges and research directions emerge.

Future efforts should focus on coupling morphological descriptors extracted from tomography with electrochemical performance metrics. Integrating bubble characteristics—such as size distribution, shape anisotropy, and spatial clustering—into multiphysics models could help quantify their influence on local mass transfer, potential distribution, and reaction kinetics. The deep learning tool developed in this work provides a natural interface for such hybrid approaches, allowing experimental datasets to serve directly as inputs for physics-based simulations.

On the modeling side, extending the current LBM framework to include electrochemical coupling and dissolved gas dynamics will enable more realistic simulations of HER-driven processes. Incorporating variable wettability, capillary pressure effects, and reactive boundary conditions will further improve the predictive accuracy for bubble evolution under different material and operational conditions. Combining these models with experimental observations will help identify optimal design windows that minimize bubble accumulation while preserving efficient charge transfer.

From an experimental standpoint, advancing toward operando, time-resolved X-ray tomography or complementary imaging modalities will be crucial for directly capturing transient bubble behavior—such as nucleation, coalescence, detachment, and reattachment—under realistic flow and current conditions. The automation framework introduced here paves the way for “four-dimensional” (3D + time) bubble analysis once such datasets become available.

Finally, the methodologies and computational tools developed in this work have broad applicability beyond VRFBs. They can be readily adapted to study gas evolution and transport phe-

nomena in proton exchange membrane electrolyzers, zinc–air batteries, or fuel cells. By combining high-resolution imaging, machine learning, and mesoscale modeling, future research can establish unified design principles for managing multiphase transport in porous electrodes, ultimately improving the performance, lifetime, and scalability of next-generation electrochemical energy systems.

Appendix

A. Additional Synchrotron X-Ray image data for Parasitic Hydrogen Evolution Reaction

This appendix chapter provides the data published by the author in the Supplementary Information to the article **K. Duan**, K. Köble, A. Ershov, M. Schilling, A. Rampf, A. Cecilia, T. Faragó, M. Zuber, T. Baumbach, P.-C. Sui, *Investigating Bubble Formation and Evolution in Vanadium Redox Flow Batteries via Synchrotron X-Ray Imaging*, ChemSusChem, e202500282, 2024, doi: 10.1002/cssc.202500282.

Supporting Information

Displacement of the Membrane

The assembly stress of the battery stack can cause membrane deformation. Figure 4.6 displays the displacement of the membrane in a through-plane direction. The baseline is defined as the line connecting the two extreme membrane edges.

Potential-Dependent Bubble Volumes

Figure A.2(a) presents bubble volume fractions under various applied potentials, consistent with our previous publication [68]. Figure A.2(b) shows cumulative bubble volume before HER at the same potentials. These results support the conclusion that bubble accumulation is closely linked to the applied potential and HER intensity.

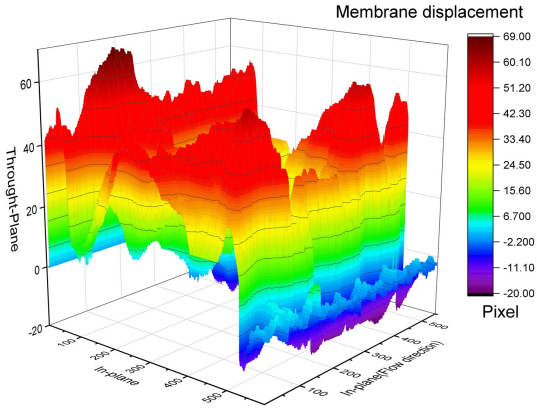

Figure A.1.: Displacement of the membrane in the through-plane direction.

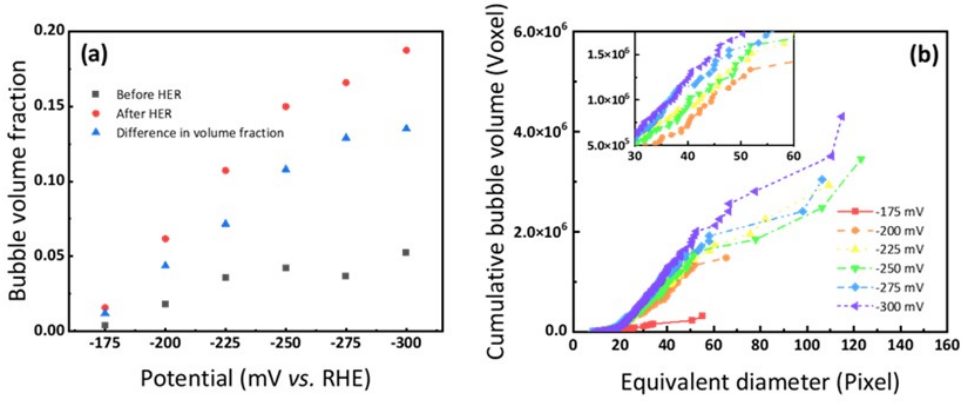

Figure A.2.: Bubble volume variations under different applied potentials: (a) bubble volume fractions; (b) cumulative bubble volumes before HER.

Bibliography

[1] United Nations Framework Convention on Climate Change (UNFCCC), The paris agreement, 2015. URL: https://unfccc.int/sites/default/files/resource/parisagreement_publication.pdf, accessed: 2025-02-27.

[2] J. G. Olivier, K. Schure, J. Peters, et al., Trends in global co2 and total greenhouse gas emissions, PBL Netherlands Environmental Assessment Agency 5 (2017) 1–11.

[3] O. Kozlov, V. Kovalchuk, S. Vistiak, N. Klymchuk, Analysis of indicators of the electrical power production enterprises' pollution and harm risk degree in terms of the paris agreement., Management Systems in Production Engineering 32 (2024).

[4] V. Klimenko, A. Klimenko, A. Tereshin, From rio to paris via kyoto: How the efforts to protect the global climate affect the world energy development. therm. eng. 66, 769–778, 2019.

[5] P. G. Wolynes, Evolution, energy landscapes and the paradoxes of protein folding, Biochimie 119 (2015) 218–230.

[6] A. Mangla, Geopolitics of renewable energy: Shaping the global power landscape, Gyan Manag. J 17 (2023) 75–80.

[7] X.-Z. Yuan, C. Song, A. Platt, N. Zhao, H. Wang, H. Li, K. Fatih, D. Jang, A review of all-vanadium redox flow battery durability: Degradation mechanisms and mitigation strategies, International Journal of Energy Research 43 (2019) 6599–6638.

[8] A. Saxena, R. Shankar, E. El-Saadany, M. Kumar, O. Al Zaabi, K. Al Hosani, U. R. Muduli, Intelligent load forecasting and renewable energy integration for enhanced grid reliability, IEEE Transactions on Industry Applications 60 (2024) 8403–8417.

[9] A. Parasuraman, T. M. Lim, C. Menictas, M. Skyllas-Kazacos, Review of material research and development for vanadium redox flow battery applications, Electrochimica Acta 101 (2013) 27–40.

[10] T. Li, X.-Z. Yuan, L. Zhang, D. Song, K. Shi, C. Bock, Degradation mechanisms and mitigation strategies of nickel-rich nmc-based lithium-ion batteries, Electrochemical Energy Reviews 3 (2020) 43–80.

[11] I. Aramendia, U. Fernandez-Gamiz, A. Martinez-San-Vicente, E. Zulueta, J. M. Lopez-Guede, Vanadium redox flow batteries: A review oriented to fluid-dynamic optimization, Energies 14 (2020) 176.

[12] K. Lourenssen, J. Williams, F. Ahmadpour, R. Clemmer, S. Tasnim, Vanadium redox flow batteries: A comprehensive review, Journal of Energy Storage 25 (2019) 100844.

[13] H. Fan, Z. Yu, S. Xia, X. Li, Review on coordinated planning of source-network-load-storage for integrated energy systems, Frontiers in Energy Research 9 (2021) 641158.

[14] U. D. of Energy (DOE), Pathways to Commercial Liftoff: Long Duration Energy Storage, Technical Report, U.S. Department of Energy, 2023. URL: https://www.energy.gov/liftoff/long-duration-energy-storage, accessed: 2025-02-27.

[15] LDES Council and McKinsey Company, Net-zero Power: Long Duration Energy Storage for a Renewable Grid, Technical Report, LDES Council and McKinsey Company, 2021. URL: https://www.mckinsey.com/~/media/mckinsey/business%20functions/sustainability/our%20insights/net%20zero%20power%20long%20duration%20energy%20storage%20for%20a%20renewable%20grid/

net-zero-power-long-duration-energy-storage-for-a-renewable-grid.pdf, accessed: 2025-02-27.

[16] T. Jirabovornwisut, A. Arpornwichanop, A review on the electrolyte imbalance in vanadium redox flow batteries, International Journal of Hydrogen Energy 44 (2019) 24485–24509.

[17] R. Ye, D. Henkensmeier, S. J. Yoon, Z. Huang, D. K. Kim, Z. Chang, S. Kim, R. Chen, Redox flow batteries for energy storage: a technology review, Journal of electrochemical energy conversion and storage 15 (2018) 010801.

[18] A. Z. Weber, M. M. Mench, J. P. Meyers, P. N. Ross, J. T. Gostick, Q. Liu, Redox flow batteries: a review, Journal of applied electrochemistry 41 (2011) 1137–1164.

[19] J. Doyle, Galvanic battery, 1879. Patent issued on September 29, 1879.

[20] Y. V. Tolmachev, Flow batteries from 1879 to 2022 and beyond, Journal of The Electrochemical Society 170 (2023) 030505.

[21] L. H. Thaller, Electrically rechargeable redox flow cells, in: 9th Intersociety energy conversion engineering conference, 1974, pp. 924–928.

[22] E. Sum, M. Rychcik, M. Skyllas-Kazacos, Investigation of the v (v)/v (iv) system for use in the positive half-cell of a redox battery, J. Power Sources;(Switzerland) 16 (1985).

[23] E. Sum, M. Skyllas-Kazacos, A study of the v (ii)/v (iii) redox couple for redox flow cell applications, Journal of Power sources 15 (1985) 179–190.

[24] M. Rychcik, M. Skyllas-Kazacos, Evaluation of electrode materials for vanadium redox cell, Journal of Power Sources 19 (1987) 45–54.

[25] M. Rychcik, M. Skyllas-Kazacos, Characteristics of a new all-vanadium redox flow battery, Journal of power sources 22 (1988) 59–67.

[26] M. Skyllas-Kazacos, M. Rychcik, R. G. Robins, All vanadium redox battery, Patent AU 0055562, 1986. Filed on April 2, 1986.

[27] M. Skyllas-Kazacos, All-vanadium redox battery and additives, ???? Patent filed on December 9, 1989.

[28] M. Skyllas-Kazacos, M. Kazacos, C. Mcdermott, Rodney John, Vanadium charging cell and vanadium dual battery system, ???? Patent filed on December 9, 1989.

[29] M. Kazacos, S. M. Kazacos, High energy density vanadium electrolyte solutions, methods of preparation thereof and all-vanadium redox cells and batteries containing high energy density electrolytes, ???? Details are based on the truncated reference information.

[30] C. Roth, J. Noack, M. Skyllas-Kazacos, Flow Batteries: From Fundamentals to Applications, John Wiley & Sons, 2022.

[31] C. P. De Leon, A. Frías-Ferrer, J. González-García, D. Szánto, F. C. Walsh, Redox flow cells for energy conversion, Journal of power sources 160 (2006) 716–732.

[32] Chinese Academy of Sciences, World's largest flow battery energy storage station connected to grid, https://english.cas.cn/newsroom/research_news/chem/202205/t20220531_306054.shtml, 2022. Accessed: March 10, 2025.

[33] A. Selänniemi, M. Hellström, M. Björklund-Sänkiaho, Long-duration energy storage technology adoption: Insights from us energy industry experts, Energy Reports 13 (2025) 378–396.

[34] M. Skyllas-Kazacos, L. Cao, M. Kazacos, N. Kausar, A. Mousa, Vanadium electrolyte studies for the vanadium redox battery—a review, ChemSusChem 9 (2016) 1521–1543.

[35] A. Hassan, T. Tzedakis, Enhancement of the electrochemical activity of a commercial graphite felt for vanadium redox flow battery (vrfb), by chemical treatment with acidic solution of k2cr2o7, Journal of Energy Storage 26 (2019) 100967.

[36] A. Aluko, A. Knight, A review on vanadium redox flow battery storage systems for large-scale power systems application, IEEE Access 11 (2023) 13773–13793.
[37] Á. Cunha, J. Martins, N. Rodrigues, F. Brito, Vanadium redox flow batteries: a technology review, International Journal of Energy Research 39 (2015) 889–918.
[38] T. Horiba, Lithium-ion battery systems, Proceedings of the IEEE 102 (2014) 939–950.
[39] M. S. Yesilyurt, H. A. Yavasoglu, An all-vanadium redox flow battery: a comprehensive equivalent circuit model, Energies 16 (2023) 2040.
[40] C. Doetsch, A. Pohlig, The use of flow batteries in storing electricity for national grids, in: Future Energy, Elsevier, 2020, pp. 263–277.
[41] L. Briot, M. Petit, Q. Cacciuttolo, M.-C. Pera, Aging phenomena and their modelling in aqueous organic redox flow batteries: A review, Journal of Power Sources 536 (2022) 231427.
[42] D. Dixon, D. J. Babu, A. Bhaskar, H.-M. Bruns, J. J. Schneider, F. Scheiba, H. Ehrenberg, Tuning the performance of vanadium redox flow batteries by modifying the structural defects of the carbon felt electrode, Beilstein Journal of Nanotechnology 10 (2019) 1698–1706.
[43] Z. Huang, A. Mu, L. Wu, B. Yang, Y. Qian, J. Wang, Comprehensive analysis of critical issues in all-vanadium redox flow battery, ACS sustainable chemistry & engineering 10 (2022) 7786–7810.
[44] K. Ngamsai, A. Arpornwichanop, Investigating the air oxidation of v (ii) ions in a vanadium redox flow battery, Journal of Power Sources 295 (2015) 292–298.
[45] T. Puleston, M. Serra, R. Costa-Castelló, Vanadium redox flow battery capacity loss mitigation strategy based on a comprehensive analysis of electrolyte imbalance effects, Applied energy 355 (2024) 122271.
[46] T. Ma, Z. Huang, X. Xie, B. Li, Evaluation of the effect of hydrogen evolution reaction on the performance of all-vanadium redox flow batteries, Electrochimica Acta 504 (2024) 144895.
[47] J. Lee, J. T. Muya, H. Chung, J. Chang, Unraveling v (v)-v (iv)-v (iii)-v (ii) redox electrochemistry in highly concentrated mixed acidic media for a vanadium redox flow battery: origin of the parasitic hydrogen evolution reaction, ACS applied materials & interfaces 11 (2019) 42066–42077.
[48] L. Eifert, Z. Jusys, R. J. Behm, R. Zeis, Side reactions and stability of pre-treated carbon felt electrodes for vanadium redox flow batteries: A dems study, Carbon 158 (2020) 580–587.
[49] T. Al Najjar, M. M. Omran, N. K. Allam, E. N. El Sawy, Tungsten oxide nanostructures for all-vanadium redox flow battery: Enhancing the V(II)/V(III) reaction and inhibiting H_2 evolution, Journal of Energy Storage 79 (2024) 110123.
[50] Y. Wen, T. P. Neville, A. J. Sobrido, P. R. Shearing, D. Brett, Bismuth concentration influenced competition between electrochemical reactions in the all-vanadium redox flow battery, Journal of Materials Chemistry A 11 (2023) 13341–13352.
[51] J. Schneider, E. Bulczak, G. A. El-Nagar, M. Gebhard, P. Kubella, M. Schnucklake, A. Fetyan, I. Derr, C. Roth, Degradation phenomena of bismuth-modified felt electrodes in VRFB studied by electrochemical impedance spectroscopy, Batteries 5 (2019) 16.
[52] C. Choi, S. Kim, R. Kim, Y. Choi, S. Kim, H.-y. Jung, J. H. Yang, H.-T. Kim, A review of vanadium electrolytes for vanadium redox flow batteries, Renewable and Sustainable Energy Reviews 69 (2017) 263–274.
[53] W. Tian, H. Du, J. Wang, J. J. Weigand, J. Qi, S. Wang, L. Li, A review of electrolyte additives in vanadium redox flow batteries, Materials 16 (2023) 4582.

[54] M. Skyllas-Kazacos, L. Cao, M. Kazacos, N. Kausar, A. Mousa, Vanadium electrolyte studies for the vanadium redox battery—a review, ChemSusChem 9 (2016) 1521–1543.
[55] X. Wu, J. Liu, X. Xiang, J. Zhang, J. Hu, Y. Wu, Electrolytes for vanadium redox flow batteries, Pure and Applied Chemistry 86 (2014) 661–669.
[56] A. Fetyan, G. A. El-Nagar, I. Lauermann, M. Schnucklake, J. Schneider, C. Roth, Detrimental role of hydrogen evolution and its temperature-dependent impact on the performance of vanadium redox flow batteries, Journal of Energy Chemistry 32 (2019) 57–62.
[57] C. Zhang, T. Zhao, Q. Xu, L. An, G. Zhao, Effects of operating temperature on the performance of vanadium redox flow batteries, Applied Energy 155 (2015) 349–353.
[58] L. Wei, L. Xiaokun, W. Bin, X. Shuang, H. Yonghong, In-situ investigation of hydrogen evolution reaction in vanadium redox flow batteries, Applied Energy 190 (2017) 1112–1118.
[59] L. Li, X. Chen, Z. Feng, Y. Jiang, L. Dai, J. Zhu, Y. Liu, L. Wang, Z. He, Recent advances and perspectives of practical modifications of vanadium redox flow battery electrodes, Green Chemistry 26 (2024) 6339–6360.
[60] Z. He, Y. Lv, T. Zhang, Y. Zhu, L. Dai, S. Yao, W. Zhu, L. Wang, Electrode materials for vanadium redox flow batteries: Intrinsic treatment and introducing catalyst, Chemical Engineering Journal 427 (2022) 131680.
[61] M. Kim, M. Ko, Suppressing effect of hydrogen evolution by oxygen functional groups on cnt/graphite felt electrode for vanadium redox flow battery, Journal of the Korean institute of surface engineering 54 (2021) 164–170.
[62] D. N. Buckley, D. Oboroceanu, N. Quill, C. Lenihan, D. N. Eidhin, R. P. Lynch, Electrolyte stability in vanadium flow batteries, MRS Advances 3 (2018) 3201–3212.
[63] Y.-J. Zhang, Q. Ye, M. Ni, The impact of in-situ hydrogen evolution on the flow resistance of electrolyte flowing through the carbon felt electrode in a redox flow battery, Journal of Power Sources 564 (2023) 232837.
[64] Q. Ye, J. Dai, P. Cheng, T. Zhao, Gas evolution induced vicious cycle between bubble trapping and flow choking in redox flow battery stacks, International Journal of Heat and Mass Transfer 221 (2024) 125100.
[65] L. Eifert, N. Bevilacqua, K. Köble, K. Fahy, L. Xiao, M. Li, K. Duan, A. Bazylak, P.-C. Sui, R. Zeis, Synchrotron x-ray radiography and tomography of vanadium redox flow batteries—cell design, electrolyte flow geometry, and gas bubble formation, ChemSusChem 13 (2020) 3154–3165.
[66] K. Köble, M. Jaugstetter, M. Schilling, M. Braig, T. Diemant, K. Tschulik, R. Zeis, Multimodal characterization of carbon electrodes' thermal activation for vanadium redox flow batteries, Journal of Power Sources 569 (2023) 233010.
[67] N. Bevilacqua, L. Eifert, R. Banerjee, K. Köble, T. Faragó, M. Zuber, A. Bazylak, R. Zeis, Visualization of electrolyte flow in vanadium redox flow batteries using synchrotron x-ray radiography and tomography–impact of electrolyte species and electrode compression, Journal of Power Sources 439 (2019) 227071.
[68] K. Köble, A. Ershov, K. Duan, M. Schilling, A. Rampf, A. Cecilia, T. Faragó, M. Zuber, T. Baumbach, R. Zeis, Insights into the hydrogen evolution reaction in vanadium redox flow batteries: A synchrotron radiation based x-ray imaging study, Journal of Energy Chemistry 91 (2024) 132–144.
[69] A. A. Shah, H. Al-Fetlawi, F. Walsh, Dynamic modelling of hydrogen evolution effects in the all-vanadium redox flow battery, Electrochimica Acta 55 (2010) 1125–1139.
[70] M. M. Saleh, M. H. El-Ankily, M. S. El-Deab, B. El-Anadouli, Electrocatalytic activity of metal-loaded reticulated vitreous carbon electrodes for hydrogen evolution from flowing alkaline solutions, Bulletin of the Chemical Society of Japan 79 (2006) 1711–1718.

[71] X. Qian, H.-Y. Jung, S. Jung, A comprehensive study of parasitic gas evolution reactions in a vanadium redox flow battery, Journal of Cleaner Production 428 (2023) 139468.

[72] L. Chen, Y. He, W.-Q. Tao, P. Zelenay, R. Mukundan, Q. Kang, Pore-scale study of multiphase reactive transport in fibrous electrodes of vanadium redox flow batteries, Electrochimica Acta 248 (2017) 425–439.

[73] Z. Liu, H. Pang, M. Pan, C. Wan, Calibration and compensation of geomagnetic vector measurement system and improvement of magnetic anomaly detection, IEEE Geoscience and Remote Sensing Letters 13 (2016) 447–451.

[74] X. Shan, H. Chen, Lattice Boltzmann model for simulating flows with multiple phases and components, Physical Review E 47 (1993) 1815.

[75] D. Zhang, Q. Cai, O. O. Taiwo, V. Yufit, N. P. Brandon, S. Gu, The effect of wetting area in carbon paper electrode on the performance of vanadium redox flow batteries: A three-dimensional lattice boltzmann study, Electrochimica Acta 283 (2018) 1806–1819.

[76] D. Zhang, A. Forner-Cuenca, O. O. Taiwo, V. Yufit, F. R. Brushett, N. P. Brandon, S. Gu, Q. Cai, Understanding the role of the porous electrode microstructure in redox flow battery performance using an experimentally validated 3d pore-scale lattice boltzmann model, Journal of Power Sources 447 (2020) 227249.

[77] K. Duan, K. Köble, A. Ershov, M. Schilling, A. Rampf, A. Cecilia, T. Faragó, M. Zuber, T. Baumbach, P. chieh Sui, R. Zeis, Investigating bubble formation and evolution in vanadium redox flow batteries via synchrotron X-ray imaging, ChemSusChem 00 (2025).

[78] L. Eifert, R. Banerjee, Z. Jusys, R. Zeis, Characterization of carbon felt electrodes for vanadium redox flow batteries: impact of treatment methods, Journal of The Electrochemical Society 165 (2018) A2577.

[79] S. Zhong, C. Padeste, M. Kazacos, M. Skyllas-Kazacos, Comparison of the physical, chemical and electrochemical properties of rayon-and polyacrylonitrile-based graphite felt electrodes, Journal of Power sources 45 (1993) 29.

[80] B. Sun, M. Skyllas-Kazacos, Modification of graphite electrode materials for vanadium redox flow battery application—i. thermal treatment, Electrochimica acta 37 (1992) 1253.

[81] K. Köble, L. Eifert, N. Bevilacqua, K. F. Fahy, A. Bazylak, R. Zeis, Synchrotron x-ray radiography of vanadium redox flow batteries–time and spatial resolved electrolyte flow in porous carbon electrodes, Journal of Power Sources 492 (2021) 229660.

[82] T. Faragó, S. Gasilov, I. Emslie, M. Zuber, L. Helfen, M. Vogelgesang, T. Baumbach, Tofu: a fast, versatile and user-friendly image processing toolkit for computed tomography, Synchrotron Radiation 29 (2022) 916.

[83] D. Paganin, S. C. Mayo, T. E. Gureyev, P. R. Miller, S. W. Wilkins, Simultaneous phase and amplitude extraction from a single defocused image of a homogeneous object, Journal of microscopy 206 (2002) 33.

[84] K. He, X. Zhang, S. Ren, J. Sun, Deep residual learning for image recognition, in: Proceedings of the IEEE conference on computer vision and pattern recognition, 2016, p. 770.

[85] H. Taniguchi, N. Kohira, T. Ohnishi, H. Kawahira, M. von und zu Fraunberg, J. E. Jääskeläinen, M. Hauta-Kasari, Y. Iwadate, H. Haneishi, Improving convenience and reliability of 5-ALA-induced fluorescent imaging for brain tumor surgery, in: Medical Image Computing and Computer-Assisted Intervention–MICCAI 2015: 18th International Conference, Munich, Germany, October 5-9, 2015, Proceedings, Part III 18, Springer, 2015, p. 209.

[86] S. Rit, M. V. Oliva, S. Brousmiche, R. Labarbe, D. Sarrut, G. C. Sharp, The reconstruction toolkit (rtk), an open-source cone-beam ct reconstruction toolkit based on the insight toolkit (itk), in: Journal of Physics: Conference Series, volume 489, IOP Publishing,

2014, p. 012079.
[87] S. Zhong, X. Zou, Z. Zhang, H. Tian, A flexible image analysis method for measuring bubble parameters, Chemical Engineering Science 141 (2016) 143.
[88] T.-C. Chang, J.-P. Zhang, Y.-K. Fuh, Electrical, mechanical and morphological properties of compressed carbon felt electrodes in vanadium redox flow battery, Journal of Power Sources 245 (2014) 66.
[89] R. Banerjee, N. Ge, C. Han, J. Lee, M. George, H. Liu, D. Muirhead, P. Shrestha, A. Bazylak, Identifying in operando changes in membrane hydration in polymer electrolyte membrane fuel cells using synchrotron x-ray radiography, International Journal of Hydrogen Energy 43 (2018) 9757.
[90] R. Banerjee, N. Bevilacqua, A. Mohseninia, B. Wiedemann, F. Wilhelm, J. Scholta, R. Zeis, Carbon felt electrodes for redox flow battery: impact of compression on transport properties, Journal of Energy Storage 26 (2019) 100997.
[91] P.-H. Chi, S. Chan, F. Weng, A. Su, P. Sui, N. Djilali, On the effects of non-uniform property distribution due to compression in the gas diffusion layer of a pemfc, International Journal of Hydrogen Energy 35 (2010) 2936.
[92] L. Chen, A. He, J. Zhao, Q. Kang, Z.-Y. Li, J. Carmeliet, N. Shikazono, W.-Q. Tao, Pore-scale modeling of complex transport phenomena in porous media, Progress in Energy and Combustion Science 88 (2022) 100968.
[93] D. A. Wolf-Gladrow, Lattice-gas cellular automata and lattice Boltzmann models: an introduction, Springer, 2004.
[94] S. Goldstein, Boltzmann's approach to statistical mechanics, in: Chance in physics: Foundations and perspectives, Springer, 2001, p. 39.
[95] T. Krüger, H. Kusumaatmaja, A. Kuzmin, O. Shardt, G. Silva, E. M. Viggen, The lattice boltzmann method, Springer International Publishing 10 (2017) 4–15.
[96] S. Harris, An introduction to the theory of the Boltzmann equation, Courier Corporation, 2004.
[97] G. A. Bird, Molecular gas dynamics, NASA STI/Recon Technical Report A 76 (1976) 40225.
[98] T. I. Gombosi, Gaskinetic theory, 9, Cambridge University Press, 1994.
[99] P. A. Thompson, G. S. Beavers, Compressible-fluid dynamics, Journal of Applied Mechanics 39 (1972) 366.
[100] P. L. Bhatnagar, E. P. Gross, M. Krook, A model for collision processes in gases. i. small amplitude processes in charged and neutral one-component systems, Physical review 94 (1954) 511.
[101] A. K. Gunstensen, D. H. Rothman, S. Zaleski, G. Zanetti, Lattice boltzmann model of immiscible fluids, Physical review A 43 (1991) 4320.
[102] D. Grunau, S. Chen, K. Eggert, A lattice boltzmann model for multiphase fluid flows, Physics of Fluids A: Fluid Dynamics 5 (1993) 2557–2562.
[103] X. Shan, H. Chen, Lattice boltzmann model for simulating flows with multiple phases and components, Physical review E 47 (1993) 1815.
[104] S. Leclaire, A. Parmigiani, O. Malaspinas, B. Chopard, J. Latt, Generalized three-dimensional lattice boltzmann color-gradient method for immiscible two-phase pore-scale imbibition and drainage in porous media, Physical Review E 95 (2017) 033306.
[105] T. Scheel, Q. Xie, M. Sega, J. Harting, Viscous to inertial coalescence of liquid lenses: A lattice Boltzmann investigation, Physical Review Fluids 8 (2023) 074201.
[106] Z. Guo, C. Zheng, B. Shi, Discrete lattice effects on the forcing term in the lattice Boltzmann method, Physical Review E 65 (2002) 046308.

[107] T. Scheel, P. Malgaretti, J. Harting, Enhancement of bubble transport in porous electrodes and catalysts, The Journal of Chemical Physics 160 (2024) 194706.

[108] R. Schweiss, A. Pritzl, C. Meiser, Parasitic hydrogen evolution at different carbon fiber electrodes in vanadium redox flow batteries, Journal of The Electrochemical Society 163 (2016) A2089.

[109] A. Narváez, K. Yazdchi, S. Luding, J. Harting, From creeping to inertial flow in porous media: a lattice Boltzmann–finite element study, Journal of statistical mechanics: theory and experiment 2013 (2013) P02038.

[110] L. Ye, S. Qi, T. Cheng, Y. Jiang, Z. Feng, M. Wang, Y. Liu, L. Dai, L. Wang, Z. He, Vanadium redox flow battery: review and perspective of 3D electrodes, ACS Nano 18 (2024) 18852–18869. doi:doi: 10.1021/acsnano.4c06675.

[111] M. Schilling, L. Eifert, K. Köble, M. Jaugstetter, N. Bevilacqua, K. F. Fahy, K. Tschulik, A. Bazylak, R. Zeis, Investigating the influence of treatments on carbon felts for vanadium redox flow batteries, ChemSusChem 17 (2024) e202301063. doi:doi: 10.1002/cssc.202301063.

[112] M. Latva-Kokko, D. H. Rothman, Static contact angle in lattice Boltzmann models of immiscible fluids, Physical Review E—Statistical, Nonlinear, and Soft Matter Physics 72 (2005) 046701.

[113] Y. Chen, A. J. Valocchi, Q. Kang, H. S. Viswanathan, Inertial effects during the process of supercritical CO_2 displacing brine in a sandstone: Lattice Boltzmann simulations based on the continuum-surface-force and geometrical wetting models, Water Resour. Res. 55 (2019) 11144–11165. doi:doi: 10.1029/2019WR025746.

[114] G. Nath, O. Aouane, J. Harting, Reaction-limited evaporation for the color-gradient lattice Boltzmann model, J. Chem. Phys. 162 (2025).

[115] M. Sedahmed, R. C. Coelho, Wetting and pressure gradient performance in a lattice Boltzmann color gradient model, Phys. Fluids 36 (2024) 092117.

[116] F. Zahid, J. A. Cunningham, Review of the color gradient lattice Boltzmann method for simulating multi-phase flow in porous media: Viscosity, gradient calculation, and fluid acceleration, Fluids 10 (2025) 128.

[117] Y. Qin, P. Qi, J. Zhao, X. Li, N. Wang, Q. Li, J. Ge, J. Liu, J. Yang, C. Yan, Measurement and accurate prediction of surface tension for $VOSO_4$-H_2SO_4-H_2O ternary electrolyte system at high-concentration in vanadium redox flow batteries, J. Mol. Liq. 365 (2022) 120079. doi:doi: 10.1016/j.molliq.2022.120079.

[118] M. A. Hoeh, T. Arlt, I. Manke, J. Banhart, D. L. Fritz, W. Maier, W. Lehnert, In operando synchrotron x-ray radiography studies of polymer electrolyte membrane water electrolyzers, Electrochemistry communications 55 (2015) 55–59.

[119] U. Panchenko, T. Arlt, I. Manke, M. Müller, D. Stolten, W. Lehnert, Synchrotron radiography for a proton exchange membrane (pem) electrolyzer, Fuel Cells 20 (2020) 300–306.

[120] D. Jo, S. T. Revankar, Bubble mechanisms and characteristics at pore scale in a packed-bed reactor, Chemical engineering science 64 (2009) 3179–3187.

[121] H. A.-Z. A.-Y. Al-Fetlawi, Modelling and simulation of all-vanadium redox flow batteries, Ph.D. thesis, University of Southampton, 2011.

[122] A. Raman, S. Schlautmann, H. Gardeniers, D. Fernández Rivas, Electrolytic bubble coalescence on hydrophobic cavity arrays determines departure radius and lowers electrolyte supersaturation, Small 21 (2025) e05728.

[123] M. Li, N. Bevilacqua, L. Zhu, W. Leng, K. Duan, L. Xiao, R. Zeis, P.-C. Sui, Mesoscopic modeling and characterization of the porous electrodes for vanadium redox flow batteries, Journal of Energy Storage 32 (2020) 101782.

[124] J. Piwek, A. Platek, E. Frackowiak, K. Fic, Mechanisms of the performance fading of carbon-based electrochemical capacitors operating in a lino3 electrolyte, Journal of power sources 438 (2019) 227029.

[125] A. Colliard-Granero, K. Duan, R. Zeis, M. Eikerling, K. Malek, M. J. Eslamibidgoli, Advancing vanadium redox flow battery analysis: A deep learning approach for high-throughput 3d visualization and bubble quantification, Digital Discovery (2025).

[126] S. Xie, R. Girshick, P. Dollár, Z. Tu, K. He, Aggregated residual transformations for deep neural networks, in: Proceedings of the IEEE conference on computer vision and pattern recognition, 2017, pp. 1492–1500.

[127] O. Oktay, J. Schlemper, L. L. Folgoc, M. Lee, M. Heinrich, K. Misawa, K. Mori, S. McDonagh, N. Y. Hammerla, B. Kainz, et al., Attention u-net: Learning where to look for the pancreas, arXiv preprint arXiv:1804.03999 (2018).

[128] H. Huang, L. Lin, R. Tong, H. Hu, Q. Zhang, Y. Iwamoto, X. Han, Y.-W. Chen, J. Wu, Unet 3+: A full-scale connected unet for medical image segmentation, in: ICASSP 2020-2020 IEEE international conference on acoustics, speech and signal processing (ICASSP), Ieee, 2020, pp. 1055–1059.

[129] H. Cao, Y. Wang, J. Chen, D. Jiang, X. Zhang, Q. Tian, M. Wang, Swin-unet: Unet-like pure transformer for medical image segmentation, in: European conference on computer vision, Springer, 2022, pp. 205–218.

[130] G. Bradski, The opencv library., Dr. Dobb's Journal: Software Tools for the Professional Programmer 25 (2000) 120–123.

[131] W. J. Schroeder, L. S. Avila, W. Hoffman, Visualizing with vtk: a tutorial, IEEE Computer graphics and applications 20 (2000) 20–27.

[132] D. P. Kingma, J. Ba, Adam: A method for stochastic optimization, arXiv preprint arXiv:1412.6980 (2014).

[133] T.-Y. Lin, P. Goyal, R. Girshick, K. He, P. Dollár, Focal loss for dense object detection, in: Proceedings of the IEEE international conference on computer vision, 2017, pp. 2980–2988.

[134] K. Köble, M. Schilling, L. Eifert, N. Bevilacqua, K. F. Fahy, P. Atanassov, A. Bazylak, R. Zeis, Revealing the multifaceted impacts of electrode modifications for vanadium redox flow battery electrodes, ACS Applied Materials & Interfaces 15 (2023) 46775–46789.

[135] K. I. Jeong, S. H. Lim, H. Hong, J.-M. Jeong, W. V. Kim, S. S. Kim, Enhancing vanadium redox flow batteries performance through local compression ratio adjustment using stiffness gradient carbon felt electrodes, Applied Materials Today 35 (2023) 101928.

[136] C.-L. Hsieh, P.-H. Tsai, N.-Y. Hsu, Y.-S. Chen, Effect of compression ratio of graphite felts on the performance of an all-vanadium redox flow battery, Energies 12 (2019) 313.

[137] K. Bromberger, J. Kaunert, T. Smolinka, A model for all-vanadium redox flow batteries: introducing electrode-compression effects on voltage losses and hydraulics, Energy Technology 2 (2014) 64–76.

[138] Q. Wang, R. Yan, J. Chen, Z. Jiang, Z. Qu, Numerical study of vanadium redox flow battery with gradient porosity induced by electrode compression, Journal of Energy Storage 72 (2023) 108465.

[139] M. Li, N. Bevilacqua, L. Zhu, W. Leng, K. Duan, L. Xiao, R. Zeis, P.-C. Sui, Mesoscopic modeling and characterization of the porous electrodes for vanadium redox flow batteries, Journal of Energy Storage 32 (2020) 101782.

[140] L. Xiao, M. Luo, L. Zhu, K. Duan, N. Bevilacqua, L. Eifert, R. Zeis, P.-C. Sui, Pore-scale characterization and simulation of porous electrode material for vanadium redox flow battery: effects of compression on transport properties, Journal of The Electrochemical

Society 167 (2020) 110545.

[141] H. Sheng, Q. Ma, J.-G. Yu, X.-D. Zhang, W. Zhang, Y.-X. Yin, X. Wu, X.-X. Zeng, Y.-G. Guo, Robust electrodes with maximized spatial catalysis for vanadium redox flow batteries, ACS Applied Materials & Interfaces 10 (2018) 38922–38927.

List of publications

Journal articles

- K. Köble, A. Ershov, **K. Duan**, M. Schilling, A. Rampf, A. Cecilia, T. Faragó, M. Zuber, T. Baumbach, R. Zeis, *Insights into the hydrogen evolution reaction in vanadium redox flow batteries: A synchrotron radiation based X-ray imaging study*, J. Energy Chem., 2024, 91, 132, doi: 10.1016/j.jechem.2023.12.010.
- M. Schilling, A. Ershov, R. Debastiani, **K. Duan**, K. Köble, S. Scherer, L. Lan, A. Rampf, T. Faragó, M. Zuber, A. Cecilia, S. Liu, C. Liu, T. Baumbach, J. Li, P.-C. Sui, R. Zeis, *Bamboo charcoal as electrode material for vanadium redox flow batteries*, Energy Adv., 2024, 3(5), 997, doi: 10.1039/D4YA00166D.
- **K. Duan**, K. Köble, A. Ershov, M. Schilling, A. Rampf, A. Cecilia, T. Faragó, M. Zuber, T. Baumbach, P.-C. Sui, R. Zeis, *Investigating Bubble Formation and Evolution in Vanadium Redox Flow Batteries via Synchrotron X-Ray Imaging*, ChemSusChem, 2024, e202500282, doi: 10.1002/cssc.202500282.
- André Colliard-Granero†, **Kangjun Duan†**, Roswitha Zeis, Michael Eikerling, Kourosh Malek, Mohammad J. Eslamibidgoli *Advancing Vanadium Redox Flow Battery Analysis: A Deep Learning Approach for High-Throughput 3D Visualization and Bubble Quantification*, Digit. Discov., 2025, 4(10): 2724-2736, doi: 10.1039/D5DD00158G[1]
- **K. Duan**, T. H. Vu, A. Ershov, T. Kadyk, Q. Xie, J. Harting, M. Eikerling, *Parasitic Gas Evolution Reactions in Vanadium Redox Flow Batteries: A Lattice Boltzmann Study*, Energy Conv. Manag, 2026, 348: 120754. doi: doi.org/10.1016/j.enconman.2025.120754.

Conference talks

- **K. Duan**, T.H. Vu, T. Kadyk, Q. Xie, J. Harting, M. Eikerling, *Pore-scale investigation of transport phenomena in compressed electrodes of vanadium redox flow batteries*, 10^{th} Asian Symposium on Computational Heat Transfer and Fluid Flow-2025 (ASCHT2025), October 2025 (Wuhan).
- **K. Duan**, T.H. Vu, T. Kadyk, Q. Xie, J. Harting, M. Eikerling, *Parasitic Gas Evolution Reactions in Vanadium Redox Flow Batteries: A Lattice Boltzmann Study*, 33^{rd} Discrete

[1] Superscript † means equal contribution.

Simulation of Fluid Dynamics (DSFD) Conference, July 2025 (Zürich).

Conference posters

- **K. Duan**, L. Zhu, M. Li, L. Xiao, N. Bevilacqua, L. Eifert, I. Manke, H. Markötter, R. Zhang, R. Zeis, P.-C. Sui, *Multiphase and Pore Scale Modeling on Catalyst Layer of High-Temperature Polymer Electrolyte Membrane Fuel Cell*, Modval18, March 14–16, 2022 (München).
- **K. Duan**, K. Köble, A. Ershov, M. Schilling, A. Rampf, A. Cecilia, T. Faragó, M. Zuber, T. Baumbach, P.-C. Sui, R. Zeis, *Bubbles in Vanadium Redox Flow Batteries - A Synchrotron X-Ray Study*, HIU Biennel Meeting, July 11–12, 2023 (Ulm).
- **K. Duan**, Y. Yang, P.-C. Sui, R. Zeis, *Investigating the Influence of Electrode Compression on Vanadium Redox Flow Battery Performance: Multiphase Pore-Scale Simulation of Carbon Felt Electrodes*, 244th ECS Meeting, October 8–12, 2023 (Gothenburg).
- **K. Duan**, T. Kadyk, Q. Xie, J. Harting, M. Eikerling, *Parasitic Gas Evolution Reactions in Vanadium Redox Flow Batteries Studied with the Lattice Boltzmann Method*, Helmholtz energy workshop, October 7–8, 2024 (Frankfurt).

Band / Volume 712
Data-Driven Modeling for Digital Representations in Energy Systems
M. C. Zimmer (2026), xv, 166 pp
ISBN: 978-3-95806-926-8 (Print)
ISBN: 978-3-95806-927-5 (E-Book)

Band / Volume 713
Towards integrated PV applications: development of lightweight silicon heterojunction solar modules and their damp-heat and UV stability
K. Zhang (2026), iii, 179 pp
ISBN: 978-3-95806-928-2 (Print)
ISBN: 978-3-95806-929-9 (E-Book)

Band / Volume 714
Zinc-Based Catalysts for the Electrochemical CO_2 Reduction
I. Stamatelos (2026), vii, 136 pp
ISBN: 978-3-95806-932-9 (Print)
ISBN: 978-3-95806-933-6 (E-Book)

Band / Volume 715
Charakterisierung innovativer keramischer Materialien für Elektrolysezellen
L. P. Wehner (2026), xiv, 110 pp
ISBN: 978-3-95806-936-7 (Print)
ISBN: 978-3-95806-937-4 (E-Book)

Band / Volume 716
Process Optimization and Scale-Up for $Ba(Zr,Ce,Y)O_{3-\delta}$-Based Proton-Conducting Electrolysis Half-Cells
L.-A. Schäfer (2026), iv, 141 pp
ISBN: 978-3-95806-940-4 (Print)
ISBN: 978-3-95806-941-1 (E-Book)

Band / Volume 717
Kostenoptimale Energieausfälle in erneuerbaren Energiesystemen
D. Franzmann (2026), xix, 235 pp
ISBN: 978-3-95806-942-8 (Print)
ISBN: 978-3-95806-943-5 (E-Book)

Band / Volume 718
***Semiclassical Thermodynamics* of Metal-Solution Interfaces: A Density-Potential Functional Theory Study**
Z. Zhang (2026), 143 pp
ISBN: 978-3-95806-946-6 (Print)
ISBN: 978-3-95806-947-3 (E-Book)

Band / Volume 719
Development and Characterization of the Airborne Chemical Ionization Mass Spectrometer FunMass-C for Atmospheric Trace Gas Measurements
S. Alber (2026), xli, 265 pp
ISBN: 978-3-95806-948-0 (Print)
ISBN: 978-3-95806-949-7 (E-Book)

Band / Volume 720
Material design and stability of All-Solid-State Lithium batteries
F. H. Al-Jaljouli (2026), xv, 174 pp
ISBN: 978-3-95806-950-3 (Print)
ISBN: 978-3-95806-951-0 (E-Book)

Band / Volume 721
Towards improved representation of the hydrological cycle by assimilating multi-source remotely sensed soil moisture data in terrestrial system models
H. Zhao (2026), XVI, 139 pp
ISBN: 978-3-95806-952-7 (Print)
ISBN: 978-3-95806-953-4 (E-Book)

Band / Volume 722
Combining Lattice Boltzmann Simulation and Synchrotron Imaging to Study Bubble Dynamics in Electrodes of Vanadium Redox Flow Batteries
K. Duan (2026), xxiii, 116 pp
ISBN: 978-3-95806-954-1 (Print)
ISBN: 978-3-95806-955-8 (E-Book)

Weitere ***Schriften des Verlags im Forschungszentrum Jülich*** unter
http://wwwzb1.fz-juelich.de/verlagextern1/index.asp

Energie & Umwelt / Energy & Environment
Band / Volume 722
ISBN 978-3-95806-955-8

Mitglied der Helmholtz-Gemeinschaft

JÜLICH
Forschungszentrum